https://theses.gla.ac.uk/

Theses Digitisation:

https://www.gla.ac.uk/myglasgow/research/enlighten/theses/digitisation/

This is a digitised version of the original print thesis.

Copyright and moral rights for this work are retained by the author

A copy can be downloaded for personal non-commercial research or study, without prior permission or charge

This work cannot be reproduced or quoted extensively from without first obtaining permission in writing from the author

The content must not be changed in any way or sold commercially in any format or medium without the formal permission of the author

When referring to this work, full bibliographic details including the author, title, awarding institution and date of the thesis must be given

Enlighten: Theses
https://theses.gla.ac.uk/
research-enlighten@glasgow.ac.uk

Computer Modelling of Transport in Electron Waveguides with Application to Realistic Quantum Point Contacts

by

Michael John Laughton

March 1992

A Thesis submitted to the Faculty of Engineering of the University of Glasgow for the degree of Doctor of Philosophy

© Michael John Laughton, 1992.

ProQuest Number: 11011475

All rights reserved

INFORMATION TO ALL USERS
The quality of this reproduction is dependent upon the quality of the copy submitted.

In the unlikely event that the author did not send a complete manuscript
and there are missing pages, these will be noted. Also, if material had to be removed,
a note will indicate the deletion.

ProQuest 11011475

Published by ProQuest LLC (2018). Copyright of the Dissertation is held by the Author.

All rights reserved.
This work is protected against unauthorized copying under Title 17, United States Code
Microform Edition © ProQuest LLC.

ProQuest LLC.
789 East Eisenhower Parkway
P.O. Box 1346
Ann Arbor, MI 48106 – 1346

Acknowledgements

As many will testify, the life of a research student is far from easy. It is, therefore, a great pleasure to acknowledge the efforts of the many people who have helped, cajoled and bullied me in my research studies during my time in the Electrical and Electronic Engineering Department at Glasgow University and more latterly continued their support after I left the department.

I would like to thank my supervisor, Prof John Barker. His enthusiasm and vision have proved fundamental to this project. Mike Finch and Jeremy Pepin gave me assistance in my early research as they came to the end of their own studies. In particular I would particularly like to thank Mike for passing on some of the less obvious black art associated with the various computer systems.

John Davies has provided a basis for this work through an excellent postgraduate lecture course and through many discussions which have contributed enormously to my understanding. This work has also benefitted greatly from collaboration with the research of John Davies and John Nixon and I am very grateful.for their continued friendship. John Arnold and Pete Ansbro have provided valuable insight in relating this work to their own research interests in electromagnetic waveguides.

Thanks are due to Ray Hutchins for his interest in my welfare and his continual encouragement. I would also like to remember the late Prof Lamb. As head of the department during my time at Glasgow, Prof Lamb showed an interest in my progress and generously made available additional finance to supplement my Science and Engineering Research Council grant.

Most of all I can now, at long last, acknowledge the enormous contribution that my wife, Fran, has made towards this work. If it had not been for Fran's encouragement, support and, at times, ruthless bullying this work would never have been completed. This thesis also owes much to her skills of sentence construction, artistry and general scientific acumen. Thanks also to our parents Charles and Barbara Laughton and Stewart and Janet Darlow. Their patience, care and understanding have proved an important foundation for our work.

Table of Contents

Abstract

This thesis describes a numerical study of the electron transport through a quantum point contact in the ballistic limit. In the initial part of this study a time-dependent model was developed. This provided a qualitative analysis of the transport and highlighted the complex scattering processes at the contact-channel interface and the modal nature of the transport in the channel region of the quantum point contact.

To study the transport in more detail a coupled-mode time-independent analysis was developed and applied to various models of a quantum point contact with different approximations to the confining potential. This included an analysis of the transport through the disordered quantum point contact, which included the potential of the randomly distributed ionized donors in the calculation of the confining potential. This study shows that the random potential in a quantum point contact leads to rapid intermode scattering. The adiabatic approximation fails badly, but conductance can still be quantized through the less stringent conditions of 'compensated' scattering. This intermode scattering was found to reduce the sensitivity of the quantum point contact to the channel-contact coupling. The lack of adiabaticity in the transport can compensate for poor interface coupling of the channel modes through a process of forward intermode scattering. This non-adiabatic process can lead to the full occupancy of the lower conducting modes even when their initial coupling is poor.

The forward intermode scattering length in the disordered quantum point contact was found to be approximately 100 nm, which was in good agreement with the analytical scattering length based on the Born Approximation. However, an efficient three-stage indirect back-scattering process has been identified which cannot be described within the usual Born Approximation. If this represents the dominant back-scattering process in quasi-one-dimensional systems, then the mobilities calculated using the Born Approximation will be overstated.

If electron devices analogous to those of electromagnetic waveguides are to be produced, these scattering mechanisms must be eliminated. This represents a considerable engineering challenge

Content of Thesis

Chapter One provides an introduction to the thesis. This chapter describes the current state of conventional devices, introduces quantum device structures and in so doing outlines the motivation for this work.

Chapter Two outlines the experimental systems in which the semiconductor quantum point contacts are fabricated. It highlights the technological driving force behind the development of the AlGaAs-GaAs heterostructure systems that form the basis of semiconductor quantum point contacts.

Chapter Three describes various time-dependent approaches applied to the study of electron transport in the ballistic limit. This chapter includes a qualitative study of the transport through a quantum point contact.

Chapter Four details the development of a time-independent coupled-mode model of the electron transport in an electron waveguide. Particular attention is drawn to the problems of modal cut-off and the general numerical instability associated with the numerical integration of evanescent modes.

Chapter Five applies the time-independent coupled-mode model to different approximations of the quantum point contact. This coupled-mode approach allows a detailed analysis of each modal contribution to the flux at all points throughout the structure.

Chapter Six provides a detailed study of the electron transport through a realistic quantum point contact. The confining potential is based on a potential that includes the effects of the non-self-averaged randomly distributed ionized donors. The results of this coupled mode analysis are also compared with an analytical study based on the Born Approximation.

Chapter Seven briefly outlines the extension of the coupled-mode model to other related ballistic transport problems and suggests directions for future work.

Chapter Eight summarises the content and results of this thesis and discusses the conclusions in the context of potential device applications.

Publications

During the course of this research, various aspects of the work have been published:

Theory of Non-Linear Transport in Quantum Waveguides
Barker J.R., Pepin J., Finch M., Laughton M.J. *Solid State Electronics* **32** (1989) 1155

A Modal Analysis of Electron Transport in a Realistic Quantum Point Contact
Laughton M.J., Barker J.R., Nixon J.A., Davies J.H. *Phys Rev* **B44** (1991) 1150

Chapter One
Introduction

1.1 Background

The long-continued advance of the performance of information processing technologies has been based on the miniaturization of components (Keyes 1988).

Undoubtedly, this observation by Keyes is a restatement of a truth that is as important today as it was when humanity advanced from writing on cave walls to paper. However, more recently, the progress in miniaturization has been more rapid.

The current period of miniaturization began with the large relay computers developed in the 1940s. Inventions in the 1950s showed that electronic computation and storage could be performed using semiconductor devices, and the quest for higher operating speeds and lower power dissipation led to ever-smaller devices (*Keyes 1988*). The advent of planar processing methods around 1960 provided a massive impetus in the development of smaller devices. Currently, Very Large-Scale Integration (VLSI) circuits can contain *one million* active elements over an area of just a few square centimetres of semiconductor. The critical scale of the elements of these VLSI circuits are now shrinking to below 0.5 μm.

The advent of planar processing also introduced the first practical approach to reduce the dimensions available to the electrons in the semiconductor system. This was achieved by exploiting the channel of a MOSFET structure to provide a two–dimensional system. In 1986, Hartstein *(Hartstein 1986)* electrostatically confined the electron channel of a n-channel MOSFET to study the physics of a quasi-one-dimensional system. The recent developments in epitaxial growth techniques have enabled the production of AlGaAs-GaAs heterostructures (Chapter 2), in which the conducting electrons are confined to a two-dimensional Electron Gas (2DEG) through band gap engineering. This heterostructure system has formed the basis for the study of the physics of semiconductor Low Dimensional Systems (LDS). It is also being investigated as a basis of more traditional devices, where the high mobility of the 2DEG at low temperatures is exploited. This can be in excess of 1000 m^2/Vs, which gives a transport mean free path approaching 1mm *(Foxon 1989)*.

The continued advances of technology have enabled lateral confinement of the 2DEG on the same scale as the Fermi wavelength of the electron. The basic scales of the

conducting electrons in an AlGaAs heterostructure at low temperatures are defined by the Fermi wavelength, $\lambda_f \approx 50$ nm, and elastic mean free path, $l_{tot} \approx 1$ μm. In order to understand such structures, it is therefore necessary to take the wave nature of the electrons into account [1]. Such systems, in which the wave nature of the electron must be employed to gain an understanding of their operation, have been termed *Quantum Devices*. They cannot be described by semiclassical transport theory, which views electrons as particles that obey Newton's Laws. At low temperatures (< 4K) these quantum devices are ballistic, since the mean free path for dissipative scattering is much larger than the structural dimensions. In modelling these structures it is therefore reasonable to assume that all inelastic scattering processes take place in the contacts, and not in the actual active area of the device. Applying this assumption, the characteristics of a quantum device are determined by the transmission matrix which relates the input flux to the output.

1.2 The Quantum Point Contact (QPC)

The most basic building block of any quantum device is a short section in which the electrons in the 2DEG are laterally confined. The lateral confinement is comparable with the Fermi wavelength of the electrons. This leads to the creation of series of allowed transverse states or 'modes' which, dependent on their energy, the electrons may occupy. Such a system has analogies with electromagnetism and so has been termed an 'electron waveguide'.

In 1988, groups at both Delft-Philips *(van Wees 1988)* and Cambridge *(Wharam 1988)* independently discovered that the conductance of a short section, ≈ 0.2μm, of electron waveguide connected to two contacts in the unconfined layer of the 2DEG heterostructure was quantized. The system, including the contact regions, has been termed a Quantum Point Contact (QPC). Both groups used the split-gate electrode method to control the width of the channel (see Chapter 2).

Figure 1.1 shows the result of measurements by Timp *et al (Timp 1989)*. This is equivalent to the first reported measurement of quantized conductance in a QPC performed by van Wees *et al.* The conductance is quantized in steps of $2e^2/h$ and is a function of the width of the constriction, as controlled by the gate voltage. When the gate voltage is made more negative, there is an increase in the depletion region under the split gates. This *squeezes* the channel, thereby reducing its width.

[1] In making this statement, it is already assumed that the quantum mechanical nature of the system has already been invoked to provide the electronic band structure and effective mass.

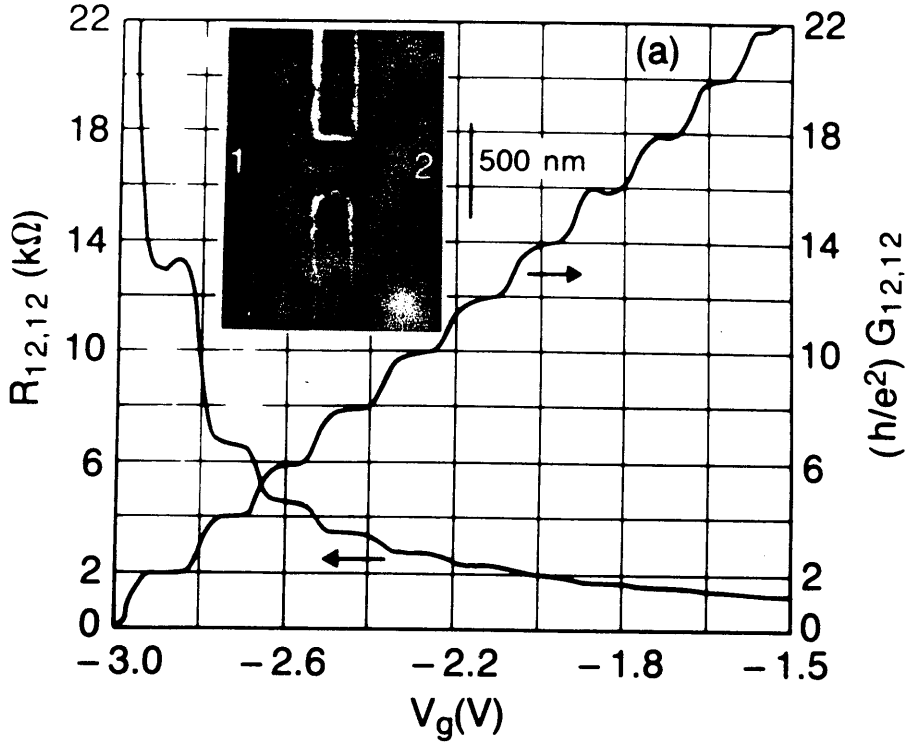

Figure 1.1 Measured conductance of a 0.2 μm QPC with good quantization, after Timp *et al (Timp 1989)*

The original analysis of this quantization (see Section 5.2) assumes both that each mode in the channel is perfectly coupled to the 2DEG contacts and also that there is no scattering in the modes inside the channel, the transport being assumed to be adiabatic *(Glazman 1988)*. This produces the quantized conductance in exact steps of $2e^2/h$. However, this is inconsistent with a numerical model *(Kirceznow 1989)* that included the interface between the contacts and the channel, which found that there was a resonant structure in the conductance.

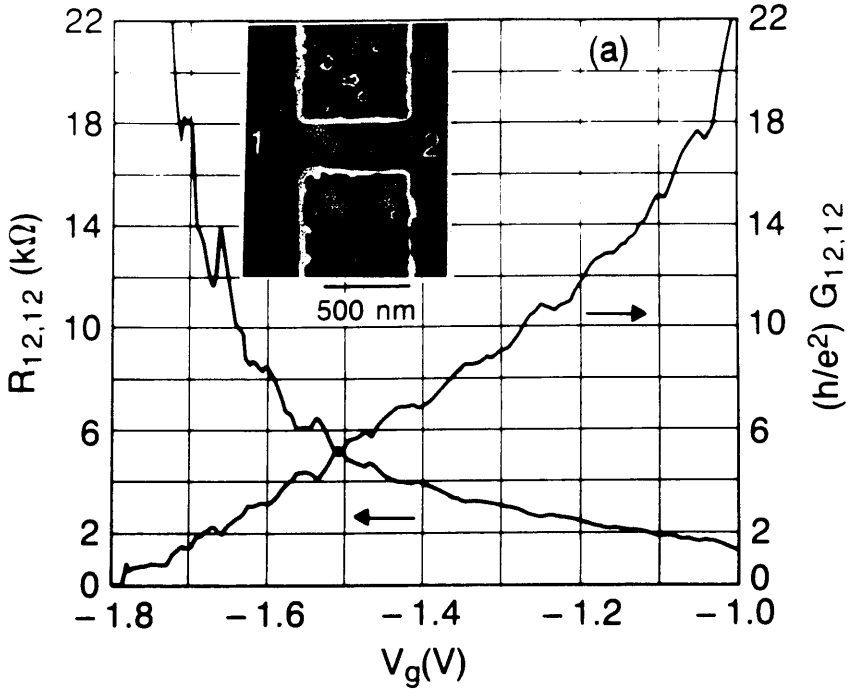

Figure 1.2 Measured conductance of a 0.6 μm QPC with no discernible quantization, after Timp *et al (Timp 1989)*

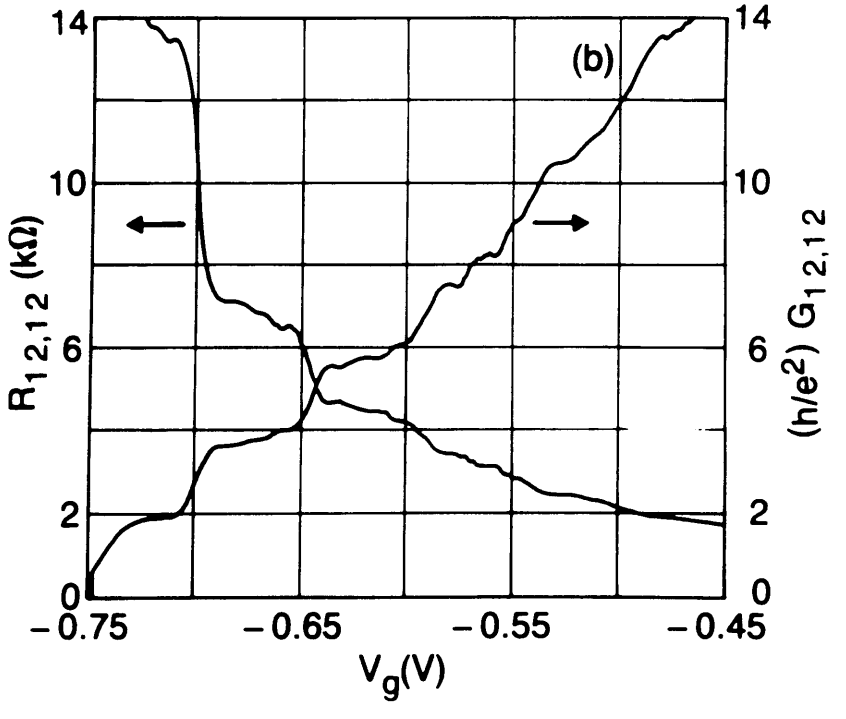

Figure 1.3 Measured conductance of a 0.6 μm QPC with low value quantization, after Timp *et al (Timp 1989)*

Further inconsistencies with the initial analysis of the transport in the QPC were uncovered when Timp *et al (Timp 1989)* observed the breakdown of quantized conductance in a QPC of length 0.6 μm (Figure 1.2), whilst other nominally identical structures showed signs of quantization only at low values of conductance (Figure 1.3). This was unexpected, as the channel length is still an order of magnitude less than the scattering length in a 2DEG. Also, earlier theory *(Sakaki 1980)* had predicted that the transport mean free path in a quasi-one-dimensional channel should be *greater* than that in a 2DEG.

1.3 Summary

The trend in electronic semiconductor devices has been towards ever increased miniaturization. As the line width of current devices is ≈ 0.5 μm, continued reduction in size may soon lead to the observation of new quantum device effects as secondary features in conventional devices. On this basis alone, quantum devices deserve understanding *(Landauer 1989)*, although they could also lead to an entirely new class of devices based on the quantum mechanical properties of electrons.

Currently there are a number of inconsistencies. The loss of quantization in a QPC of channel length 0.6 μm and the role of the channel-contact interface brings into question the basic assumptions underlying the transport in the well–quantized QPC of 0.2 μm channel length. In the following chapters, these inconsistencies are examined through the use of numerical models to study the electron transport through the QPC.

Chapter Two
Experimental Systems

2.1 Introduction

In this chapter the experimental system used in the study of electron transport through a QPC is discussed. The development of this area of semiconductor physics has been technology driven. It is only as a result of relatively recent advances in the growth of semiconductor materials using Molecular Beam Epitaxy (MBE) and fabrication of device structures using Electron Beam (E-Beam) lithography that this area of semiconductor physics has been opened up in LDS systems.

This chapter begins with a brief description of these two principal technologies and then describes the experimental system in which the QPC is fabricated.

2.2 Molecular Beam Epitaxy (MBE)

The MBE system may be thought of as a sophisticated evaporation chamber. The core of the system is an ultra-high vacuum growth chamber into which the substrate is loaded. Connected to this growth chamber are several evaporation cells which can supply, in a controlled manner, the various species in the form of a hot flux that may be required to be deposited on the substrate. The flux can be initiated or terminated in less than a second and the growth rate is of the order of 5Å per second. Provided that the lattice spacings of the various species evaporated onto the substrate are similar both to each other and also to the substrate, it is possible to grow a system of multiple crystalline layers with good lattice matching.

Another important technique more often associated with optoelectronic applications is Metallo-Organic Chemical Vapour Deposition (MOCVD), in which the substrate is exposed to a hot stream of gaseous compounds, such as $(CH_3)_3Ga$, $(CH_3)_3Al$ or AsH_3. The chemical reaction of these compounds at the growth surface leaves successive layers of the desired semiconductor.

2.2.1 The AlGaAs-GaAs system

A particularly important combination of materials used in the engineering of MBE layers, and that used in the fabrication of the QPC, is the AlGaAs-GaAs system. These two semiconductors are closely matched in lattice spacings, but their band structures differ. It has been shown *(see Collins 1986* for a summary*)* that the difference in the band structure can be approximated by an electrostatic potential, where the conduction band of the $Al_xGa_{1-x}As$ is approximately x eV above that of the GaAs (for $x \leq 0.35$).

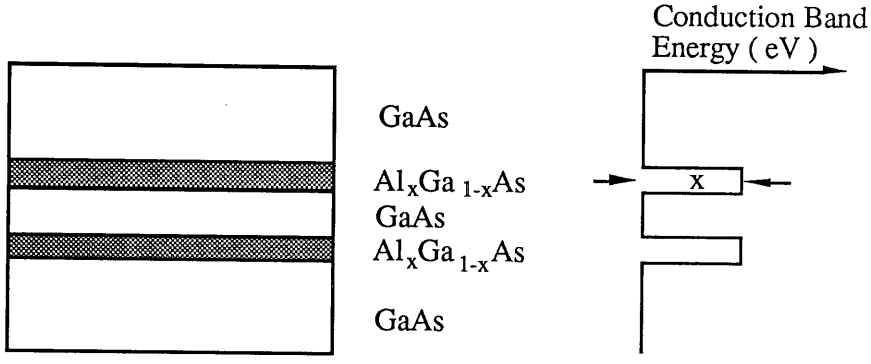

Figure 2.1 Conduction band profile of a AlGaAs-GaAs resonant tunnelling barrier

Figure 2.1 shows a resonant tunnelling barrier formed from alternate layers of AlGaAs and GaAs. If more potential barriers were added, the single resonant states of the tunnelling barrier would expand to form mini-bands of resonant or 'allowed' energies. This is analogous to the origins of the normal semiconductor bands, and can be engineered to produce a desired band structure. Such structures are called superlattices and have found widespread applications, particularly in the field of optoelectronics.

2.3 Electron Beam Lithography

The second technology important to the fabrication of semiconductor devices of sufficiently small size is Electron Beam lithography. This is based around a sophisticated electron gun, which can focus the electron beam down to a spot size of the order of 10Å in diameter. The electron beam moves around the surface of an electron-sensitive film or resist on the substrate. It is directed by deflection coils, controlled by a computer which has been programmed to produce the desired pattern.

The final stages of the fabrication follow those of normal photolithography, where the pattern written by the E-beam into the resist can be transferred to the substrate, or subsequent layers placed over the resist by a variety of techniques.

2.4 The Two-Dimensional Electron Gas (2DEG)

The first semiconductor two-dimensional electron gas (2DEG) was that of the inversion layer of a silicon MOSFET. More recently, the advent of MBE and MOCVD growth techniques have enabled the creation of a 2DEG in a AlGaAs-GaAs system.

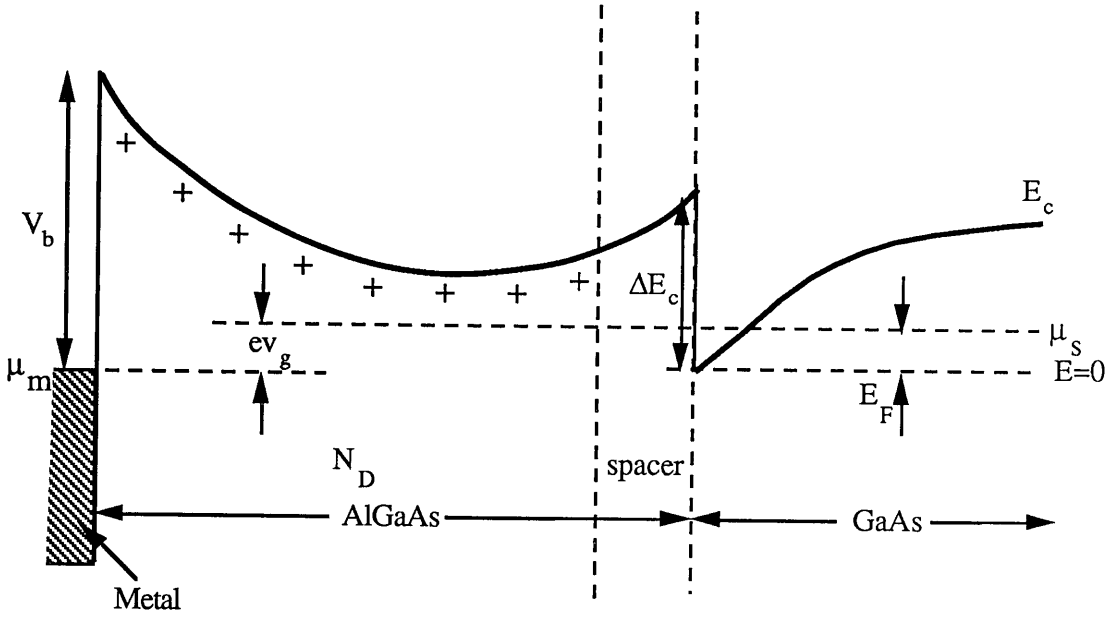

Figure 2.2 Conduction band of the heterostructure. The conduction band discontinuity creates a 2DEG at the interface of the AlGaAs and GaAs *(Davies 1987)*.

Figure 2.2 shows the conduction band of a AlGaAs–GaAs system that forms a 2DEG at the boundary of an undoped GaAs layer and an undoped AlGaAs spacer layer. The potential discontinuity at the surface results from the Schottky barrier potential between the the AlGaAs and the metal. Even if there is no metal contact there still exists a potential discontinuity at the surface as a result of the 'pinning' of the Fermi energy on the surface of the AlGaAs.

When in equilibrium, a well designed AlGaAs-GaAs heterostructure will have a roughly triangular well in the conduction band at the AlGaAs–GaAs interface below the Fermi energy of the system. Electrons from activated donors in the doped AlGaAs region of the structure diffuse into the interface well. Here they become trapped in one of the quantized subbands of the well, generally in a region within 10nm of the interface. In the experimental structures, the heterostructure is designed so that only the lowest quantized subband of the interface well is occupied. The donor electrons in the system are therefore confined in the direction perpendicular to the plane of the AlGaAs-GaAs interface, but are free to move in the plane of the interface, restricted only by the size of the system.

2.4.1 Properties of a 2DEG

The principal advantage of this heterostructure 2DEG over those formed in the inversion layers of silicon MOSFETs is the separation in real space of the conducting 2DEG electrons and the ionized donor impurity atoms.

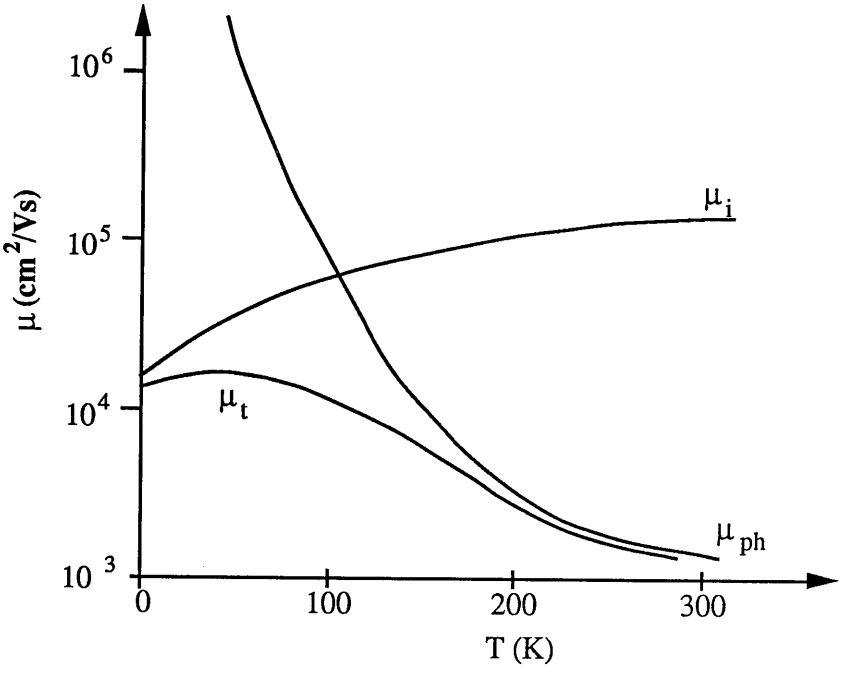

Figure 2.3 Temperature dependence of principal scattering mechanisms in bulk GaAs material *(Jaros 1989)*

The significance of this physical separation can be understood by reference to the major processes that restrict the electron mobility in a semiconductor (Figure 2.3). At high temperatures, the principal restriction on electron mobility (μ_t) is scattering with the lattice vibrations (μ_{ph}). The vibrational properties of semiconductor crystals do not vary greatly from material to material *(Jaros 1989)*. There is therefore very little that can be done to improve electron mobility at high temperatures.

However, at low temperatures, the electron mobility is limited by the scattering of electrons with the impurity atoms (μ_i). Unfortunately, the impurities are the very dopants that provide the conducting electrons in the system, and they therefore cannot be removed from the system. Ideally the impurity atoms and the conducting electrons should be physically separated. This is achieved in a AlGaAs-GaAs heterostructure, where an additional undoped AlGaAs spacer layer is introduced into the system. This is done in order to increase further the distance between the 2DEG and the ionized donors, and hence the mobility. However, if the spacer layer is made too wide, it can start to inhibit charge transfer into the undoped GaAs. A balance must therefore be achieved between

either high mobility but low carrier concentration, or else low mobility and high carrier concentration.

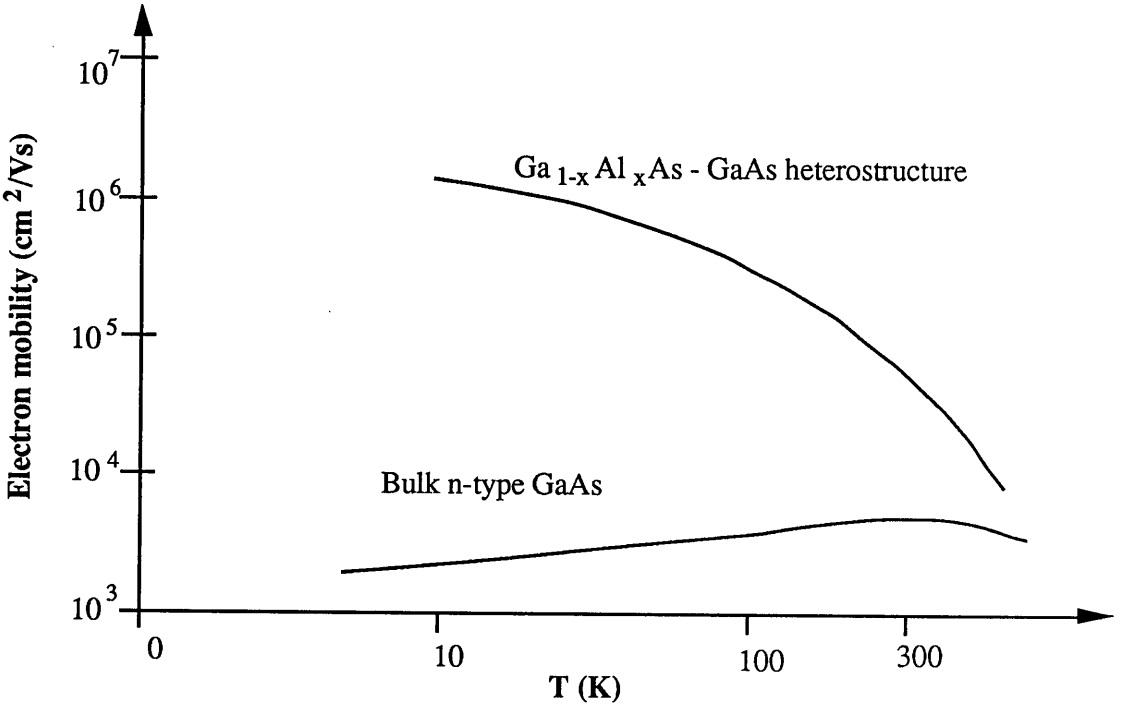

Figure 2.4 Temperature dependence of mobility in n-type bulk and 2DEG GaAs *(Jaros 1989)*

2.5 The Confinement of a 2DEG into a QPC

After the heterostructure has confined the electrons into a 2DEG, there are a variety of ways to further restrict the electron transport in the AlGaAs–GaAs system. The transport can become quasi-one-dimensional when the confining width becomes comparable with the Fermi wavelength of the 2DEG electrons. The various techniques of further confining the 2DEG are shown in Figure 2.5.

Lateral confinement can be achieved by full or partial etching of the material on either side of the required channel (Figure 2.5a). In the latter case, the reduction in the distance between the 2DEG and the pinned Fermi energy at the surface is sufficient to deplete the 2DEG of electrons. Ion bombardment (Figure 2.5b) can also be used to confine the electrons by damaging selected areas of the material, which leads to substantially reduced conductivity.

A further approach to confining the 2DEG is to use a patterned gate on the surface of the sample to deplete carriers in selected regions. This technique was used in the original discovery of the quantized conductance, and subsequently this approach has been used in nearly all experiments associated with the QPC. The widespread use of this approach, known as the 'squeezed' gate technique, stems from not having to damage the sample in confining the 2DEG, and by being able to dynamically adjust the confinement by changing the gate voltage.

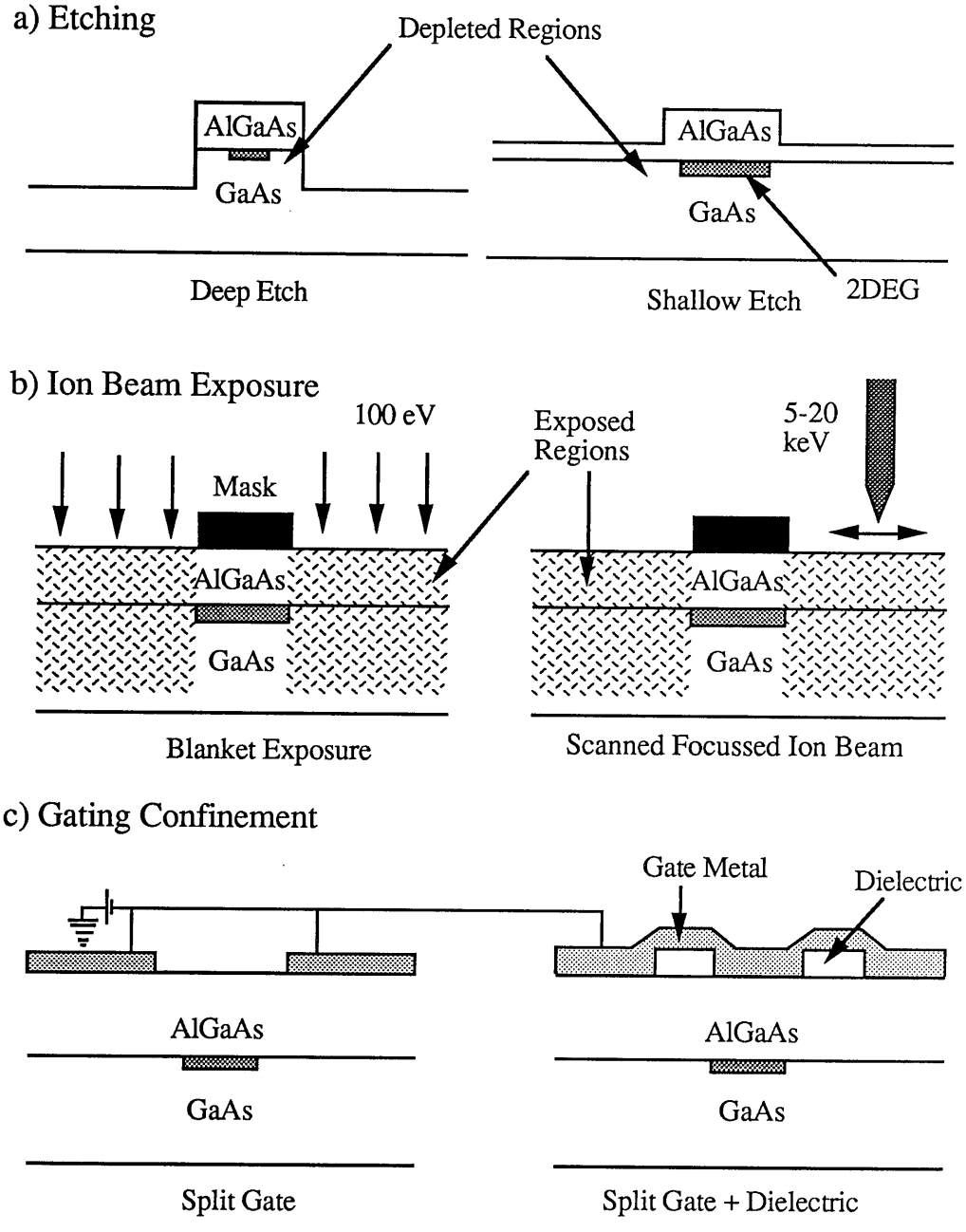

Figure 2.5 Techniques for the confinement of a 2DEG *(Thornton 1989)*

Figure 2.6 shows a schematic of the 0.6 μm QPC studied experimentally by Timp *et al. (Timp 1989)*. This structure was confined using the electrostatic 'squeezed gate' technique, and forms the basis of the model used to study the electron transport in realistic QPCs in Chapter 6. As can be seen from Figure 1.2, this structure has poor quantized conductance.

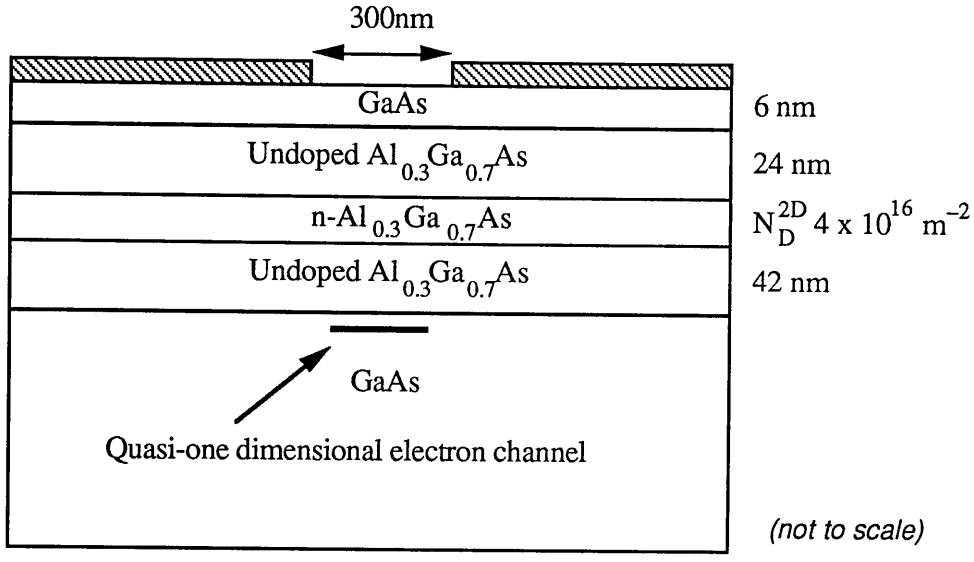

Figure 2.6 Schematic of the experimental structure modelled in Chapter Six *(Timp 1989)*

2.6 Summary

This chapter has provided a brief description of the principal technologies used in the preparation of LDS structures. The area of LDS has been seen to be technology driven and it is the recent advances in this technology which have allowed the growth and confinement of the 2DEG, formed at the band gap discontinuity of a semiconductor heterostructure.

The enhanced mobility of the 2DEG system at low temperature provides an excellent system in which to study semiconductor quantum ballistic transport in reduced dimensions, and is the basis of the experimental QPCs modelled in this work.

Chapter Three
Time–Dependent Analysis

3.1 Introduction

This chapter begins with the application of a one-dimensional solution of the Time-Dependent Schrödinger Equation (TDSE) to a qualitative study of scattering in one dimension. This numerical technique is then adapted using the Alternating Direction Implicit (ADI) method to solve the two-dimensional TDSE, which is then applied to the study of transport in the QPC.

The last part of this chapter describes the development of a novel monoenergetic quantum mechanical source, which can provide details in the study of time-dependent processes and provide time-independent solutions in its steady state.

3.2 One-Dimensional Time-Dependent Schrödinger Equation

The time evolution of a single particle non-relativistic quantum mechanical system is governed by the TDSE and the initial state of the system.

$$\mathbf{H}\psi(r,t) = i\hbar\frac{\partial\psi(r,t)}{\partial t} \tag{3.1}$$

where $\psi(r,t)$ is the wavefunction and $\mathbf{H}$ is the Hamiltonian of the system. For systems evolving in a continuum space, the TDSE belongs to a class of linear parabolic partial differential equations. The formal solution of this equation is

$$\psi(r,t) = \exp\left(-\frac{i}{\hbar}\mathbf{H}\,t\right)\psi(r,0) \tag{3.2}$$

In general, the explicit expression for the solution cannot be written down in closed form, and it is necessary to resort to numerical techniques to solve this initial value problem. Continuous space and time may be replaced by discretized approximations separated by Δx and Δt respectively. As usual in the discretization of a continuous problem, it is necessary to make a compromise between accuracy and computation effort, although the overriding criterion must be that of numerical stability.

Following Goldberg *et al (Goldberg 1969)*, the Crank-Nicholson scheme was considered. This scheme develops a propagating procedure by considering forward and backward propagation in time from the current position.

$$\psi^{n+1}(r) = \exp\left(-\frac{i}{\hbar}\mathbf{H}\Delta t\right)\psi^{n}(r) \tag{3.3}$$

$$\psi^{n-1}(r) = \exp\left(\frac{i}{\hbar}\mathbf{H}\Delta t\right)\psi^{n}(r) \tag{3.4}$$

where $\psi^{n}(r)$ is the wavefunction at r at time $n\Delta t$. Eliminating the term in $\psi^{n}(r)$ results in the equation

$$\exp\left(\frac{i}{\hbar}\mathbf{H}\Delta t\right)\psi^{n+1}(r) = \exp\left(-\frac{i}{\hbar}\mathbf{H}\Delta t\right)\psi^{n-1}(r) \tag{3.5}$$

Expanding the two exponentials to first order using the Taylor expansion results in an approximation for the time evolution operator, known as the Cayley approximation

$$\psi^{n+1}(r) = \left[\frac{\left(1-i(\Delta t/2)H/\hbar\right)}{\left(1+i(\Delta t/2)H/\hbar\right)}\right]\psi^{n}(r) \tag{3.6}$$

Potter *(Potter 1973)* has investigated the stability of this time operator using the Von Neumann stability criteria, which considers the growth of the Fourier modes present on the mesh of grid points. For stability, the modulus of the growth factor must always be less than or equal to unity. The growth factor G is defined as

$$G = \frac{U^{n+1}}{U^{n}} \tag{3.7}$$

where U^{n} is a Fourier amplitude at time $n\Delta t$. Application of this stability analysis to the Cayley operator produces *(Finch 1989)* a growth factor of

$$G = \frac{\left[1-i\left(2A\left\{1-\cos(k\Delta x)+2v_j\Delta t\right\}\right)\right]}{\left[1+i\left(2A\left\{1-\cos(k\Delta x)+2v_j\Delta t\right\}\right)\right]} \tag{3.8}$$

The modulus of this growth factor is always unity, which implies that errors will not grow exponentially, and therefore the time evolution operator is stable.

A second property of a time evolution operator is that it must be unitary. This is necessary in order that the normalisation of the wavefunction is preserved, and therefore that the wavefunction is neither created or destroyed. For the Cayley time evolution operator to be unitary $\mathbf{H}\,\mathbf{H}^{*} = 1$, where $\mathbf{H}^{*}$ is the Hermitian conjugate. With reference to Equation 3.6, this is clearly the case. The Cayley approximation is therefore a suitable time evolution operator, in that it is both stable and unitary.

The spatial discretization follows the well known finite difference method. The one-dimensional single particle Hamiltonian has the form

$$\mathbf{H} = \frac{-\hbar^2}{2m}\frac{\partial^2}{\partial x^2} + V(x) \tag{3.9}$$

where m is the effective electron mass, which is an approximation which is used throughout this work.

This is replaced by a finite difference form, where the continuous space has been replaced by a series of points separated by a distance Δx,

$$\mathbf{H} = \frac{-\hbar^2}{2m}\left[\frac{\psi_{j+1}^n - 2\psi_j^n + \psi_{j-1}^n}{\Delta x^2}\right] + \psi_j^n V_j \tag{3.10}$$

where ψ_j^n is the wavefunction at position $j\Delta x$ at time $n\Delta t$. Applying this discretization to Equation 3.6 produces the Crank-Nicholson discretized TDSE of the form

$$\psi_{j+1}^{n+1} + \psi_j^{n+1}\left[-\alpha + i\beta - 2\right] + \psi_{j-1}^{n+1} = -\psi_{j+1}^n + \psi_j^n\left[\alpha + i\beta + 2\right] + \psi_{j-1}^n \tag{3.11}$$

where $\alpha = \frac{-2m\Delta x^2 V_j}{\hbar^2}$ and $\beta = \frac{4m\Delta x^2}{\hbar\Delta t}$.

Provided that the initial state of the system, including the boundary conditions, are known, this equation can be rewritten as a tridiagonal matrix equation in the unknowns ψ_j^{n+1}. Standard sparse matrix techniques can be used *(Press 1987)* to obtain the wavefunction throughout the system at time step (n+1). The sparse nature of the matrix means that it can be efficiently solved in the order of N computation steps, where the matrix is of the size $N \times N$. This new wavefunction is then used as the initial conditions to determine the subsequent wavefunction. This numerical procedure is stable provided the criteria for mesh size and time step, outlined by Goldberg, are used.

3.2.1 Results of the One-Dimensional Model

Figures 3.1 and 3.3b illustrate various snap shots of the interaction of a gaussian wavepacket with a potential barrier, which represents a GaAs–AlGaAs–GaAs system. By Figure 3.3b, the wavepacket has finished interacting with the barrier and has split into two roughly equal packets, both of which are moving away from the barrier. The splitting of the probability density of the wavepacket represents the possible outcomes of

the interaction of the electron with the barrier. Either the electron tunnels through the barrier and continues with its forward motion, or else the electron is reflected.

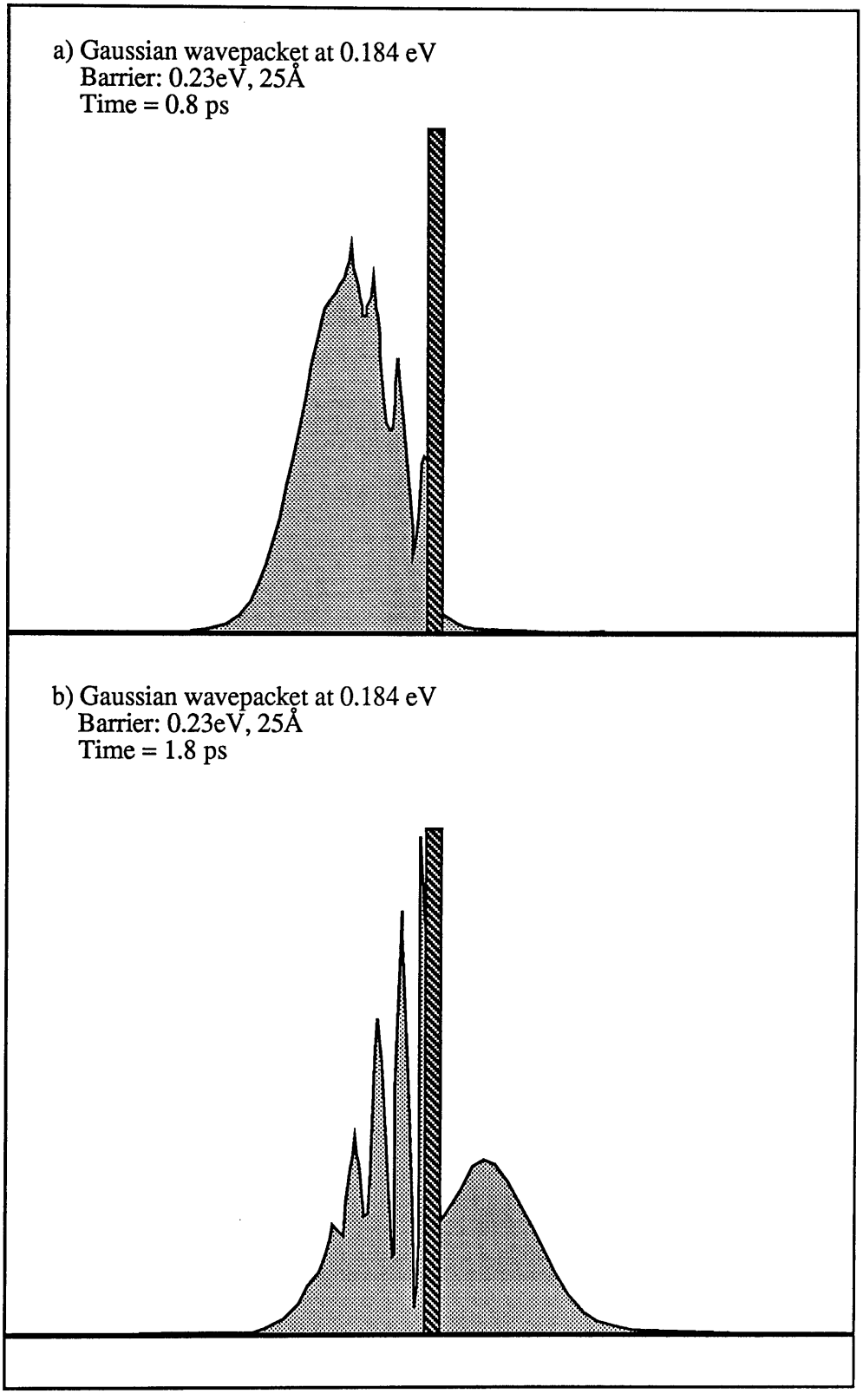

Figure 3.1 The interaction of a 0.184 eV gaussian wavepacket with a barrier. This barrier represents a AlGaAs tunnelling barrier in a GaAs system.

The probabilities of the electron being reflected or transmitted are determined by the relative areas of the transmitted and reflected probability density of the wavepackets, compared to the incident wavepacket. Since the evolution operator is unity, the total flux remains conserved and the sum of the transmitted and reflected wavepackets equals the incident wavepacket.

To confirm these results, a comparison was made between the numerical approach and a stationary state analytical calculation. In order to perform the analytical calculation, it is necessary to Fourier transform the initial wavepacket into k space using

$$F(k) = \frac{1}{\sqrt{2\pi}} \int_{-\infty}^{\infty} \Psi(x) \exp(ikx)\, dx \tag{3.12}$$

where the gaussian wavepacket is given by

$$\Psi(x) = \left[\frac{1}{\sigma\sqrt{\pi}}\right]^{1/2} \exp(ik_0 x) \exp\left(\frac{-x^2}{2\sigma^2}\right) \tag{3 13}$$

$$\text{This gives } F(k-k_0) = \left[\frac{\sigma}{\sqrt{\pi}}\right]^{1/2} \exp\left[\frac{-\sigma^2}{2}(k-k_0)^2\right] \tag{3.14}$$

The probability of transmission of each momentum (k) component was calculated from the standard plane wave transmission through a rectangular barrier, derived in any quantum mechanical text book *(Eisberg 1961)*. After applying these transmission coefficients to the k-space components, they were transformed back to real space in order to obtain the analytical transmission probability of the transmission through a barrier. A comparison of integrated wavepacket and analytical transmission probabilities is shown in Figure 3.2, from which the numerical technique is found to be in good agreement with the analytical results.

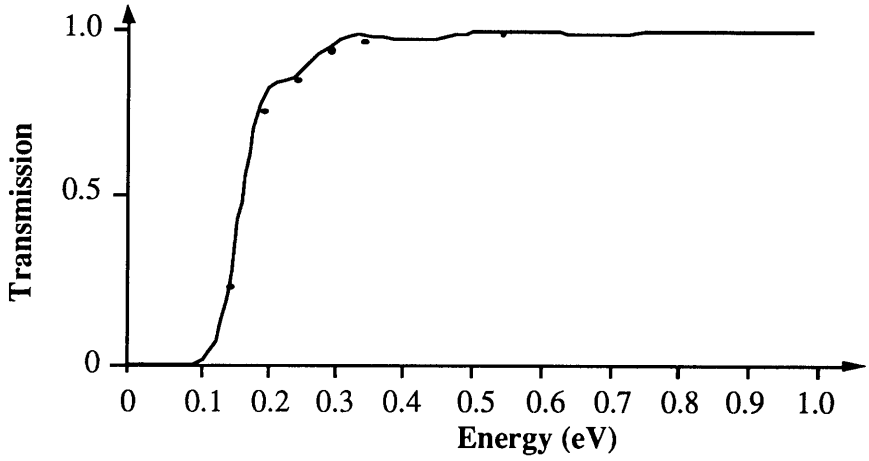

Figure 3.2 Comparison of the analytical (line) and time-dependent (points) calculations of the transmission probability of a gaussian wavepacket through a tunnelling barrier.

In Figure 3.3, the result of a wavepacket scattering with one barrier is compared with the same wavepacket interacting with two identical barriers.It is seen that more of the wavepacket scattering off the double barrier in Figure 3.3a is transmitted than in the single barrier case illustrated in Figure 3.3b. This increased transmission is due to the resonant tunnelling of the wavepacket whose energy coincided with the resonant energy of the double barrier system.

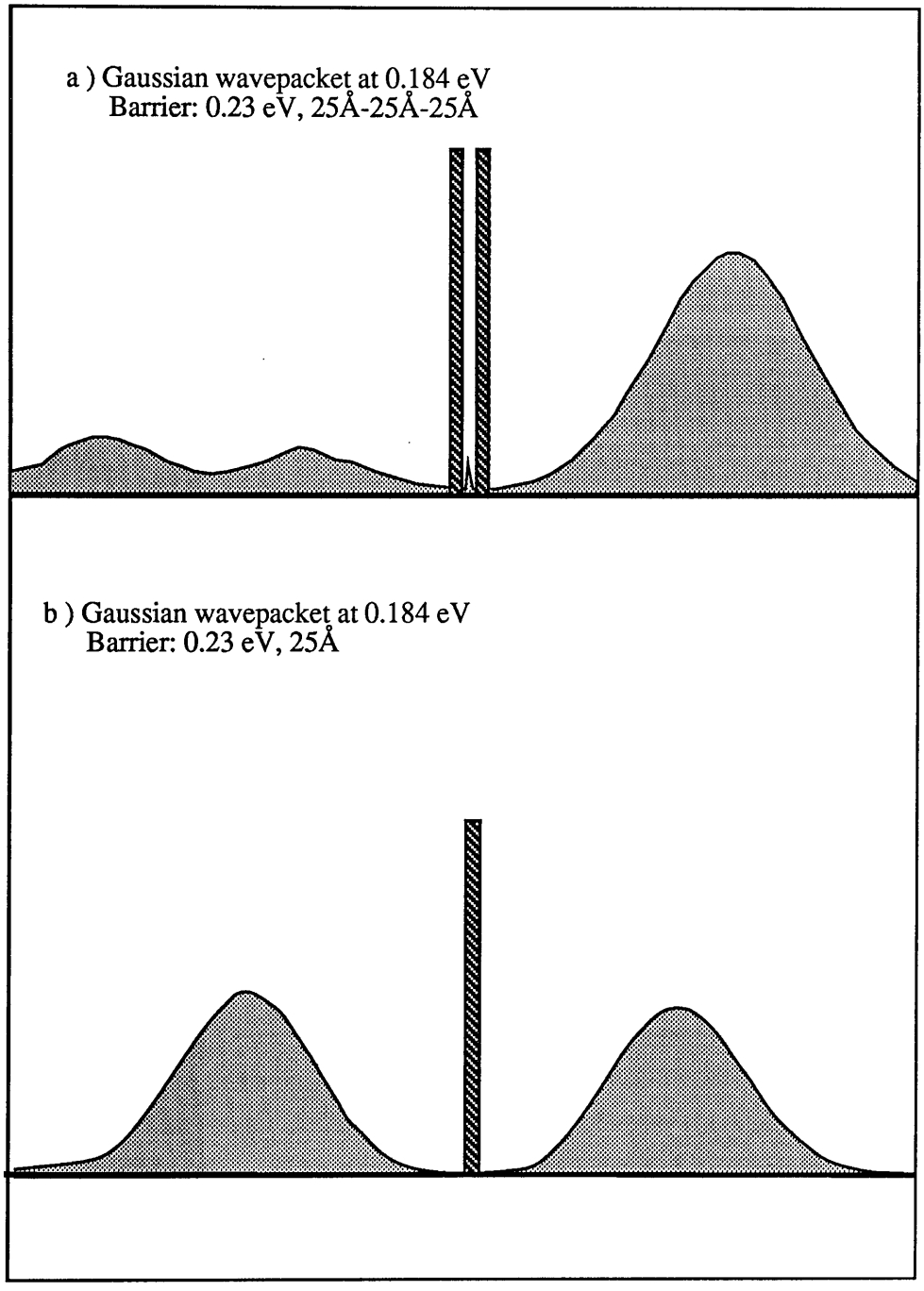

Figure 3.3 Comparison of 0.184 eV gaussian wavepacket passing through a single and double resonant barrier system.

3.3 Two-Dimensional Time-Dependent Schrödinger Equation

Following Finch *(Finch 1989)*, the one-dimensional Crank-Nicholson scheme is extended to two dimensions using the Alternating Direction Implicit (ADI) technique.

The ADI scheme is an operator–splitting approach, in which the full two-dimensional Hamiltonian $\mathbf{H}_{xy}$ is approximated by the sum

$$\mathbf{H}_{xy} = \mathbf{H}_x + \mathbf{H}_y \tag{3.15}$$

Applying the Cayley expansion yields the relation

$$\psi^{n+1} = \frac{(1-\mathbf{H}_x\tau-\mathbf{H}_y\tau)}{(1+\mathbf{H}_x\tau+\mathbf{H}_y\tau)}\psi^n, \text{ where } \tau = \frac{i\Delta t}{2\hbar}. \tag{3.16}$$

This expression can be factorized so that it resembles the product of two one-dimensional operators and, if an intermediate time position $\psi^{n+1/2}$ is introduced, the calculation can be broken down into the two stages

$$\psi^{n+1/2} = \frac{(1-\mathbf{H}_y\tau)}{(1+\mathbf{H}_x\tau)}\psi^n \tag{3.17}$$

$$\psi^{n+1} = \frac{(1-\mathbf{H}_x\tau)}{(1+\mathbf{H}_y\tau)}\psi^{n+1/2} \tag{3.18}$$

Finch has shown that at high magnetic field (> 1T) there is a loss of unitarity. However, in this zero magnetic field expansion, the method is stable under the same stability criteria as the purely one-dimensional system. The computation procedure is also very similar to the one-dimensional problem, although it is necessary to solve two tridiagonal matrices at each time step.

3.3.1 Results of the Two-Dimensional Model

The two-dimensional TDSE numerical technique detailed in Section 3.3 was used to study the transport through a QPC. The QPC was approximated as a uniform channel of zero energy in an otherwise impenetrable potential barrier (of several electron volts energy) connecting two large but finite contact areas (Figure 3.4). The incident electron was approximated as a gaussian wavepacket centred on the channel. It has only a forward component of energy, defined by the chosen electron energy.

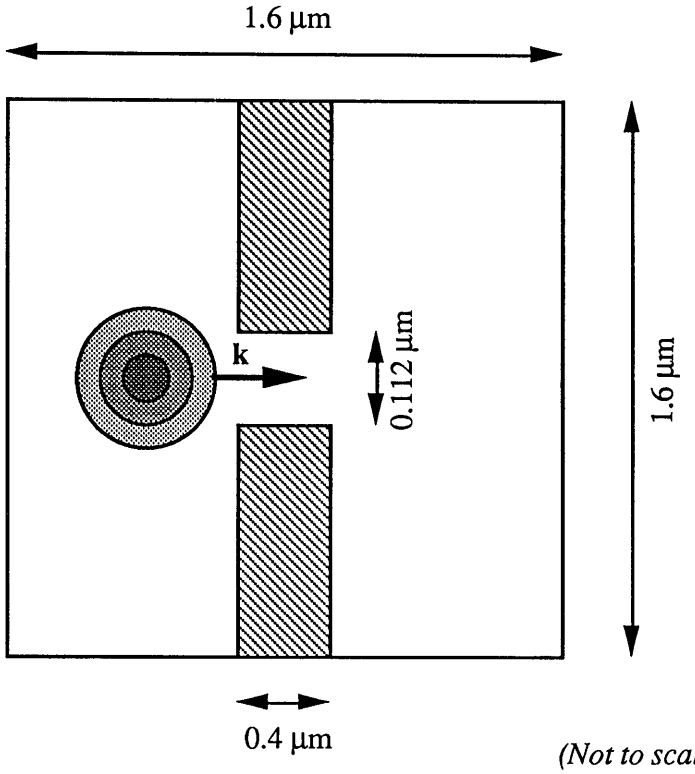

Figure 3.4 Schematic of the system used in the computation of the 2D TDSE.

Table 3.1 gives the modal energies of the channel assuming the 'particle in a box' approximation. This is reasonable, as the walls of the confining potential are very much larger than the electron energy.

Mode Number	Modal energies of the non-tapered channel (meV)	Modal energies of the tapered channel at the widest point (meV)
1	0.448	0.112
2	1.790	0.448
3	4.028	1.008
4	7.160	1.792
5	11.187	2.800

Table 3.1 Modal Energies of QPC channels used in the time-dependent study.

Table 3.1 shows quite clearly the significant effect of tapering the channel. At the interface with the contacts all of the five lowest modes in the tapered channel have energies below 3 meV. In comparison, only the first two modes of the non-tapered channel are in this energy range. Figures 3.5 to 3.8 show snap shots of the various states of an electron scattering through a QPC for both a uniform channel and a channel with rounded corners. In all cases there is no potential inside the channel.

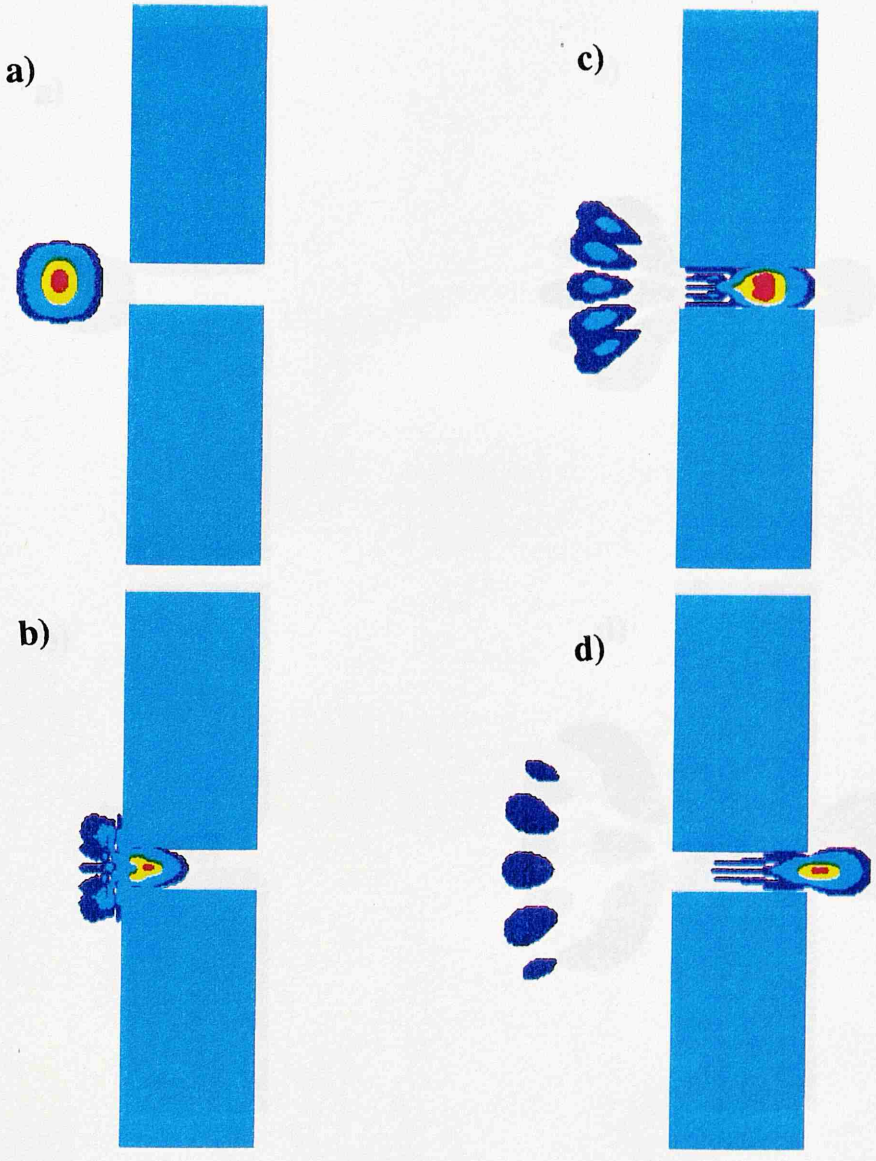

Figure 3.5 Various stages of the interaction of a 10 meV gaussian wavepacket with the non-tapered QPC a) t = 0, b) t = 1 ps, c) t = 2 ps, d) t = 4 ps.

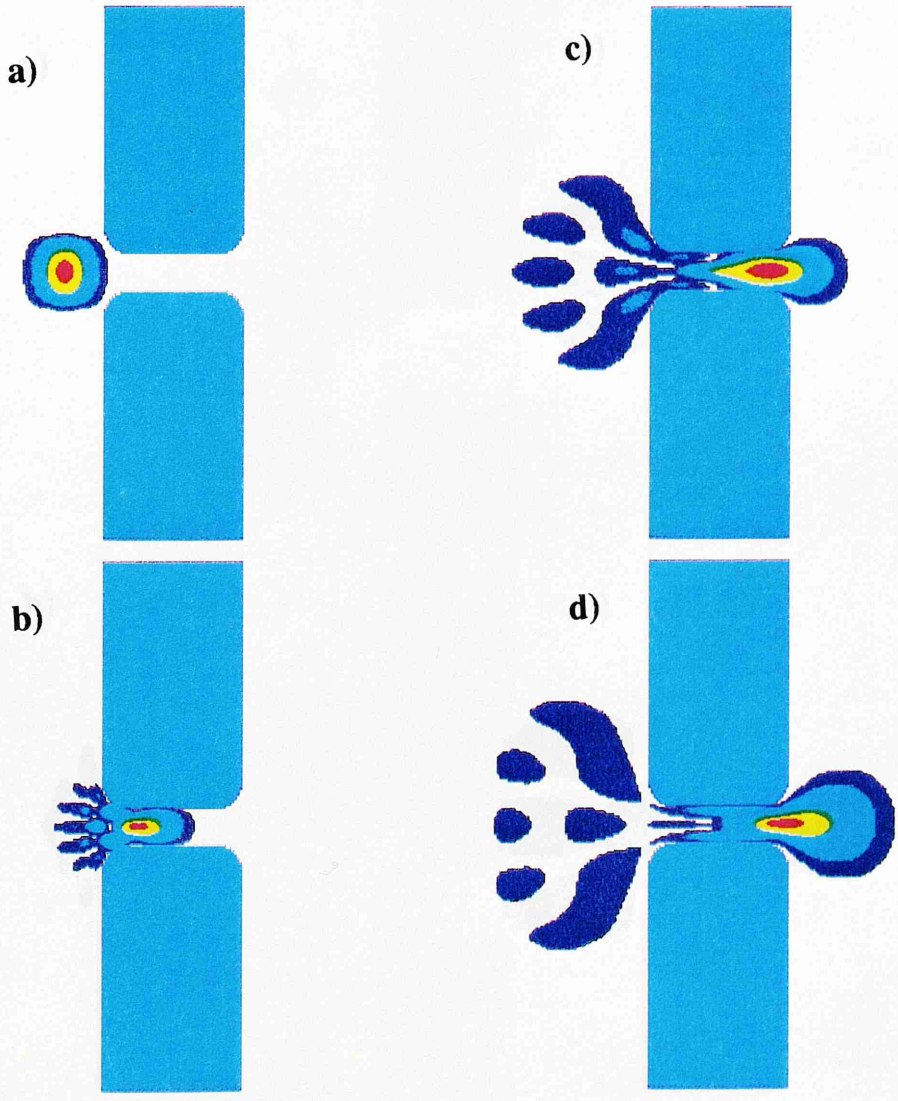

Figure 3.6 Various stages of the interaction of a 5 meV gaussian wavepacket with the tapered QPC a) t = 0, b) t = 2 ps, c) t = 4 ps, d) t = 5 ps.

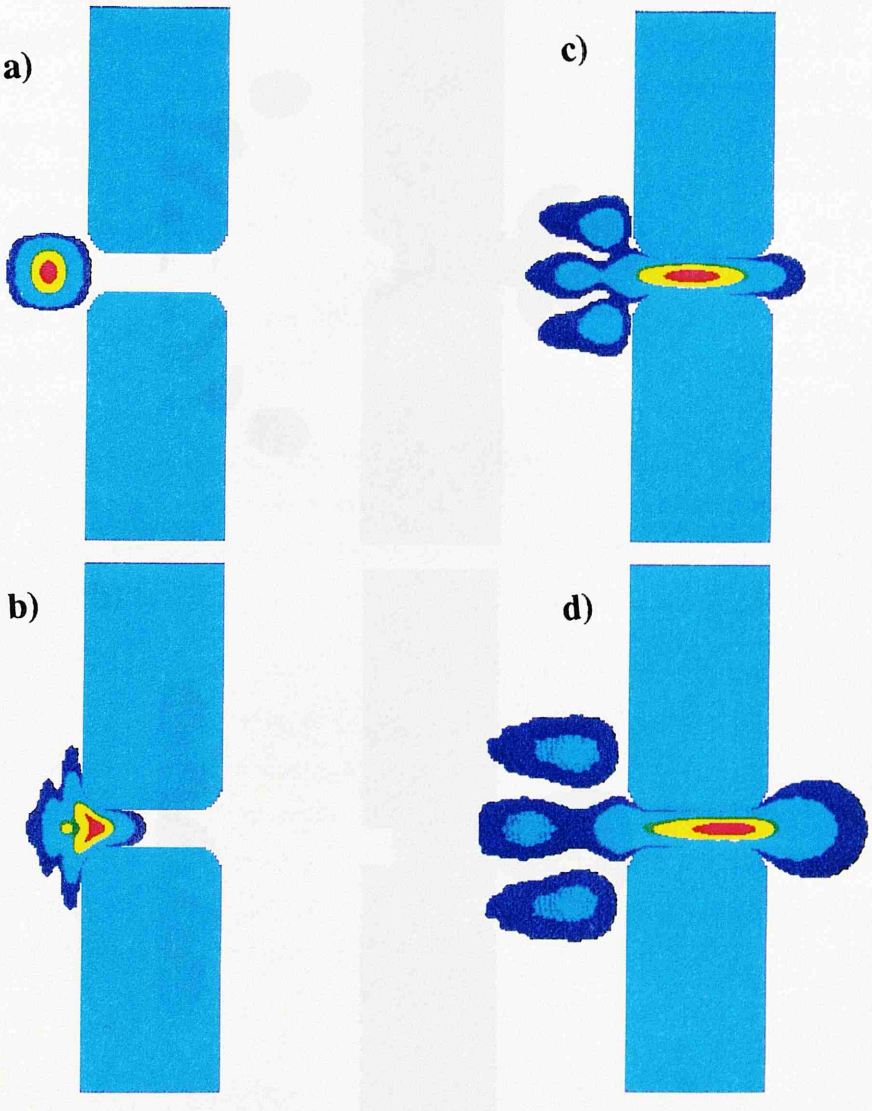

Figure 3.7 Various stages of the interaction of a 1 meV gaussian wavepacket with the tapered QPC a) t = 0, b) t = 2 ps, c) t = 5 ps, d) t = 7 ps.

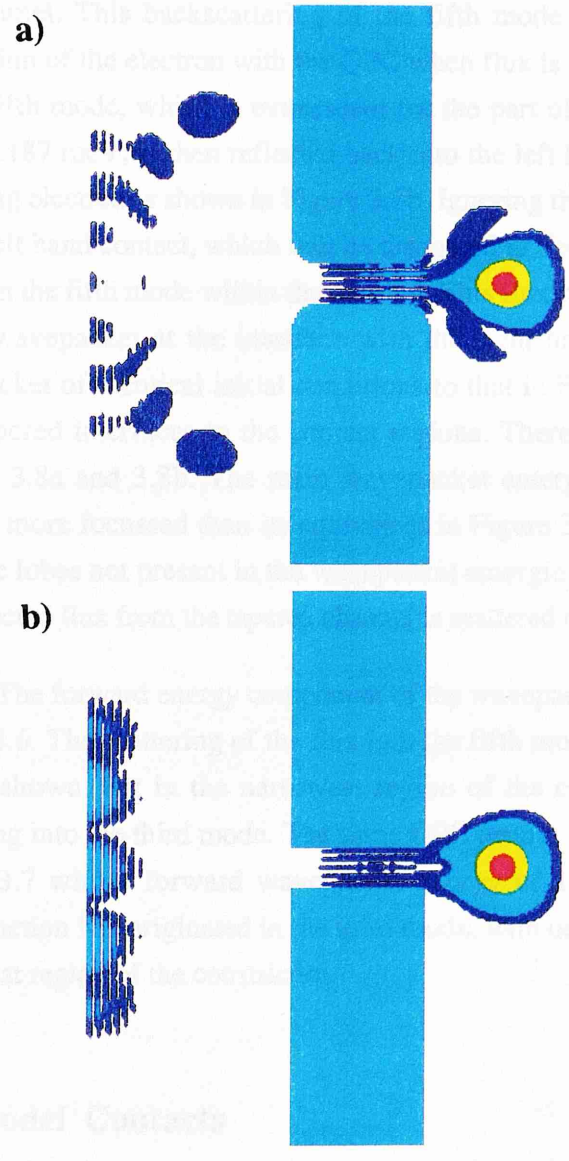

Figure 3.8 Comparison of the emerging 10 meV wavepacket from a tapered and non-tapered QPC at t = 5 ps (Note the interference of the reflected wavepacket as it scatters off the boundary of the calculated area).

By Figure 3.5c the principal part of the forward–travelling wavepacket has broadened. It shows signs of being scattered out of the lowest mode of the channel, whilst the tail of the wavepacket has been scattered into the fifth mode. As this electron begins to enter the right-hand contact, it has relaxed, with the main body in the lowest mode and the tail in the third mode (Figure 3.5d). The reflected wavefunction has scattered over a considerable angle and appears to have originated from the fifth mode of the channel. This backscattering of the fifth mode probably results from the initial interaction of the electron with the QPC when flux is scattered into this mode. This flux in the fifth mode, which is evanescent for the part of the wavepacket with energy less than 11.187 meV, is then reflected back into the left hand contact. A further plot of the emerging electron is shown in Figure 3.8b. Ignoring the interference of the reflected flux in the left hand contact, which will be discussed in Section 3.4, it can be seen that there is flux in the fifth mode within the channel. This flux probably results from the scattering of the wavepacket at the interface with the right hand contact. Figure 3.8a shows a wavepacket of identical initial conditions to that in Figure 3.8b emerging from a QPC with tapered interfaces to the contact regions. There is very little difference between Figures 3.8a and 3.8b. The main wavepacket emerging from the tapered channel is slightly more focussed than its equivalent in Figure 3.8b, although it has an additional two side lobes not present in the wavepacket emerging from the uniform channel. Also, the reflected flux from the tapered channel is scattered over a wider angle.

The forward energy component of the wavepacket has been reduced to 5 meV in Figure 3.6. The scattering of the flux into the fifth mode and its subsequent reflection is clearly shown, but in the narrowest region of the channel there is only evidence of scattering into the third mode. The same QPC profile has been used in the simulation of Figure 3.7 with a forward wavepacket energy of 1 meV. In this case the reflected wavefunction has originated in the third mode, with only the lowest mode evident in the narrowest region of the constriction.

3.4 Model Contacts

The interference of the reflected flux in Figure 3.8 results from artificial scattering off the boundary of the calculated area. In reality the contact area is much larger, but for calculation purposes it has been reduced. The time-independent boundary condition of $\psi = 0$ is used in the time evolution calculation. This results in the complete reflection of all flux that interacts with the boundary. Clearly this scattering is non-physical but, in order to make the calculation tractable, the grid of the calculation must be kept to a relatively

small size. Figure 3.8 illustrates this artificial reflection, which has not, however, made any impact on the overall scattering of the electron with the QPC at this point in time.

To overcome this problem of non-physical reflections, complex potential absorbers were placed at the boundaries. With a complex, wholly imaginary potential V_i, the quantum mechanical continuity equation becomes

$$\frac{\partial P(r,t)}{\partial t} + \nabla . \mathbf{S}(r,t) = -\frac{2V_i P(r,t)}{\hbar} \tag{3.19}$$

where P(r,t) is the position probability density and S(r,t) is the probability current density. Complex potentials have found similar applications in the fields of optics and nuclear physics *(Schiff 1968)*. The right hand side of Equation 3.19 acts as a source if V_i is negative, and as a sink if V_i is positive. Now, for positive V_i and $\nabla \mathbf{S} = 0$, the wavefunction is seen to decay as

$$\Psi \propto \exp\left[\frac{(-iE - V_i)\, t}{\hbar}\right] \tag{3.20}$$

As with real potentials, the imaginary potential does cause some backscattering of the wavefunction. It is impossible to eliminate backscattering totally, but it can be reduced to a minimum by allowing the complex potential to increase slowly in space. Complex potentials with gaussian 'tails' were therefore positioned at the boundaries of the system and, after some fine tuning of their shape and magnitude, they were found to function as adequate absorbers of the wavefunction, absorbing the majority of the wavefunction originally reflected from the system boundaries.

3.5 Quantum Mechanical Source

As already discussed, the usual boundary conditions consistent with the Crank-Nicholson scheme and the cause of boundary scattering are

$$\psi(\text{start}, t) = \psi(\text{end}, t) = 0 \qquad \text{for all times } t \geq 0. \tag{3.21}$$

However, a closer examination of the finite difference equations shows that the system can also be solved for a time-dependent boundary condition, provided that for all future times the flux at the boundary is known in advance. The boundary is described by some known external time-dependent function, for example a time-dependent plane wave source. Then, provided that there is no wavefunction incident on the boundary which has been reflected from the system, the wavefunction at the boundary is known for all future times. In order to prevent any reflections from the system altering the boundary value of

the known time-dependent function, the boundary is placed in a complex potential. This absorbs any reflected wavefunction before it reaches the boundary, but it also absorbs the flux transmitted into the system as it passes through this complex potential. It therefore becomes necessary to amplify the time–dependent source, so that there is sufficient flux entering the system after passage through the absorber. Figure 3.9 shows a schematic diagram of the quantum mechanical source placed in a complex potential. The only flux at the boundary is that transmitted into the system by the source. All reflected flux is absorbed by the complex potential. This is depicted below the x-axis in Figure 3.9.

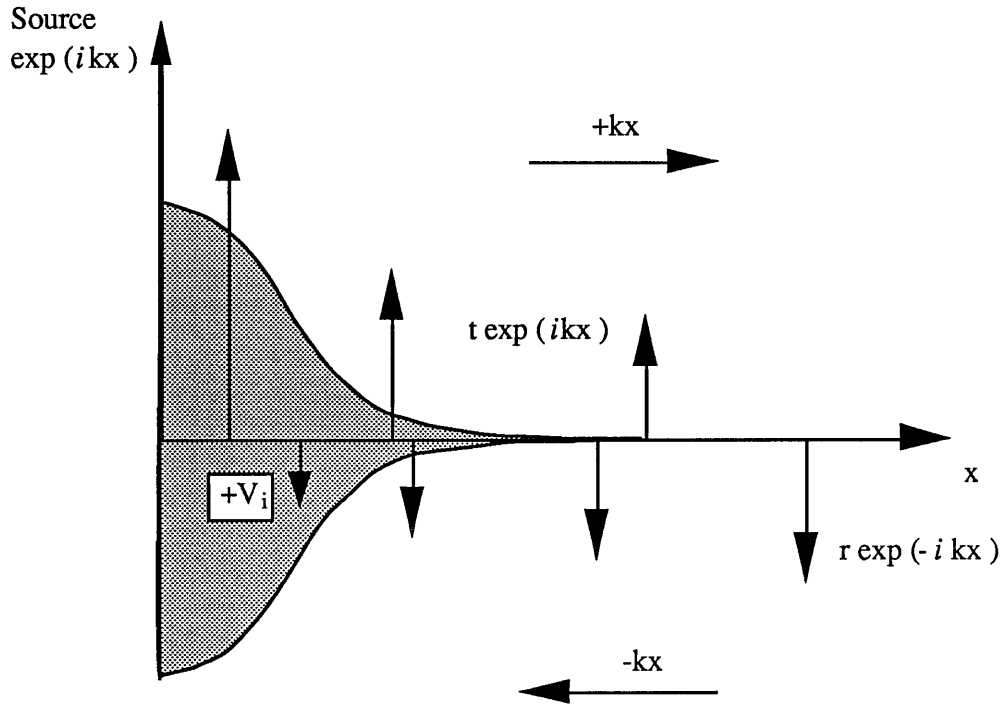

Figure 3.9 Schematic of Quantum Mechanical source protected from reflected flux by a complex potential.

Figure 3.10 shows the propagation of a monoenergetic plane wave source into the system. Since there were no scattering sites in the system and the right hand boundary was protected by an absorbing complex potential, there was no need to isolate the source in a complex potential. The injecting boundary may be considered, after Moshinsky *(Moshinsky 1976)*, as a beam of particles of momentum +k incident on a completely absorbing shutter given by the plane x=0. The wavefunction is then

$$\psi(x) = \begin{cases} \exp(ikx) & \text{if } x \le 0 \\ 0 & \text{if } x \ge 0 \end{cases} \qquad (3.22)$$

If at time t=0 the absorbing barrier is removed, the system evolves in accordance with the TDSE. The initial wavefunction incident in the system is expected to diffract in much the same way in which the wavepackets, on reaching the sharp edge potentials in Figure 3.1, show strong diffraction effects.

For such a monoenergetic system, Moshinsky has derived the propagation function

$$\Psi(x,t) = \frac{1}{\sqrt{2}} \exp\left(\frac{-i\pi}{4}\right) \exp\left[i\left(kx + \frac{1}{2}k^2 t \frac{\hbar}{m} \int_{-\infty}^{\varepsilon} \exp\left(i\frac{\pi}{2}u^2\right) du \right)\right] \tag{3.23}$$

where $u = (x' - x)(\pi t)^{-1/2} + k\left(\frac{t}{\pi}\right)^{1/2}$ and $\varepsilon = (\pi t)^{-1/2}(kt - x)$.

This is a Fresnel integral and the solution, after Moshinsky, is given by

$$\Delta x = 0.85\left[\frac{\pi\hbar t}{m}\right]^{1/2} \tag{3.24}$$

where Δx is the distance between the first points in which the probability density takes its stationary value. This has been found to be in good agreement with the numerical solution, an example of which is illustrated in Figure 3.10.

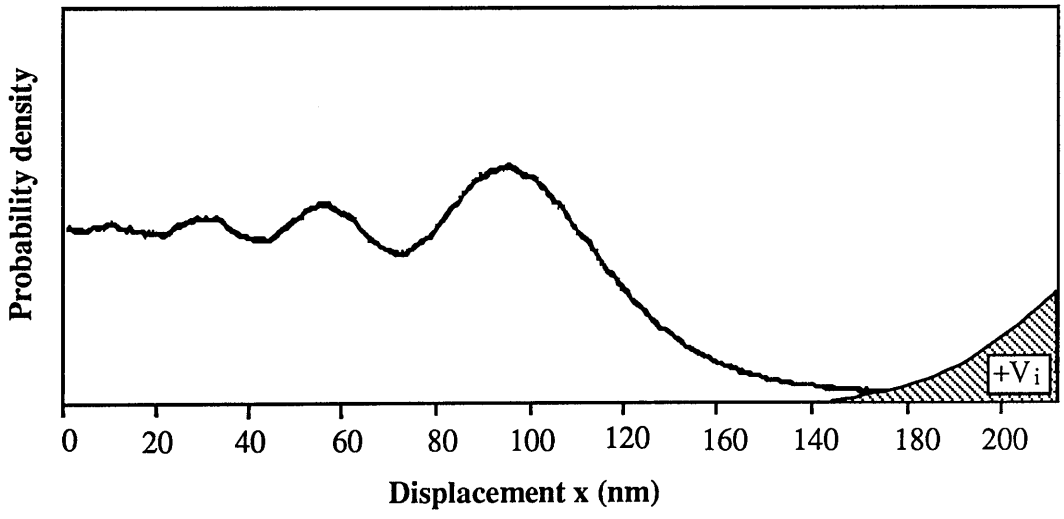

Figure 3.10 Evolution of a quantum mechanical source into a system at t=0.2 ps.

3.5.1 Application to One-Dimensional Resonant Tunnelling

A one-dimensional resonant double barrier consists of alternate layers of materials with differing energy bandgaps. The resulting conduction band profile (Figure 3.11) of the device resembles that of a text book quantum mechanics problem.

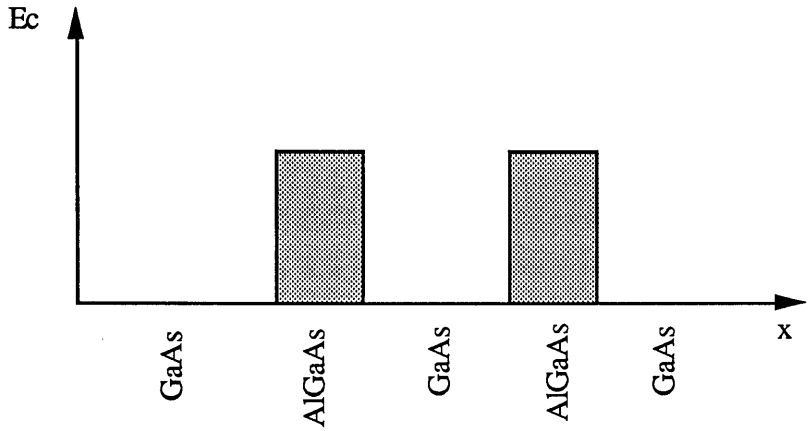

Figure 3.11 Schematic of the conduction band profile of an AlGaAs / GaAs resonant barrier system

Figure 3.12 shows the transmission probability of a 50-50-50Å AlGaAs-GaAs barrier system calculated using the transmission matrix method *(Thouless 1974)*. There is a sharp resonance with unity transmission at 0.08eV, which is well below the barrier height of ≈0.23eV. At this resonance energy the incident electron flux couples to that of a quasi-eigenstate of the potential well inside the double barrier system. Such a discrete resonance of a double barrier system provides an ideal test environment for the quantum mechanical source developed in Section 3.5.

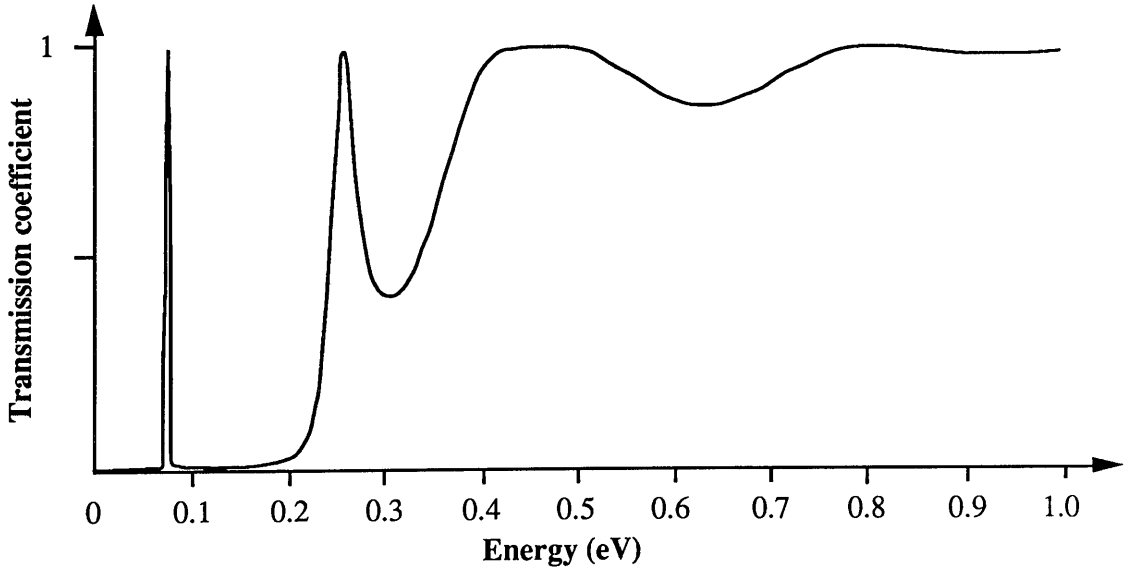

Figure 3.12 Transmission probability of a 50-50-50Å AlGaAs-GaAs barrier system

Figures 3.13 and 3.14 show various stages in the interaction of a monoenergetic source tuned to the resonant energy of a 50-50-50Å AlGaAs-GaAs double barrier system. In these figures the faint line represents the steady state of the source travelling through the system when there is no barrier present.

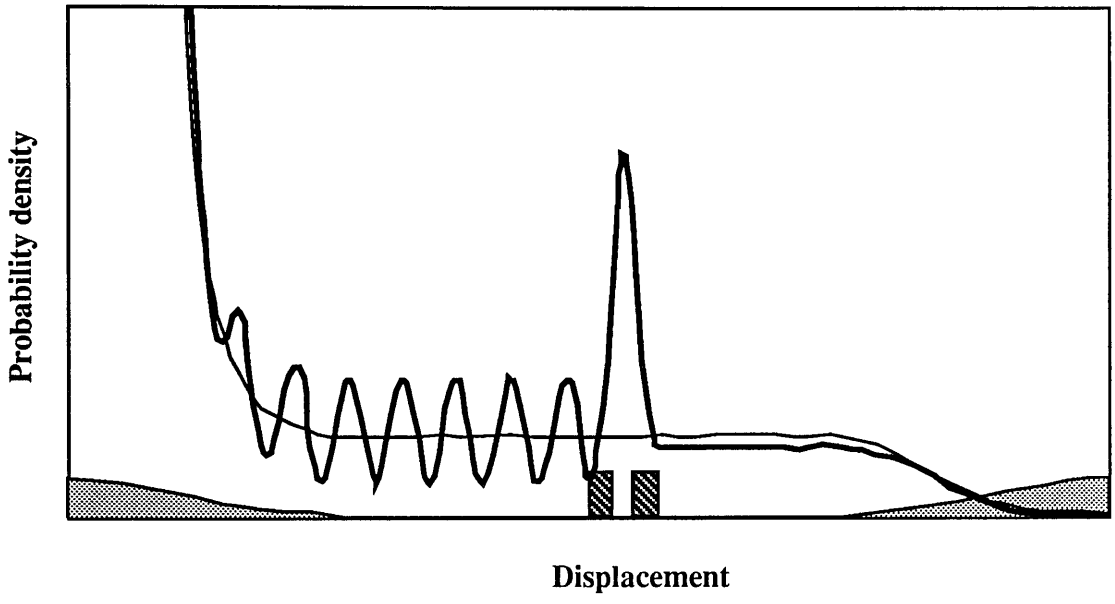

Figure 3.13 'Snap shot' of the build-up of resonance in a one-dimensional resonant tunnelling system. The faint line indicates the steady state of the system with no barrier system.

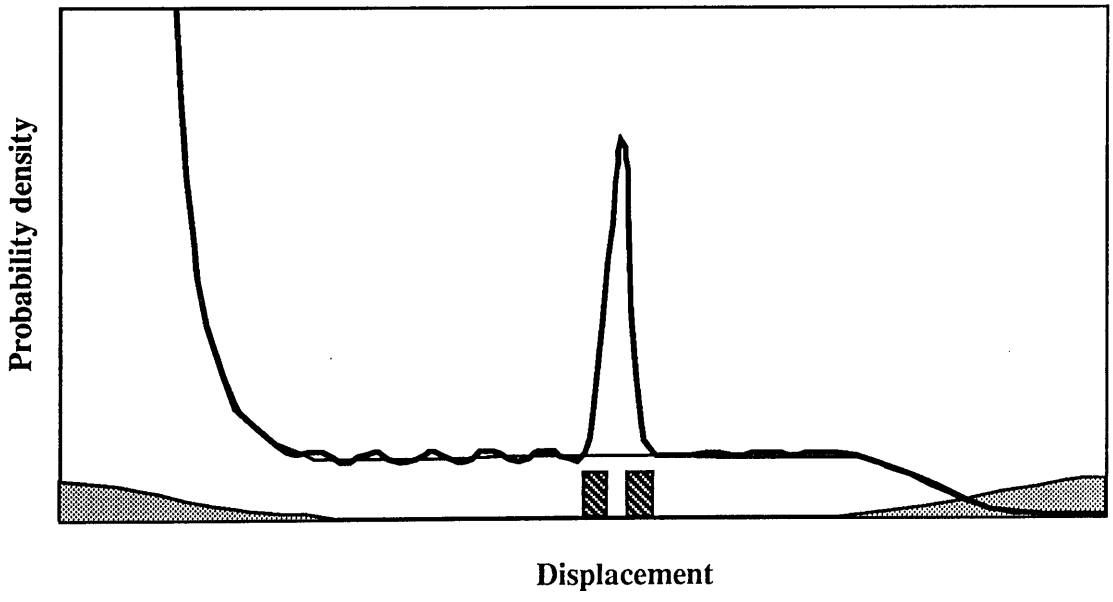

Figure 3.14 'Snap shot' of the build-up of resonance in a one-dimensional resonant tunnelling system close to the steady state.

The slight ripple on the steady state line indicates a small amount of back scattering from the complex potential absorbers, which are shown at either end of the system (not to scale). In Figure 3.13 the transmission from the double barrier has not reached unity, as defined by the steady state source with no barrier present, and there is considerable reflection from the barrier system. Figure 3.14 shows the same system at a later time, when the system has almost reached steady state with almost unity transmission through the double barrier and minimal reflected flux. Figure 3.15 shows the integrated probability density inside this system as the steady state is reached. The initial build up of flux inside the barrier is difficult to interpret due to the diffracted nature of the initial incident flux, as illustrated in Figure 3.10. However, Figure 3.15 also shows the decay of the flux out of the barrier system, which results after the source is turned off and no more flux enters the system. The decay of the flux inside the barrier system had an exponential time dependence. By standard theory, the decay is related to the half width of the resonance profile ΔE through

$$\psi \propto \exp\left(-\frac{t}{\tau}\right), \text{ where } \tau = \frac{\hbar}{\Delta E}. \tag{3.25}$$

The decay of the flux inside the barrier has been fitted to an exponential time constant of 0.56 picoseconds (Figure 3.15), which is consistent with the half width of the system's resonance profile.

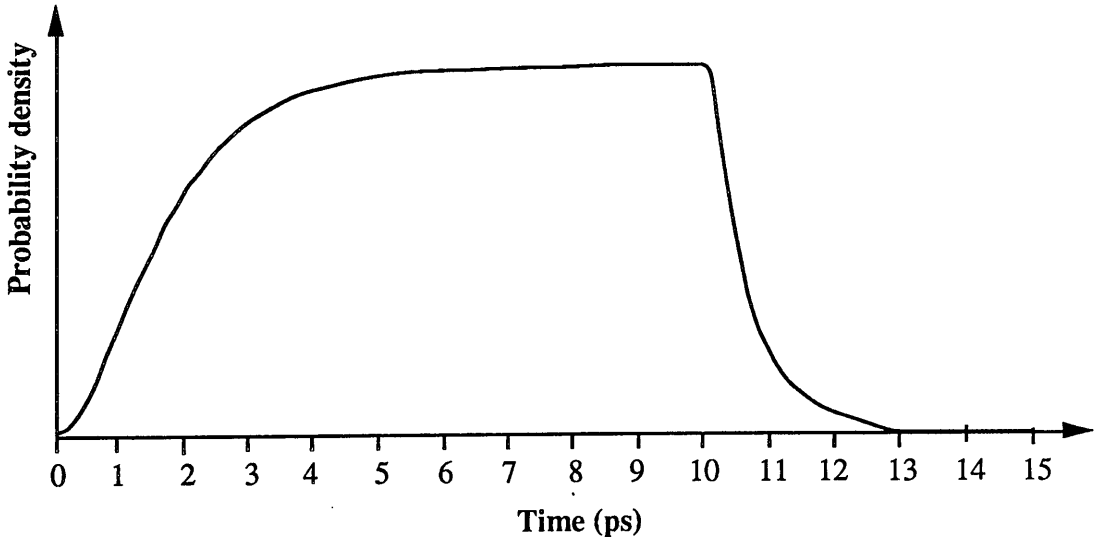

Figure 3.15 Probability density buildup and decay inside a barrier system.

3.6 Summary

A one–dimensional solution to the time–dependent Schrödinger Equation has provided a qualitative analysis of resonant tunnelling, in which the probability of the electron tunnelling through the resonant barriers is increased. It has also formed the basis of a two-dimensional time–dependent solution to the Schrödinger Equation.

This two-dimensional solution to the time–dependent Schrödinger Equation was briefly used in the analysis of transport through a QPC. In this model, the contacts were approximated by relatively large but finite regions of zero potential, and the QPC was approximated as a uniform narrow channel of zero potential in an otherwise impenetrable potential barrier.

The nature of the time-dependent calculation takes care of all scattering processes once the initial conditions have been set up. This is a significant advantage in terms of the calculation, but does not provide a full understanding of the scattering mechanisms. A superficial analysis of the transport was performed based on the predominant modal patterns evident in the wavepacket in the channel. Transmitted wavepackets were compared from channels both with and without tapered interfaces with the contacts. This might suggest that there was a small amount of wavepacket focusing in the former case, but this was inconclusive. For a fuller analysis of the scattering processes it would have been necessary to perform a Fourier analysis, in order to determine the time–dependent modal occupancies in the guide as the wavepacket passed through. However, even if this had been performed, it would still prove difficult to analyse the scattering mechanisms, due to the complex time–dependent nature of this wavepacket approach.

In this two-dimensional model, only the wavepacket with net forward momentum along the principal axis of the channel was considered. To model the full contact interaction with the QPC, it would be necessary to consider wavepackets incident on the channel from all possible angles, but this would have been prohibitive in the computational time required. This necessary requirement to model the contacts accurately draws a comparison with the work of Finch *(Finch 1989)*, who made a study of the Aharonov-Bohm (A-B) effect in semiconductor rings using a time–dependent wavepacket approach. In Finch's work, the time–dependent analysis only made a study of the electron transport around the ring under varying magnetic fields, and made no attempt to model the regions where the A-B ring made contact to the 2DEG contacts. This was possible, since the variation in the magnetic field made changes to a background resistance which always included the 2DEG-channel contact scattering. Therefore, provided that it can be assumed that there is no change in the contact scattering with changing magnetic fields, the 2DEG-channel interface can be ignored in the calculation.

In the latter part of this chapter, a novel time–dependent quantum mechanical source was developed with the use of complex potentials. A study was made of its initial diffraction as it entered into the system and its interaction when set to a resonant energy with a double barrier system. This provided evidence that the source did behave as a quantum mechanical flux. This source could be expanded to two dimensions and could prove useful in the study of time-dependent processes.

In conclusion, the time-dependent study of transport provided a qualitative introduction to transport through a QPC. It highlighted the complex scattering processes at the channel-contact interface and the modal nature of the transport inside the channel. However, a time-dependent approach was not considered a suitable technique to analyse these areas in detail. In addition, a quantum mechanical time–dependent source was developed, which could have been used to develop time–independent solutions as the steady state of the time–dependent solution. This approach would have had the advantage of producing a solution without detailed consideration of the scattering process but, unfortunately, would have required excessively large amounts of computer time. It was therefore decided to move to a time–independent approach for the study of transport in a QPC.

Chapter Four
The Coupled Mode Model

4.1 Introduction

In the last chapter, a time–dependent technique was developed and applied to the analysis of transport in mesoscopic systems. This study provided information on the general properties of electron transport. However, it was not considered a practical approach for a detailed analysis of the transport properties of a QPC, but instead indicated that a time-independent technique was more suitable.

This chapter describes a time–independent coupled mode approach to the study of electron transport in a QPC. The wavefunction in the channel is expanded in terms of the local eigenstates of the system, and variations in the channel parameters induce scattering between the various modes of the system. The latter part of the chapter is concerned with the problems of numerical instability, which are inescapable in a structure in which some modes are allowed to freely propagate, whilst others pass through cut-off and are reflected.

4.2 Local Modal Representation of Wavefunctions

Drawing on the analogy with electromagnetic radiation, the narrow channel, along which electrons travel in a QPC, can be thought of as an electron waveguide. Within this waveguide, it is a natural progression to expand the wavefunction in terms of the local eigenfunctions, or modes, of this confining potential. The local potential is very much larger than the electron energy, so that it is not necessary to consider any leaky or radiation modes. In this respect the electron waveguide differs from that of an electromagnetic wave (*Ansbro 1989*).

The first self-consistent calculations of the potential seen by electrons in a squeezed gate waveguide were performed by Kumar *et al* (*Kumar 1989*). Their results show that the confinement potential can be treated as a parabolic potential for low electron densities, but that this becomes increasingly more flat-bottomed as the electron density increases.

For this initial phase of the time–independent study, it was decided to use a parabolic function to describe the potential. This is because such a potential offered a reasonable approximation to the actual potential, and has known eigenfunctions that would enable an analytical approach in the first instance.

Figure 4.1 shows a schematic representation of the initial waveguide considered. Within the model there is freedom for the characteristics of the parabolic potential to vary as well as the local axial potential, V(x).

$$V(x,y) = \frac{1}{2} m\omega^2(x) y^2 + V(x) \tag{4.1}$$

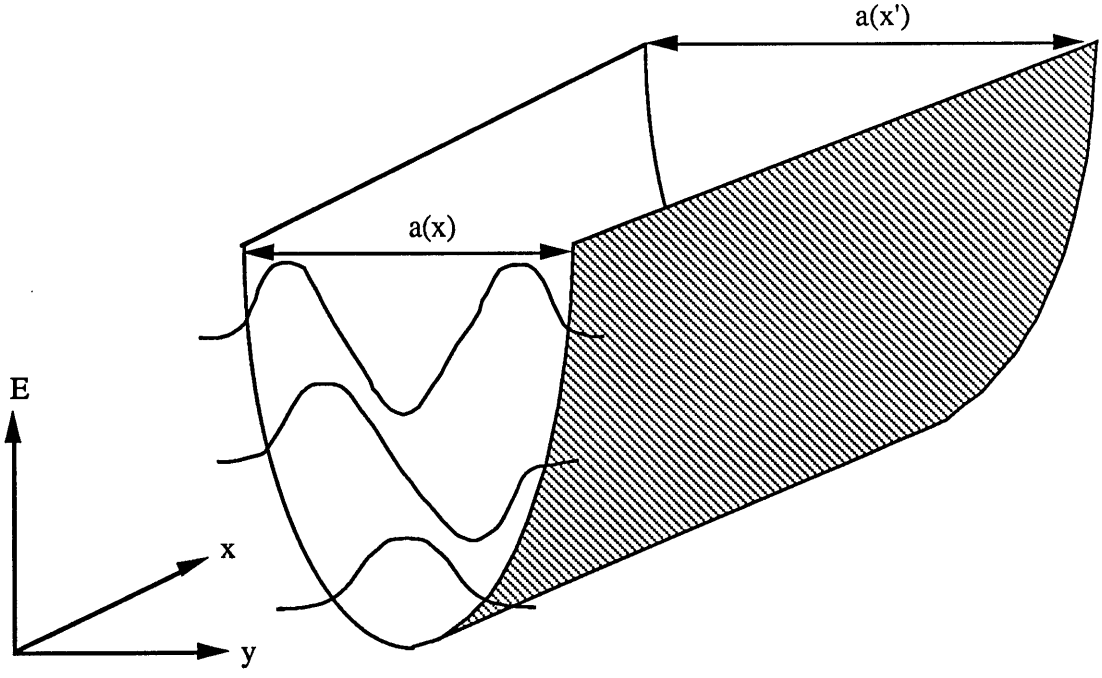

Figure 4.1 Schematic of analytic electron waveguide

The full two-dimensional time-independent Schrödinger Equation of the waveguide system is then given by

$$\sum_n \left[\frac{-\hbar^2}{2m} \left(\frac{\partial^2}{\partial x^2} + \frac{\partial^2}{\partial y^2} \right) + \frac{1}{2} m\omega^2(x) y^2 + V(x) \right] \psi_n(x)\,\phi_n(y) = \psi_n(x)\,\phi_n(y) E_{TOT} \tag{4.2}$$

The local wavefunction $\Psi(x,y)$ has been expanded as

$$\Psi(x,y) = \sum_{m=1}^{\infty} \psi_m(x)\phi_m(y) \tag{4.3}$$

where $\phi_n(y) = 2^{-n/2}(n!)^{-1/2}\left(\frac{m\omega(x)}{\hbar\pi}\right)^{1/4}\exp\left(\frac{-m\omega(x)y^2}{2\hbar}\right)H_n\left(\sqrt{\frac{m\omega(x)}{\hbar}}\,y\right)$ (4.4)

This local transverse eigenfunction of the parabolic confining potential satisfies

$$\left[\frac{-\hbar^2}{2m}\frac{\partial^2}{\partial y^2} + \frac{1}{2}m\omega^2(x)y^2\right]\phi_n(y) = \varepsilon_n\,\phi_n(y), \text{ with } \varepsilon_n = \hbar\omega(x)(n+\tfrac{1}{2}). \tag{4.5}$$

The longitudinal component of the local mode $\psi_n(x)$ is given by

$$\psi_n(x) = \psi_n^+ + \psi_n^- = c_n^+\exp(ik_n x) + c_n^-\exp(-ik_n x) \tag{4.6}$$

and $k_n = \sqrt{2m(\varepsilon_{TOT} - V(x) - \varepsilon_n)/\hbar^2}$. (4.7)

Applying the results of Equation 4.3 to Equation 4.2 gives

$$\sum_n \frac{-\hbar^2}{2m}\left[\phi_n\frac{\partial^2\psi_n}{\partial x^2} + 2\frac{\partial\psi_n}{\partial x}\frac{\partial\phi_n}{\partial\omega}\frac{\partial\omega}{\partial x} + \psi_n\frac{\partial^2\phi_n}{\partial\omega^2}\left(\frac{\partial\omega}{\partial x}\right)^2 + \psi_n\frac{\partial\phi_n}{\partial\omega}\frac{\partial^2\omega}{\partial x^2}\right]$$

$$+ \psi_n\phi_n V(x) + \psi_n\phi_n(\varepsilon_n - \varepsilon_{TOT}) = 0 \tag{4.8}$$

which is a system of n second order partial differential equations.

In the next stage of simplifying this equation, the known recursive properties of the Hermite function *(Arfken 1970)* in Equation 4.4 are exploited to expand $\partial\phi_n/\partial\omega$ and $\partial^2\phi_n/\partial\omega^2$. This leads to

$$\frac{\partial\phi_n}{\partial\omega} = \left(\frac{1}{4\omega} - \frac{my^2}{2\hbar}\right)\phi_n + y\left(\frac{nm}{2\hbar\omega}\right)^{1/2}\phi_{n-1} \tag{4.9}$$

$$\frac{\partial^2\phi_n}{\partial\omega^2} = \left(\frac{-3}{16\omega^2} - \frac{my^2}{4\hbar\omega} + \frac{m^2y^4}{4\hbar^2}\right)\phi_n - \frac{my^3}{\hbar}\left(\frac{nm}{2\hbar\omega}\right)^{1/2}\phi_{n-1} + y^2\frac{m}{2\hbar\omega}(n(n-1))^{1/2}\phi_{n-2} \tag{4.10}$$

When these equations are substituted into Equation 4.8, the following equation results:

$$\sum_n \frac{-\hbar^2}{2m}\left\{\phi_n\frac{\partial^2\psi_n}{\partial x^2}+2\frac{\partial\psi_n}{\partial x}\frac{\partial\omega}{\partial x}\left[\left(\frac{1}{4\omega}-\frac{my^2}{2\hbar}\right)\phi_n+y\left(\frac{nm}{2\hbar\omega}\right)^{1/2}\phi_{n-1}\right]\right.$$

$$+\psi_n\left(\frac{\partial\omega}{\partial x}\right)^2\left[\left(\frac{-3}{16\omega^2}-\frac{my^2}{4\hbar\omega}+\frac{m^2y^4}{4\hbar^2}\right)\phi_n-\frac{my^3}{\hbar}\left(\frac{nm}{2\hbar\omega}\right)^{1/2}\phi_{n-1}+y^2\frac{m}{2\hbar\omega}(n(n-1))^{1/2}\phi_{n-2}\right]$$

$$\left.+\psi_n\frac{\partial^2\omega}{\partial x^2}\left[\left(\frac{1}{4\omega}-\frac{my^2}{2\hbar}\right)\phi_n+y\left(\frac{nm}{2\hbar\omega}\right)^{1/2}\phi_{n-1}\right]\right\}+\psi_n\phi_n(\varepsilon_n+V(x)-\varepsilon_{TOT})=0 \qquad (4.11)$$

The next stage in obtaining the characteristic equation of a mode in the system is to use the orthonormality of the local transverse modes of the system by multiplying Equation 4.11 by

$$\int_{-\infty}^{\infty}\phi_\beta(y)\,dy \qquad (4.12)$$

and applying the known results of the various overlap integrals *(Wilson 1955)*.

This overlap integral projects out the characteristic equation of the mode β. Having performed this integration and simplified the n-coupled equations, these reduce to coupled mode equations of the form

$$\frac{\partial^2\psi_\beta(x)}{\partial x^2}+\psi_\beta\left[k_\beta^2-\left(\frac{\partial\omega}{\partial x}\right)^2\frac{(\beta^2+\beta+1)}{8\omega^2}\right]+\psi_{\beta-2}\left[-\frac{\partial^2\omega}{\partial x^2}\frac{[\beta(\beta-1)]^{1/2}}{4\omega}+\left(\frac{\partial\omega}{\partial x}\right)^2\frac{1}{4\omega^2}[\beta(\beta-1)]^{1/2}\right]$$

$$+\frac{\partial\psi_{\beta-2}}{\partial x}\left[-\frac{[\beta(\beta-1)]^{1/2}}{2\omega}\left(\frac{\partial\omega}{\partial x}\right)\right]+\psi_{\beta+2}\left[\frac{\partial^2\omega}{\partial x^2}\frac{[(\beta+1)(\beta+2)]^{1/2}}{4\omega}-\left(\frac{\partial\omega}{\partial x}\right)^2\frac{[(\beta+1)(\beta+2)]^{1/2}}{4\omega^2}\right]$$

$$+\frac{\partial\psi_{\beta+2}}{\partial x}\left[\frac{\partial\omega}{\partial x}\frac{[(\beta+1)(\beta+2)]^{1/2}}{2\omega}\right]+\psi_{\beta+4}\left(\frac{\partial\omega}{\partial x}\right)^2\left[\frac{1}{16\omega^2}[(\beta+1)(\beta+2)(\beta+3)(\beta+4)]^{1/2}\right]$$

$$+\psi_{\beta-4}\left(\frac{\partial\omega}{\partial x}\right)^2\left[\frac{1}{16\omega^2}[\beta(\beta-1)(\beta-2)(\beta-3)]^{1/2}\right]=0 \qquad (4.13)$$

where $k_\beta^2=\frac{2m}{\hbar^2}[\varepsilon_{TOT}-\varepsilon_\beta-V(x)]$.

Interestingly, a tapered parabolic confining potential results in scattering into modes $\beta\pm2$ and $\beta\pm4$. This scattering is governed principally by the parity of the states.

If the waveguide were homogeneous, then $\partial\omega/\partial x=0$ and $\partial^2\omega/\partial x^2=0$. The equation then reduces to the well-known uncoupled one-dimensional Schrödinger Equation

$$\frac{\partial^2\psi_\beta}{\partial x^2}+k_\beta^2\psi_\beta=0 \tag{4.14}$$

and has the solution given by Equation 4.6.

Locally, even when the waveguide is not homogeneous, the wavefunction may be expanded in terms of the local transverse eigenstates of the system

$$\Psi(x,y)=\sum_n \psi_n(x)\,\phi_n(y) \tag{4.15}$$

where $\psi_n(x)=c_n^+\exp(ik_nx)+c_n^-\exp(-ik_nx)$.

Extending this idea, Equation 4.3 can be expanded in terms of these local forward (c_n^+) and (c_n^-) backward travelling states.

To convert Equation 4.3 to local forward and backward states, the Villars-Fesbach transformation *(Fesbach 1958)* is used, that is

$$\psi_n^\pm=\frac{1}{2}\left[\psi_n\pm\frac{1}{ik_n}\frac{\partial\psi_n}{\partial x}\right] \tag{4.16}$$

When applied to $\psi_n(x)=c_n^+\exp(ik_nx)+c_n^-\exp(-ik_nx)$, this produces either the forward, ψ_n^+, or backward, ψ_n^-, travelling components. From Equation 4.16, the following further identities can be determined:

$$\frac{\partial\psi_n}{\partial x}=ik_n\left(\psi_n^+-\psi_n^-\right) \tag{4.17}$$

and $$\frac{\partial^2\psi_n}{\partial x^2}=ik_n\left[\pm2\frac{\partial\psi_n^\pm}{\partial x}\mp ik_n\left(\psi_n^+-\psi_n^-\right)+\frac{1}{k_n}\frac{\partial k_n}{\partial x}\left(\psi_\beta^+-\psi_\beta^-\right)\right]. \tag{4.18}$$

Using these relationships (Equations 4.17 and 4.18), Equation 4.3 can be rewritten as a system of coupled first order linear differential equations in terms of the local forward and backward travelling components of each mode.

$$\frac{\partial \psi_\beta^+}{\partial x} = ik_\beta \psi_\beta^+ + \sum_n M_{\beta n}^{++} \psi_n^+ + \sum_n M_{\beta n}^{+-} \psi_n^- \tag{4.19}$$

$$\frac{\partial \psi_\beta^-}{\partial x} = -ik_\beta \psi_\beta^- + \sum_n M_{\beta n}^{-+} \psi_n^+ + \sum_n M_{\beta n}^{--} \psi_n^- \tag{4.20}$$

where $M_{\beta n}^{\pm\pm}$ are the intermode coupling terms detailed in Appendix 1.

If we define ${}^kM_{\beta\beta}^{++} = M_\beta^{++} + ik_\beta$ and ${}^kM_{\beta\beta}^{--} = M_\beta^{--} - ik_\beta$, the coupled equations can be rewritten as

$$\frac{\partial}{\partial x}\begin{bmatrix} \psi_1^+ \\ \psi_2^+ \\ \vdots \\ \psi_n^+ \\ \psi_1^- \\ \psi_2^- \\ \vdots \\ \psi_n^- \end{bmatrix} = \begin{bmatrix} {}^kM^{++} & M^{+-} \\ M^{-+} & {}^kM^{--} \end{bmatrix} \begin{bmatrix} \psi_1^+ \\ \psi_2^+ \\ \vdots \\ \psi_n^+ \\ \psi_1^- \\ \psi_2^- \\ \vdots \\ \psi_n^- \end{bmatrix} \tag{4.21}$$

In order to find the general solution for the waveguide, it is necessary to integrate these 2n coupled equations across the system. Since only the net current is of interest, it is only necessary to consider the potential difference, δV, between the contacts.

This leads to a separation in the known boundary conditions of the system shown in Figure 4.2. All input modes are assumed to be fully occupied at the entrance of the waveguide and, because only net current is considered, all of the backward travelling states at the end of the system are assumed to be empty.

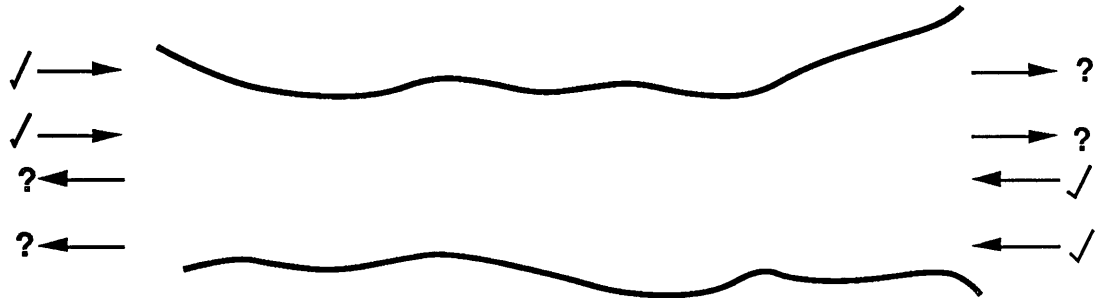

Figure 4.2 All inputs of the electron waveguide are known

This type of problem is known as a two point boundary value problem (2BVP), referring to the separation in the known boundary conditions between the two ends of the system. To find a complete solution, it is necessary to find the unknown boundary conditions at either end of the system. These must be consistent with the known boundary conditions and the system equations.

As a consequence of this problem being common to many areas of applied mathematics, physics and engineering, many approaches have been developed to solve the 2BVP *(Roberts 1972)*. The choice of approach and its development evolved as various techniques were tried, and their limitations in the context of the electron waveguide problem discovered. Of particular importance in this process were the problems of modal cutoff and numerical stability. These were finally solved within the framework of the method of complementary functions.

4.3 The Method of Complementary Functions (CF)

If a full set of boundary conditions were known at either boundary of the system, the solution for the entire system could be obtained by integrating this known complete boundary condition across the system. Unfortunately, a complete boundary condition is not available. The known boundary conditions are separated between the two ends of the system and so the missing boundary conditions must be found.

Of the techniques used to solve this 2BVP, many are termed 'shooting' methods. This refers to a multi-pass approach, in which the missing boundary conditions are estimated and the system of equations integrated. The discrepancy between the known boundary conditions at the end of the system and those calculated are then used to improve the initial estimates of the unknown boundary conditions. This process is then repeated until a satisfactory solution is obtained. Unfortunately, in the electron waveguide system, small changes in the the initial conditions can, due to the exponential nature of cut-off evanescent modes, lead to large changes in the solution. Such problems are termed 'sensitive' and prove very difficult to solve by techniques which attempt to converge on a solution. Instead, the method of complementary functions (CF) was used, since it determines the unknown boundary conditions in one pass through the system.

From the theory of linear differential equations it is known that, barring numerical inaccuracy, solutions which are linearly independent at some initial point remain orthogonal for all values of the independent variable for which a solution exists *(Roberts 1972)*. This property forms the basis of the CF method, which expands the solution in terms of orthogonal vectors. These vectors evolve through the system but their expansion coefficients remain constant. Therefore, once a set of independent vectors of a system have been determined, any boundary configuration may be solved by expanding the required boundary condition in terms of these known orthogonal functions. This latter point is very useful and leads to a considerable saving in computer time over other methods, which must compute the entire solution for every configuration of known boundary conditions.

Consider the 2n coupled equations, partitioned so that the boundary conditions of the vector **A** are more easily assigned

$$\frac{\partial \mathbf{A}}{\partial x} = \mathbf{M}(x)\,\mathbf{A}(x) \tag{4.22}$$

where **A**(x) = 2n vector of components $\left(A_1^+(x)A_2^+(x)\ldots A_n^+(x)A_1^-(x)A_2^-(x)\ldots A_n^-\right)^T$, **M** is a $2n \times 2n$ coupling matrix and the known boundary conditions are

$A_i\,(x_{start}) = \Pi start_i$ for i = 1, 2,...., n

$A_m\,(x_{end}) = \Pi end_m$ for m = n+1, n+2,..., 2n

The general solution of this linear system may be represented as

$$A(x) = \sum_{k=1}^{2n} b_k A^k(x) \qquad x_{start} \le x \le x_{end} \tag{4.23}$$

where $A^k(x)$ is the k^{th} independent vector with components $\left(A_1^k(x) A_2^k(x) \ldots A_{2n}^k(x)\right)$ and b_k are the expansion coefficients, which are related to the known boundary conditions via

$$\sum_{k=1}^{2n} b_k A_i^k(x_{start}) = \Pi start_i \quad i = 1,n \tag{4.24a}$$

and

$$\sum_{k=1}^{2n} b_k A_m^k(x_{end}) = \Pi end_m \quad m = n+1,2n \tag{4.24b}$$

This represents a system of 2n equations in the 2n unknown variables b_k. If the independent vectors at the start of the system are defined by $A_j^k(x_{start}) = \delta_{kj}$, then $b_i = \Pi start_i$ for i = 1,2,...,n and Equation 4.24 reduces to

$$\sum_{k=n+1}^{2n} b_k A_m^k(x_{end}) = \Pi end_m - \sum_{k=1}^{n} \Pi start_k A_m^k(x_{end}) \qquad m = n+1, 2n \tag{4.25}$$

The system of equations has been halved and, providing that it is possible to integrate the independent vectors, the determination of the boundary conditions is a straightforward process. Once the independent vectors have been propagated through the system, any change of boundary conditions simply requires the recalculation of the expansion coefficients, b_k, in Equation 4.25. This results in a considerable saving of computational time.

4.4 Integration of the Coupled Mode Equations

If the waveguide were straight and homogeneous, then all intermode coupling would disappear, so that $\partial\omega/\partial w = 0$ and $\partial^2\omega/\partial x^2 = 0$, and the system would revert back to that of n uncoupled one–dimensional problems. Unfortunately, on the introduction of intermode coupling, analytical solutions are difficult to find, and the system of 2n coupled first order differential equations must be integrated numerically.

4.4.1 Integration Through Cut-off

Unlike other waveguide systems, the electron waveguide does not support leaky or radiation modes, since the confining potential is very much larger than the electron energy. Consequently, it becomes necessary to integrate accurately through the modal cutoff regions of the device. As mode β passes through cutoff, then $k_\beta = 0$ and the coupling matrix in $\psi_\beta^\pm$ space (Appendix 1) becomes singular. This singularity at cut-off is analogous to the turning point problem in the one–dimensional WKBJ problem, as the modal field can no longer be adequately described in the $\psi_\beta^\pm$ space.

Transforming from the $\psi_\beta^\pm$ space to a new Ψ_β, Ω_β space, where $\Omega_\beta = \partial\psi_\beta/\partial x$, as shown in Appendix 2, removes the singularity at cut-off, at the expense of moving to a less physical space. In the Ψ_β, Ω_β space the coupled equations are transformed to

$$\frac{\partial}{\partial x}\begin{bmatrix} \psi_1 \\ \psi_2 \\ \vdots \\ \psi_n \\ \Omega_1 \\ \Omega_2 \\ \vdots \\ \Omega_n \end{bmatrix} = \begin{bmatrix} \mathbf{T}^{\psi\psi} & \mathbf{T}^{\psi\Omega} \\ \mathbf{T}^{\Omega\psi} & \mathbf{T}^{\Omega\Omega} \end{bmatrix} \begin{bmatrix} \psi_1 \\ \psi_2 \\ \vdots \\ \psi_n \\ \Omega_1 \\ \Omega_2 \\ \vdots \\ \Omega_n \end{bmatrix} \tag{4.26}$$

where the coupling matrix $\mathbf{T}$ is represented by four $n \times n$ sub-matrices. $\mathbf{T}^{\Psi\Psi} = 0$, $\mathbf{T}^{\Psi\Omega} = \mathbf{I}$, the identity matrix, and the sub-matrices $\mathbf{T}^{\Omega\Psi}$ and $\mathbf{T}^{\Omega\Omega}$ are given in Appendix 2.

The success of this transformation can be understood by examining an uncoupled system. In the space of ψ_β and Ω_β each modal equation becomes

$$\frac{\partial}{\partial x}\begin{bmatrix} \psi_\beta \\ \Omega_\beta \end{bmatrix} = \begin{bmatrix} 0 & 1 \\ k_\beta^2 & 0 \end{bmatrix} \begin{bmatrix} \psi_\beta \\ \Omega_\beta \end{bmatrix} \tag{4.27}$$

which is well behaved through cutoff. When k_β^2 is linear in x, this is equivalent to Stokes's equation

$$\frac{\partial^2\psi_\beta}{\partial x^2} - Cx\psi_\beta = 0 \tag{4.28}$$

The solutions of this equation (Eqn 4.28) are well documented, and are used to determine the connecting formulas in the WKBJ approximation. For the system of 2n coupled equations, it is neither practical nor necessary to employ these connecting formulae, as the numerical integration follows the correct solution in the analytically continuous ψ_β, Ω_β space.

4.4.2 Numerical Instability of Integration

Simple integration of the coupled equations, using Runge-Kutta or any other integration procedure, can lead to a divergence of the solution. This divergence results from the presence of two very different growth classes of solution and, when one or more modes are cut off, it is not always possible to track the growing and decaying factors in the finite word length range of a computer *(Evans 1986)*. For example, consider

$$y(x) = C\exp(-20x) + B\exp(+20x) \tag{4.29}$$

Often the physical solution is the decaying exponential but, unfortunately, any rounding or truncation error is equivalent to the introduction of a small amount of the unwanted solution

$$y(x) = D\exp(-20x) + \delta\exp(+20x) \tag{4.30}$$

Eventually, even if δ is very small, the increasing exponential will dominate the solution, and will lead to a loss of orthogonality between the initially independent vectors of the CF method. Such a problem has been termed an *exponential dichotomy (Mattheij 1985)*.

It was shown in Section 4.2 that the equations of a straight, homogeneous waveguide decouple into n one-dimensional independent systems. These one-dimensional problems are well known in quantum mechanics *(Schiff 1968)*. In such systems it is often possible to avoid numerical problems, when flux tunnels through a wide barrier, by integrating the two growth classes of the solution in their respective decaying direction. This ensures that all terms are of the same magnitude. Unfortunately, this is not possible with this system of equations, because the intermode coupling leads to a dependence of each mode on *both* growth classes.

4.4.3 A Stable Integration Procedure

The first stage in determining a stable integration procedure is to discretize the problem by dividing the channel into sections of length Δx. Then it is necessary to determine a wave propagator $\mathbf{Q}_j$ for each section, j, of the channel. This wave propagator is defined to propagate a known wavefunction from the start of section j-1 to the start of section j. It therefore comprises of two distinct elements:

i) the propagation solution across the section j-1, defined by the operator $\mathbf{P}_j$
ii) the interface function, $\mathbf{R}_j$, that carries the solution across the interface into the start of the next section, whilst maintaining the continuity of the wavefunction and its first derivative.

The propagation element, $\mathbf{P}_j$, is determined by numerically integrating, using fourth order Runge-Kutta, a system of 2n independent solutions. This determines the propagator for the section in an identical manner to the method of complementary functions described in Section 4.3. Accuracy is maintained by ensuring that Δx is sufficiently small to allow stable and accurate numerical integration.

A trivial example would be the propagator of a forward propagating plane wave state in a uniform guide. Using the standard independent vectors $\begin{bmatrix} 1 \\ 0 \end{bmatrix}$ and $\begin{bmatrix} 0 \\ 1 \end{bmatrix}$ for the two terms ψ and $\partial\psi/\partial x$ produces a propagation matrix

$$\begin{bmatrix} \exp(ik\Delta x) & 0 \\ 0 & \exp(ik\Delta x) \end{bmatrix} \tag{4.31}$$

which would propagate the vector $\begin{bmatrix} \psi_{j-1}^s & \dfrac{\partial \psi_{j-1}^s}{\partial x} \end{bmatrix}^T$ across the the section j-1

$$\begin{bmatrix} \psi_{j-1}^e \\ \dfrac{\partial \psi_{j-1}^e}{\partial x} \end{bmatrix} = \begin{bmatrix} \exp(ik\Delta x) & 0 \\ 0 & \exp(ik\Delta x) \end{bmatrix} \begin{bmatrix} \psi_{j-1}^s \\ \dfrac{\partial \psi_{j-1}^s}{\partial x} \end{bmatrix} \tag{4.32}$$

where ψ_{j-1}^s and ψ_{j-1}^e is the wavefunction at the start and end of section j-1 respectively.

Obviously, where more than one mode is included in the calculation and where there is intermode coupling, this propagator is more complex. It is, however, still obtained in an identical manner, by numerically integrating 2n independent vectors across the system.

The interface element of the propagator, $\mathbf{R}_j$, ensures that there is continuity of the wavefunction and its first derivative over the boundary of connected sections. Expanding the wavefunction and first derivative of the wavefunction on either side of the boundary gives

$$\psi_1^e(x)\phi_1^e(y) + \psi_2^e(x)\phi_2^e(y) + \ldots \psi_n^e(x)\phi_n^e(y) = \psi_1^s(x)\phi_1^s(y) + \psi_2^s(x)\phi_2^s(y) + \ldots \psi_n^s(x)\phi_n^s(y) \tag{4.33}$$

$$\Omega_1^e(x)\phi_1^e(y) + \Omega_2^e(x)\phi_2^e(y) + \ldots \Omega_n^e(x)\phi_n^e(y) = \Omega_1^s(x)\phi_1^s(y) + \Omega_2^s(x)\phi_2^s(y) + \ldots \Omega_n^s(x)\phi_n^s(y) \tag{4.34}$$

where the subscript for the section number has been dropped for clarity but (*e*) signifies the end of a section and (*s*) signifies the start of the next section. The wavefunctions and derivatives at the start of the section are obtained by applying the projection integrals

$$\int_{-\infty}^{\infty} \phi_n^s(y)\, dy \tag{4.35}$$

to the wavefunction at the end of the preceding section. This produces an interface matching matrix of the form

$$\begin{bmatrix} \psi_1^s \\ \Omega_1^s \\ \psi_2^s \\ \Omega_2^s \\ . \\ . \\ \psi_n^s \\ \Omega_n^s \end{bmatrix} = \begin{bmatrix} \langle\phi_1^e|\phi_1^s\rangle & 0 & \langle\phi_2^e|\phi_1^s\rangle & 0 & . & . \\ 0 & \langle\phi_1^e|\phi_1^s\rangle & 0 & \langle\phi_2^e|\phi_1^s\rangle & . & . \\ \langle\phi_1^e|\phi_2^s\rangle & 0 & \langle\phi_2^e|\phi_2^s\rangle & 0 & . & . \\ 0 & \langle\phi_1^e|\phi_2^s\rangle & 0 & \langle\phi_2^e|\phi_2^s\rangle & . & . \\ . & . & . & . & . & . \\ . & . & . & . & . & . \\ \langle\phi_1^e|\phi_n^s\rangle & 0 & \langle\phi_2^e|\phi_n^s\rangle & 0 & . & . \\ 0 & \langle\phi_1^e|\phi_n^s\rangle & 0 & \langle\phi_2^e|\phi_n^s\rangle & . & . \end{bmatrix} \begin{bmatrix} \psi_1^e \\ \Omega_1^e \\ \psi_2^e \\ \Omega_2^e \\ . \\ . \\ \psi_n^e \\ \Omega_n^e \end{bmatrix} \tag{4.36}$$

In the case of a channel which can be described by an analytical function, there is no discontinuity between the adjacent sections, and therefore this interface matrix reduces to the identity matrix. In cases where there is a discontinuity between adjacent sections, as described in Section 4.6, it is generally necessary to determine this overlap matrix numerically.

The full wave propagator $\mathbf{Q_j}$ is therefore given by

$$\mathbf{Q}_j = \mathbf{R}_j \mathbf{P}_j \tag{4.37}$$

$$\text{and } \mathbf{v}_j = \mathbf{Q}_j \mathbf{v}_{j-1} \tag{4.38}$$

Equation (4.38) describes the propagation of a wavefunction represented by a vector $\mathbf{v}_{j-1}$ at the start of section j-1 to the start of section j. Unfortunately, the application of this equation to propagate a wavefunction through the entire system would still result in the numerical problems already discussed in Section 4.4.2.

However, Mattheij *(Mattheij 1985)* has developed a stable method of applying this propagation operator in Ψ^+ and Ψ^- space. In order to use this method, it is therefore necessary to transform Equation 4.38 to Ψ^+ and Ψ^- space. Again the transformation given in Equation 4.17 is used, such that the matrix X_j transforms from $\Psi\Omega$ to $\Psi^+\Psi^-$ space. Then

$$\begin{bmatrix} \psi_1^- \\ \psi_2^- \\ . \\ \psi_n^- \\ \psi_1^+ \\ \psi_2^+ \\ . \\ \psi_n^+ \end{bmatrix} = \mathbf{X}_j \begin{bmatrix} \psi_1 \\ \Omega_1 \\ \psi_2 \\ \Omega_2 \\ . \\ . \\ \psi_n \\ \Omega_n \end{bmatrix} \tag{4.39}$$

$$\mathbf{V}'_j = \mathbf{X}_j \mathbf{V}_j$$

$$\text{Then } \mathbf{V}'_j = \mathbf{Q}'_j \mathbf{V}'_{j-1} \tag{4.40}$$

Equation 4.40 describes the propagation of a matrix $\mathbf{V}'_{j-1}$ of 2n wavefunctions in the ψ^+ and ψ^- space over the same section from the start of section j-1 to the start of section j, where $\mathbf{Q}'_j = \mathbf{X}_j \mathbf{R}_j \mathbf{P}_j \mathbf{X}^{-1}_{j-1}$.

Following Evans *(Evans 1987)*, who has applied this approach to the study of seismic waves, it is possible to integrate these equations in a stable manner. The main idea is to replace Equation 4.40 with a triangular recursion, in which the two growth classes of the solution are partially decoupled.

First a transformation is defined as

$$\mathbf{V}'_j = \mathbf{T}_j \mathbf{W}_j \tag{4.41}$$

where $\mathbf{T}_0$ is equal to the identity matrix and $\mathbf{T}_j$ is found from the modified Gram-Schmidt orthogonalization of the columns of $\mathbf{Q}'_j \mathbf{T}_{j-1}$ for $j = 1, ..., N+1$, that is

$$\mathbf{Q}'_j \mathbf{T}_{j-1} = \mathbf{T}_j \mathbf{U}_j \tag{4.42}$$

where $\mathbf{T}_j$ is unitary and $\mathbf{U}_j$ is upper triangular. Substituting Equations 4.41 and 4.42 into Equation 4.40 produces a triangular recursion

$$\mathbf{W}_j = \mathbf{U}_j \mathbf{W}_{j-1} \tag{4.43}$$

for the new unknown matrix $\mathbf{W}_j$. Since $\mathbf{U}_j$ is upper triangular there is a partial decoupling in the propagation of the elements of $\mathbf{W}$.

This can be seen by partitioning $\mathbf{U}$ and $\mathbf{W}$, so that

$$\mathbf{U}_j = \begin{bmatrix} \mathbf{B}_j & \mathbf{C}_j \\ 0 & \mathbf{E}_j \end{bmatrix} \text{ and } \mathbf{W}_j = \begin{bmatrix} \mathbf{W}_{BB,j} & \mathbf{W}_{BF,j} \\ \mathbf{W}_{FB,j} & \mathbf{W}_{FF,j} \end{bmatrix}. \tag{4.44}$$

Therefore

$$\mathbf{W}_{BB,j} = \mathbf{B}_j \mathbf{W}_{BB,j-1} + \mathbf{C}_j \mathbf{W}_{FB,j-1} \tag{4.45}$$

$$\mathbf{W}_{BF,j} = \mathbf{B}_j \mathbf{W}_{BF,j-1} + \mathbf{C}_j \mathbf{W}_{FF,j-1} \tag{4.46}$$

$$\mathbf{W}_{FB,j} = \mathbf{E}_j \mathbf{W}_{FB,j-1} \tag{4.47}$$

$$\mathbf{W}_{FF,j} = \mathbf{E}_j \mathbf{W}_{FF,j-1} \tag{4.48}$$

These new variables, $\mathbf{W}$, are not physical, but provide an unusual representation of $\mathbf{W}_{FF}$ propagating forward along the channel. The wavefunction in this space is only reflected, once it has reached the end of the channel, through $\mathbf{W}_{BF}$ propagating back along the channel.

Mattheij *(Mattheij 1985)* has proved that $\mathbf{W}_{FF}$ is numerically stable for increasing j, and that $\mathbf{W}_{BB}$ is numerically stable for decreasing j, as is $\mathbf{W}_{BF}$. To obtain a general solution for the entire system, the method of Complementary Functions is again used. First, n independent vectors, defined by $\mathbf{W}_{FB,0} = 0$ and $\mathbf{W}_{FF,0} = \mathbf{I}$, are propagated forward through the system. Then a further n independent vectors, defined by $\mathbf{W}_{BF,N+1} = 0$ and $\mathbf{W}_{BB,N+1} = \mathbf{I}$, are propagated back up through the system, completing the system of 2n independent vectors.

4.5 Numerical Results

The stable integration procedure described in Section 4.4.3 was applied to the method of Complementary Functions and used to calculate solutions to the analytical systems of coupled mode equations (Equation 4.8). The complete computational procedure was as follows:

i) Define the analytical functions to represent the required structure.

ii) Divide the structure into suitably sized sections, Δx, and determine the wave propagator in each section (by integrating in ψ, Ω space and then transforming to ψ^+, ψ^- space).

iii) Decouple the propagator matrices $\mathbf{Q}'_j$ using the approach developed by Mattheij to integrate the 2n independent vectors across the system.

iv) Calculate the expansion coefficients consistent with the known boundary conditions and the 2n independent vectors to determine the wavefunction and flux throughout the entire system.

The stability of the approach was tested on various structures, paying particular attention to the current conservation. It was found that current conservation was adequate, with an error of the order of 1 part in 10^5, when the wavefunction was expanded in terms of ten local normal modes.

To illustrate the stability of this approach, the probability density of an electron in the lowest mode passing through a parabolic tapered electron waveguide of length 0.3 μm is shown in Figure 4.3. The electron wavefunction passes through cut-off at 0.2 μm and, after tunnelling, is completely reflected. Ten modes were maintained throughout so that, even in the region where the mode is propagating, the calculation is carrying nine potentially unstable modes. The step in the plot represents the 8 meV contour of the parabolic confining potential. The stepped nature of the taper is an artifact of the plotting routine.

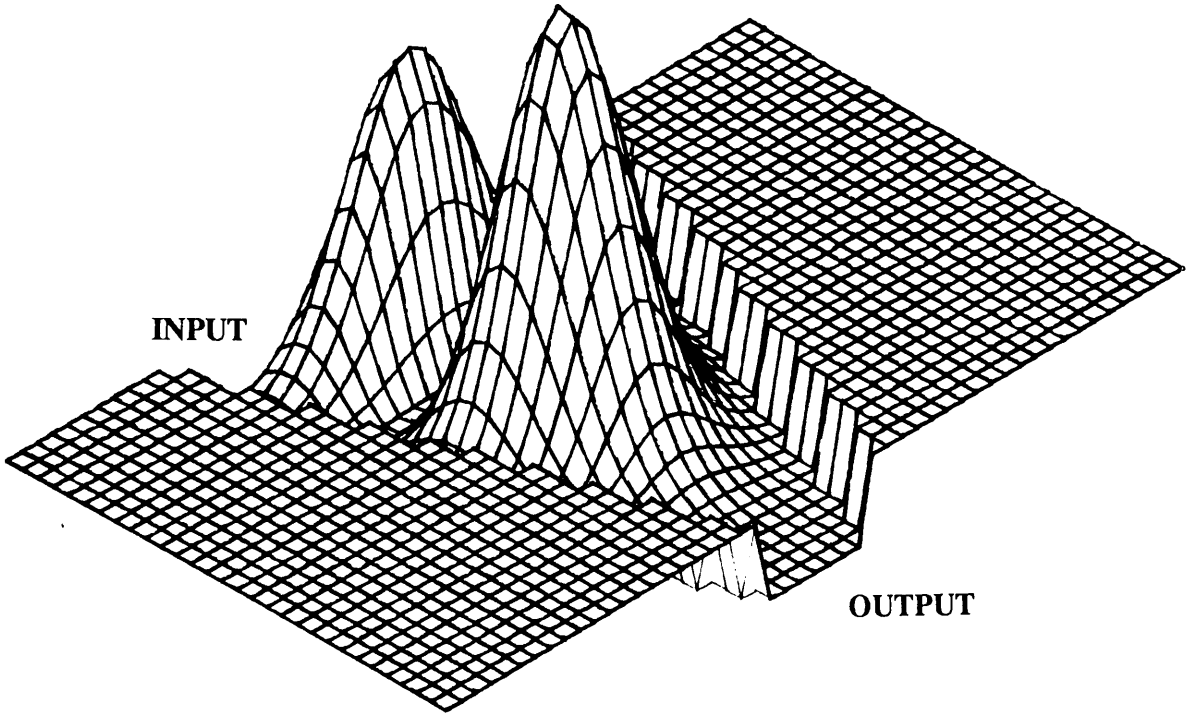

Figure 4.3 Electron wavefunction (2 meV) in lowest mode passing through a tapered section of waveguide. The channel taper is 0.3 μm long and the 2 meV wavefunction cuts off at 0.2 μm.

Another example is illustrated in Figure 4.4. This shows the transmission coefficient of an electron, incident in the lowest mode, going through a circular cavity in the guide. As can be seen from the transmission, the cavity passes through various resonances as the energy of the electron wavefunction is varied.

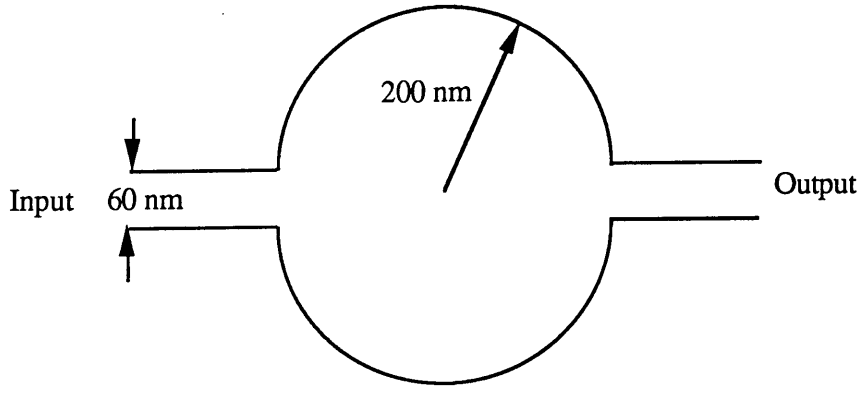

Figure 4.4a Schematic of cavity with transmission coefficient shown in Figure 4.4b. The outline represents the 30 meV contour of the parabolic confining potential.

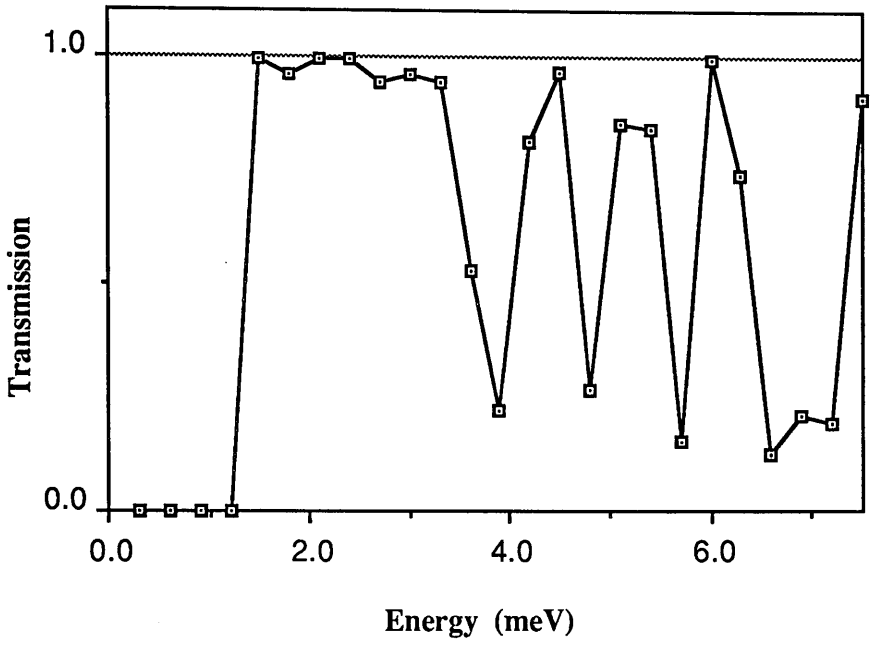

Figure 4.4b The calculated transmission coefficient of an electron input in the lowest mode

4.6 Non-analytic Structures

In the previous section, results were shown for structures in which the potential profile of the guide could be described by analytical functions. The intermode coupling could therefore also be described by closed analytical functions.

However, in subsequent chapters it will not always be possible to describe the potential profile by analytical functions. In such structures it will be necessary to discretize the problem. In each small section the waveguide will, however, be assumed to be homogeneous. At the interfaces, where the waveguide is discontinuous, the interface matrix $\mathbf{R}_j$ will no longer be equivalent to the identity matrix, but must be determined numerically. Figure 4.5 shows a schematic of such a discretization. The dashed lines indicate interfaces where the overlap matrix will lead to intermode scattering.

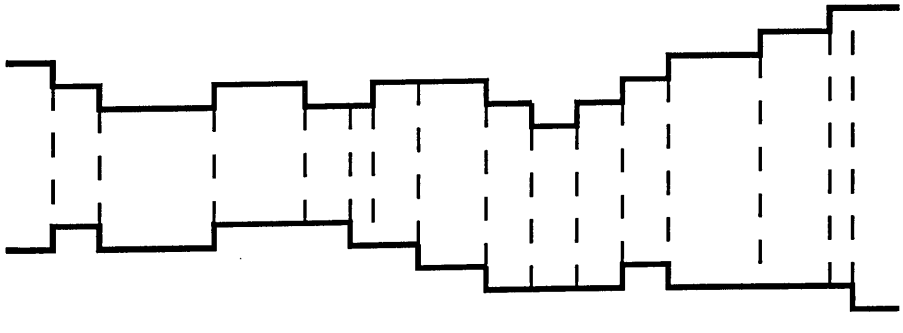

Figure 4.5 Schematic of the approach used in the discretization of the non-analytic electron waveguide potential

4.7 Summary

This chapter began with the analytical development of a system of coupled equations for an electron waveguide defined by a parabolic potential. This was made possible by exploiting several of the known characteristics of the Hermite polynomial eigenfunctions of the parabolic potential. The coupled mode equations explicitly showed that any deviation from a homogeneous waveguide would result in scattering into modes $\beta \pm 2$ and $\beta \pm 4$. Unfortunately it was necessary to develop a numerical method to solve this system of equations.

The numerical method applied to the solution of the coupled equations was based on the method of Complementary Functions (CF). It was however necessary to extend the basic CF method to take account of the problems of singularities at modal cut-off and general numerical stability. By careful choice of the space in which the coupled equations are integrated, and by adoption of the decoupling transformation developed by Mattheij, a numerically stable and efficient method to solve the coupled mode equations was successfully developed.

Chapter Five
The Ideal Quantum Point Contact

5.1 Introduction

The beauty of the quantum point contact is its apparent geometric simplicity. After the sophisticated MBE process to produce a 2DEG, the QPC is formed by confining a section of this two-dimensional system into a narrow constriction, usually by means of the electrostatic squeezed gate technique (refer to Chapter 2). In this and all subsequent chapters, the discussion will be restricted to squeezed gate samples. Since the width of the constriction is comparable to the Fermi wavelength, the electrons in the channel enter the transverse quantized states across the channel, whilst maintaining their freedom in the axial direction.

In this chapter, the electron transport through this ballistic device is studied. The basic geometry of the ideal QPC has a uniform channel and consequently no intermode scattering. The system can therefore be modelled by applying the well-known methods of one-dimensional quantum mechanics to each mode independently. However, as the model becomes more realistic, a point is reached where the electrons begin to explore beyond the confines of a purely one-dimensional system and therefore an alternative technique must be used. In this work a modal analysis is employed based on the Coupled Mode method developed in Chapter Four. As will become evident, such an approach is very versatile and has provided a detailed study of the electron transport characteristics in ballistic structures for the first time.

5.2 The Original Experiments

In the original experiments of Wharam *et al (Wharam 1988)* and van Wees *et al (van Wees 1988),* the analysis of the quantized resistance was based on a system of purely one-dimensional channels with no intermode coupling. The net current due to one particular 1D transverse quantized sub-band or mode, I, assuming that it is fully occupied, is given by

$$I = e \times v(E_f) \times \frac{1}{2} n_{1d}(E_f) \times eV \tag{5.1}$$

where $v(E_f)$ is the electron velocity at the Fermi energy E_f, n_{1d} is the one-dimensional density of states and V is the potential difference across the QPC. The factor of 1/2 is necessary, since only the electrons which are propagating in the forward direction contribute to the flux.

The one-dimensional density of states, including spin, is given by

$$n_{1d}(E_f) = \frac{2}{\pi \hbar v(E_f)} \tag{5.2}$$

Substituting this into Equation 5.1 leads to a cancellation of the energy-dependent velocity to give

$$I = \frac{e^2 V}{\pi \hbar} \tag{5.3}$$

and, as $G = \frac{I}{V}$, (5.4)

$$G = \frac{2e^2}{h} \tag{5.5}$$

If it is assumed that each of the conducting modes acts independently in the constriction, then

$$G = \sum_{1}^{m} \frac{2e^2}{h} \tag{5.6}$$

where m is the upper limit on the number of occupied modes, such that the transverse energy of the m^{th} mode must be less than the Fermi energy.

With such an elegant analysis producing the desired result, it is perhaps surprising to learn that very many samples do not produce quantized resistance. Even when samples are made in an apparently identical manner, often alongside each other on the same substrate, it is impossible to determine in advance which samples will produce a quantized resistance *(Williamson 1990)*.

5.3 The Uniform Model With 2DEG Contacts.

In the simplest model of a QPC, the channel seen by the electrons is assumed to be identical to that of the gap between the gate electrodes on the surface of the sample. The assumption that the walls of the channel are smooth and parallel leads to a complete decoupling between the different quantized transverse modes of the channel. Therefore, within the single particle approximation, each occupied mode of the system propagates independently of electrons in all other modes in the channel. This is a considerable simplification, which has already been shown in Section 5.2 to be able to be solved analytically. This analysis produces perfect quantized resistance, with the implicit assumption that the QPC is connected to the contacts by ideal leads.

So far, no attempt has been made to incorporate the 2DEG contact regions into the model. It has so far been assumed that all the available modes in the channel are filled with electrons from the 2DEG contacts. However, unlike many macroscopic systems in which the exact nature of the electrical contact regions are unimportant, the contacts to the electron channel form an integral part of the system *(Landauer 1989b)*.

The contact region is much wider than the channel and is approximated as an infinite 2DEG in which the electron wavefunction is $\psi_{2D}(\mathbf{r}) = \exp(i\mathbf{K}.\mathbf{r})$, where $|K| = \sqrt{\kappa^2 + \gamma^2}$, κ is the component of the wavevector in the axial direction of the QPC and γ is the perpendicular wavevector component. In the channel the wavefunction is approximated by a composition of n modes. As in Chapter Four, these n modes are separated into the forward and backward travelling components. The flux inside the channel is expanded as

$$\Psi(x,y) = \sum_n \left\{ c_n^+ \exp(ik_n x) + c_n^- \exp(-ik_n x) \right\} \phi_n(y) \qquad (5.7)$$

where $c_n^{\pm}$ is the amplitude of the electrons travelling forward (+) or backwards (–) in the n^{th} mode.

The propagation constant is given by

$$k_n = \sqrt{2m(\varepsilon_{tot} - \varepsilon_n)/\hbar^2} \tag{5.8}$$

where ε_{tot} is the total energy and ε_n is the energy of the n^{th} transverse eigenstate. The propagation constant may be real or imaginary, corresponding to propagating or evanescent modes.

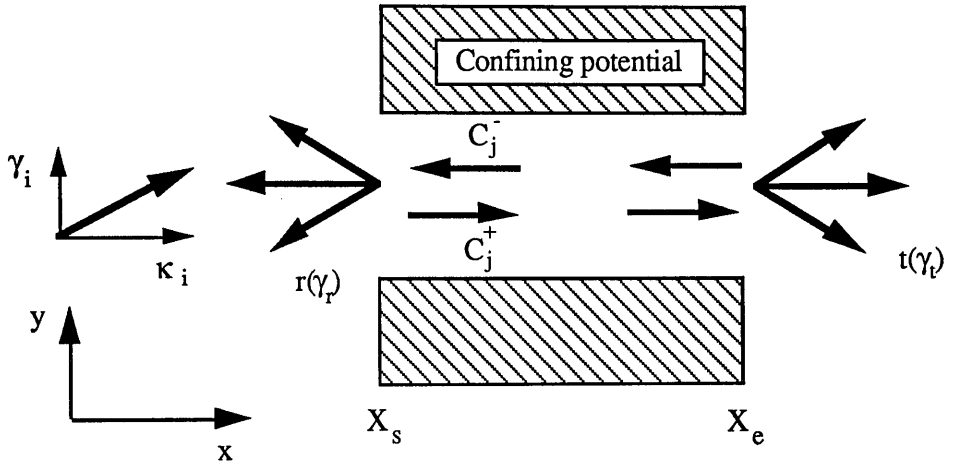

Figure 5.1 Schematic of the QPC connected to 2DEG contacts

In order to simplify the equations, the matrix **E** is defined. This matrix is made up of 2n independent column vectors. Each column vector is formed from the forward and backward components of the n modes in the system. For a uniform QPC, the independent vectors are represented by a simple plane wave component in each mode at the start of the channel. By the end of the channel, at x_e, these independent column vectors will each have propagated independently, since there is no intermode coupling in a uniform channel. If **E** at the start of the channel is represented by $\mathbf{E}_{xs}$, where

$$\mathbf{E}_{xs} = \begin{bmatrix} \exp(ik_1x_s) & 0 & & & & \\ 0 & \exp(-ik_1x_s) & 0 & & & \\ & 0 & \exp(ik_2x_s) & . & & \\ & & 0 & . & 0 & \\ & & & . & \exp(ik_nx_s) & 0 \\ & & & & 0 & \exp(-ik_nx_s) \end{bmatrix} \tag{5.9}$$

Then the matrix has the form $\mathbf{E}_{xe}$ at the end of the channel, where

$$\mathbf{E}_{xe}=\begin{bmatrix} \exp(ik_1x_e) & 0 & & & & & \\ 0 & \exp(-ik_1x_e) & 0 & & & & \\ & 0 & \exp(ik_2x_e) & . & & & \\ & & 0 & . & 0 & & \\ & & & . & \exp(ik_nx_e) & 0 & \\ & & & & 0 & \exp(-ik_nx_e) & \end{bmatrix} \tag{5.10}$$

However, for more complex systems in which the channel is not uniform and where is inter-mode coupling, these independent vectors become more complex as they progress through the channel. They must be found numerically throughout the system using the method in Chapter Four.

The transverse components of these independent vectors are equal to the local transverse eigenstates of the guide. These transverse components are defined by the column vector $\Phi_{xs}(j)$, in which the first n elements are the first n transverse eigenstates of the system $\phi_1(y)$, $\phi_1(y)$, $\phi_2(y)$, $\phi_2(y)$ etc. These are then repeated for the second part of the vector, which corresponds to the backward travelling components in each mode.

The usual continuity conditions of the wavefunction and its first derivative at the discontinuities are applied at the two interfaces of the channel with the 2DEG contacts for each of the 2n modes in the channel. The necessary continuity of the wavefunction at this interface implies that the sum of the incident and reflected wavefunction in the contact must equal the transmitted wavefunction in the waveguide. Applying this continuity of wavefunction to the interface between the left hand 2DEG contact and the start of the channel leads to the equation

$$\frac{1}{\sqrt{2\pi}}\exp(i\gamma_i y)\exp(i\kappa_i x_s)+\frac{1}{\sqrt{2\pi}}\int_{-\infty}^{+\infty} r(\gamma_r)\exp(i\gamma_r y)\exp(i\kappa_r x_s)\,d\gamma_r$$
$$=\sum_{j}^{2n}\sum_{l}^{2n} c_j\Phi_{xs}(l)\,E_{x_s}(l,j) \tag{5.11}$$

For the case of a homogeneous channel, the terms c_{2j-1} and c_{2j} for $j \geq 1$ correspond respectively to the amplitude of the forward (c_j^+)and backward (c_j^-) travelling flux in each mode throughout the channel. The term $r(\gamma_r)$ is equal to the amplitude of the reflected flux of the plane wave, $\exp(i\gamma_r y)\exp(i\kappa_r x_s)/\sqrt{2\pi}$. This results from the incidence of the plane wave $\exp(i\gamma_i y)\exp(i\kappa_i x_s)/\sqrt{2\pi}$ on the QPC from the contact. The term κ_r is defined by

$$\kappa_r=\sqrt{\left((2m\varepsilon_{tot}/\hbar^2)-\gamma_r^2\right)}.$$

Using the orthogonality of the wavefunction at x_S, it is possible to simplify Equation 5.11 by applying the projection operator

$$\frac{1}{\sqrt{2\pi}} \int_{-\infty}^{\infty} \exp\ (-i\,\gamma_r y)\ dy$$

The equation then becomes

$$\delta_{\gamma_i\gamma_r}\exp(i\kappa_i x_s) + r(\gamma_r)\exp(-i\kappa_r x_s) = \sum_{j}^{2n}\sum_{l}^{2n} c_j M_{xs}(-\gamma_r,l)\, E_{xs}(l,j) \tag{5.12}$$

where $M_{xs}(-\gamma_r,l) = \frac{1}{\sqrt{2\pi}}\int_{-\infty}^{\infty} \exp(-i\gamma_r y)\,\phi_l(x_s y)\,dy.$

Next, the first derivative of the wavefunction at x_S is matched at the interface between the left hand 2DEG contact and the QPC channel, this time using the projection operator

$$\int_{-\infty}^{\infty} \phi_n(y)\,dy$$

This gives

$$\kappa_i\exp(i\kappa_i x_s)M_{xs}(\kappa_i,n) - \int_{-\infty}^{\infty} r(\gamma_r)\kappa_r M_{xs}(\gamma_r,n_c)\exp(-i\kappa_r x_s)d\gamma_r =$$

$$\sum_{j}^{2n}\sum_{p}^{2n} c_j Q(n,p) E_{xs}(p,j) \tag{5.13}$$

where the operator $\mathbf{Q}(n_c,p)$ produces the derivative of the wavefunction via the Villars-Fesbach transformation

$$\frac{\partial\psi_\beta(x)}{\partial x} = ik_\beta\left(\psi_\beta^+(x) - \psi_\beta^-(x)\right) \tag{5.14}$$

The operator $\mathbf{Q}$ therefore has the form

$$\mathbf{Q} = \begin{bmatrix} ik_1 & -ik_1 & & & \\ & ik_2 & -ik_2 & & \\ & & . & . & \\ & & & ik_n & -ik_n \end{bmatrix} \tag{5.15}$$

Combining Equations 5.12 and 5.13 gives Equation 5.16, which is a series of n equations in the 2n unknowns c_j:

$$2\kappa_i \mathbf{M}_{xs}(\gamma_i,n)\exp(i\kappa_i x_s)$$

$$=\sum_{j}^{2n} c_j \left[\sum_{l}^{2n} E_{xs}(l,j) \int_{-\infty}^{\infty} \kappa_r M_{xs}(\gamma_r,n_c) M_{xs}(-\gamma_r,l) d\gamma_r + \sum_{p}^{2n} Q(n,p) E_{xs}(p,j) \right] \tag{5.16}$$

Applying a similar analysis to the right hand interface of the channel and 2DEG contact, this time matching the flux in the channel with the transmitted flux in the 2DEG contact, gives

$$\sum_{j}^{2n} c_j \left[\sum_{l}^{2n} E_{xe}(l,j) \int_{-\infty}^{\infty} \kappa_r M_{xe}(\gamma_r,n_c) M_{xe}(-\gamma_r,l) d\gamma_r - \sum_{l}^{2n} Q(n,l) E_{xe}(l,j) \right] = 0 \tag{5.17}$$

which are a further n equations in the 2n unknown terms c_j. Equations 5.16 and 5.17 represent a total of 2n equations in 2n unknowns, c_j, and therefore are soluble.

5.3.1 The Conductance

In the experimental measurement of the conductance of a QPC, a very small bias, δV, is applied across the device. This is done in order to minimise carrier heating and the measurements are performed at very low temperatures, often less than one Kelvin. Under such conditions it is reasonable to simplify the conductance calculation, approximating the Fermi function as a Heaviside step function: $f(E,\mu)=\Theta(\mu-E)$, where μ= Fermi energy. The electrons contributing to the current through the QPC are shown schematically in Figure 5.2.

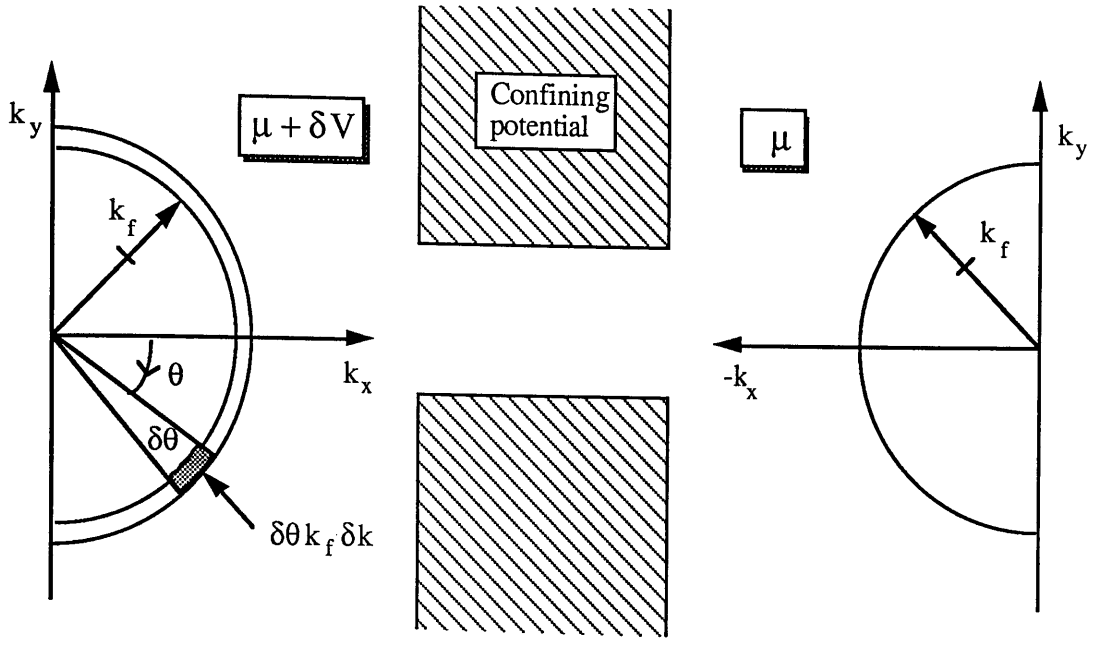

Figure 5.2 Schematic of electrons contributing to the conductance

Only the electrons in the shell of width δk at the Fermi wavevector, k_f, produce a net current flowing through the QPC from left to right.

$$\text{Since } E = \frac{\hbar^2 k^2}{2m}, \tag{5.18}$$

$$\delta k = \frac{m\,\delta E}{\hbar^2 k} = \frac{m\,e\,\delta V}{\hbar^2 k_f} \tag{5.19}$$

The number of states N_s per unit area of real space in the small shaded region is

$$N_s = \frac{2\,\delta\theta\,k_f\,\delta k}{4\pi^2} \tag{5.20}$$

Therefore the current density is

$$J = \int_{-\frac{\pi}{2}}^{+\frac{\pi}{2}} \frac{2}{4\pi^2}\, d\theta\, k_f\, \delta k \left\langle \psi_\theta | J_x | \psi_\theta \right\rangle \tag{5.21}$$

where $\left\langle \psi_\theta | J_x | \psi_\theta \right\rangle$ is the current density through the QPC for an electron incident at angle θ from the 2DEG contact.

The conductance can be written as

$$G = \frac{J}{\delta v} = 2 \int_{-k_f}^{k_f} \frac{e\,m}{\hbar^2} \frac{1}{k_x} \langle \psi_\theta | J_x | \psi_\theta \rangle dk_y \tag{5.22}$$

Unfortunately this integral must be performed numerically.

5.3.2 Numerical Study

In this study of the uniform QPC approximation, the quasi-one-dimensional channel is assumed to have a uniform parabolic potential cross section throughout and to be connected at either end to 2DEG contact regions. The conductance is calculated as a function of the Fermi energy without changing the potential of the channel. This is different from the general experimental approach where the channel width is changed by adjusting the gate bias. However, it should not qualitatively alter the results, having already assumed a uniform channel connected to 2DEG contacts.

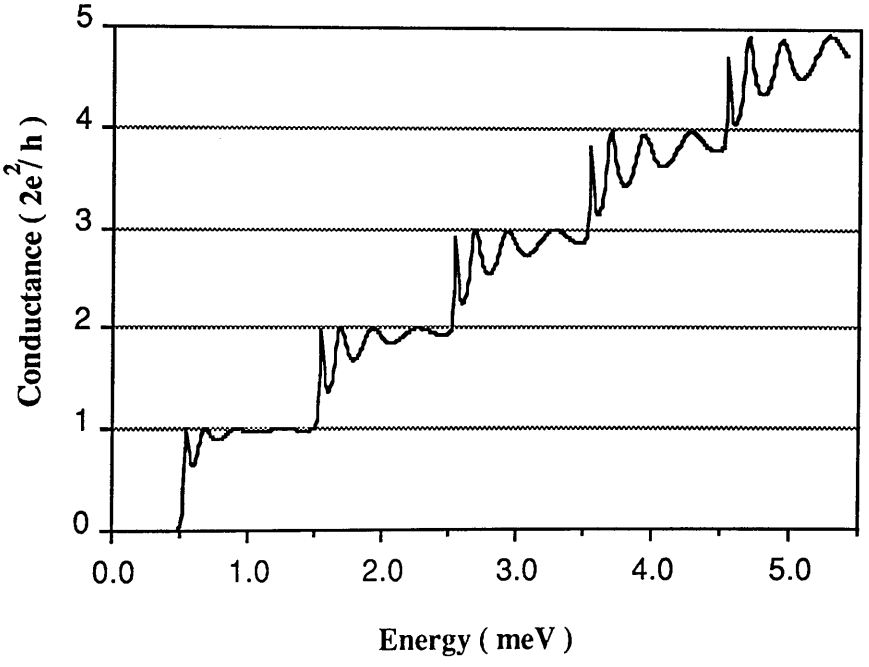

Figure 5.3 Conductance of a uniform QPC, length 0.65μm, temperature 0K

Figures 5.3 and 5.4 show the calculated conductance of two uniform QPCs. In these conductance plots each 'plateau' is separated by 1meV. This separation corresponds to the equal energy spacing between the eigenstates, $\varepsilon_n = \hbar\omega(n + 1/2)$, of a parabolic potential. If tunnelling is assumed to be negligible, then each mode begins to contribute to

the conductance as the Fermi energy increases above the minimum transverse energy ε_n supported by that mode. A different transverse potential will produce different energy spacings between the plateaux, which would mirror their transverse eigenstates' energy spacings.

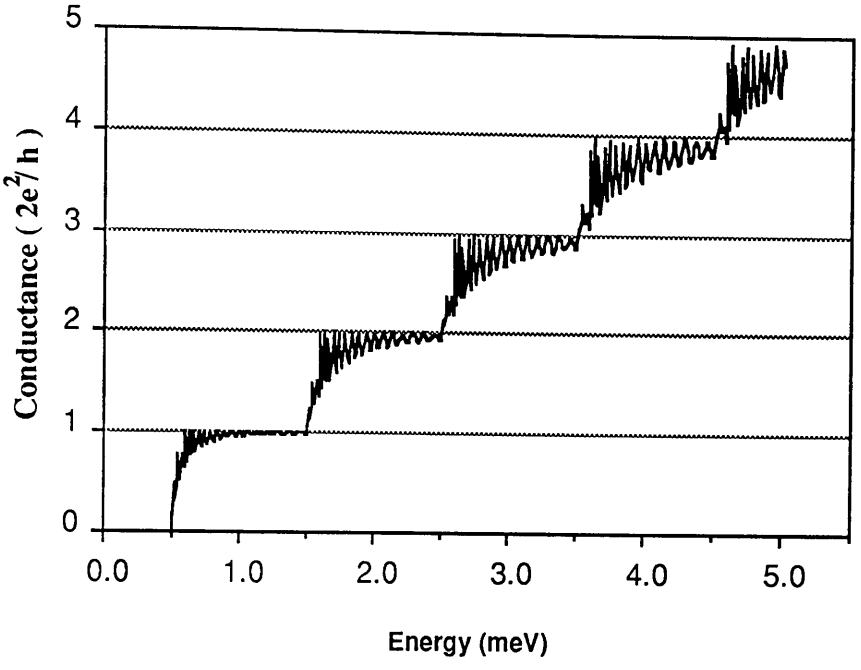

Figure 5.4 Conductance of a uniform QPC, length 3.3μm, temperature 0K

Each of the conductance plateaux contains a series of oscillations which were not predicted by the calculation of Section 5.2. This resonance structure was first calculated by Kirceznow *(Kirceznow 1989)*. Implicit to the calculation of Section 5.2 was the assumption that all modes become fully occupied when the Fermi energy is greater than the transverse energy of the mode. The difficulty with this is that the electrons in the quasi-one-dimensional system originate from the electrical contacts, which are approximated by infinite 2DEG regions.

In order to accurately model the experimental system, it is necessary to include the interface regions from which the electrons from the contacts enter the quasi-one-dimensional system. By using ideal leads, in which all available modes are fully occupied, one is assuming a physical system of an adiabatic horn. In the heart of the 2DEG contact there are an infinite number of quasi-one-dimensional channels which form the two-dimensional density of states filled up to the Fermi energy. As electrons in the positive k_x half space travel down the adiabatic horn, modes pass through cut-off and electrons are reflected. Eventually, only a small number of modes survive, which have remained fully occupied on their passage from the heart of the reservoir in the 2DEG contact region (see Section 6.6.1).

The abrupt interface with the 2DEG contacts in this numerical calculation is very different from the ideal leads assumed in the analysis of Section 5.2. It would appear that this abrupt interface is the cause of the oscillatory structure of the numerically calculated conductance. These oscillations are analogous to the 'over the top' resonances of a one-dimensional potential barrier. A factor in the strength of these oscillations is the one-dimensional nature of the uncoupled transport, in which each mode is treated independently with its own zero-point energy and overlap matrix with the 2DEG contact regions $\mathbf{M}_n$.

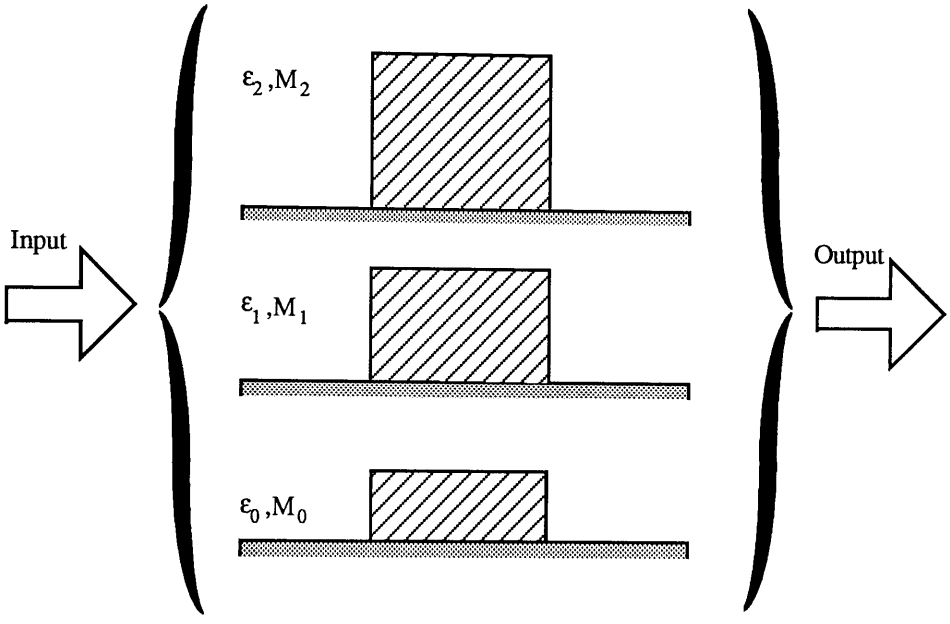

Figure 5.5 One-dimensional equivalent of a uniform QPC

Clearly, this calculated conductance differs from the experimentally measured conductance of Figure 1.1, in which no oscillatory structure has been observed. In an attempt to improve the model of the QPC, the effects of the non-zero temperature of the experimental structures can be modelled by transforming the zero temperature calculation using

$$G(T,E) = \int_0^\infty G(0,\varepsilon)\left(-\frac{\partial f}{\partial \varepsilon}\right)d\varepsilon \qquad (5.23)$$

where G(0,E) = zero temperature conductance and

$$f(\varepsilon) = \text{Fermi function} = \left[\exp\left(\frac{\varepsilon - E_f}{kT}\right) + 1\right]^{-1}.$$

This transformation to finite temperature has been performed in Figure 5.6. The inclusion of this temperature correction smooths out the resonance curves as a direct consequence of the smearing of the Fermi surface.

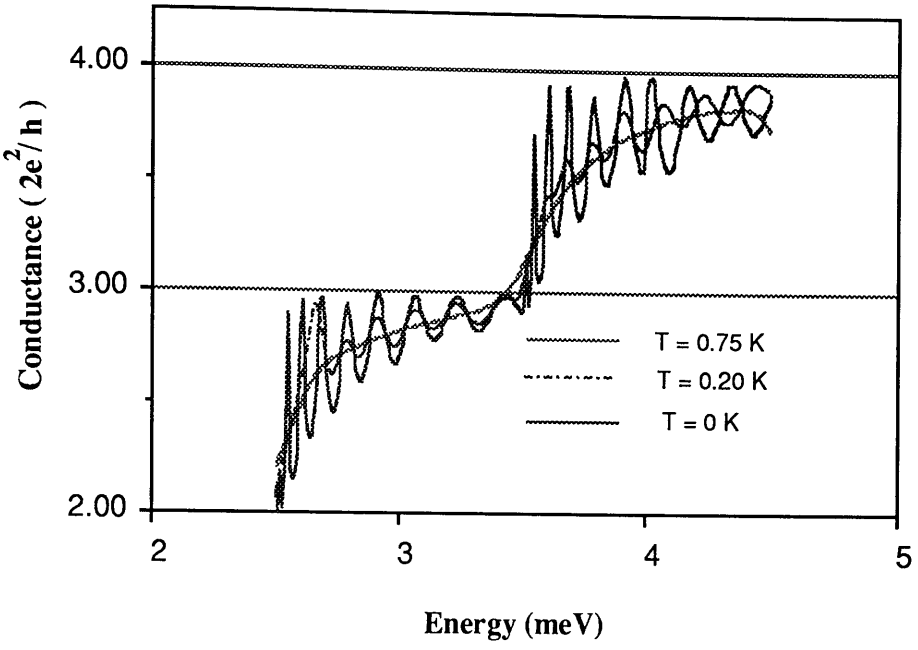

Figure 5.6 Calculated temperature dependence of conductance

At a temperature of 750 mK the resonance structure has been smoothed out but, in averaging over the rapid fluctuations, the step profile in the conductance has been destroyed. Experimentally, van Houten *et al (van Houten 1990)* have found that the most accurately quantized conductance plateaux are observed at a temperature of 500 mK.

5.4 An Ideal QPC Connected to a 2DEG

So far, we have used a simple potential model which has produced qualitative agreement with experimental observations. However, in order to understand, amongst other things, the absence of plateau resonances in the experimental measurements, it is necessary to move one step closer to the actual potential seen by the electrons in the QPC.

Kumar, Laux and Stern *(Kumar 1990)* were the first group to attempt to model self-consistently the electrostatic confining potential below the surface of the sample. They found that the high wave-vector components of the surface gate potential were attenuated in the QPC, resulting in a rounding of the junction made with the 2DEG. This result was confirmed by the work of Nixon and Davies, which is discussed in Chapter Six.

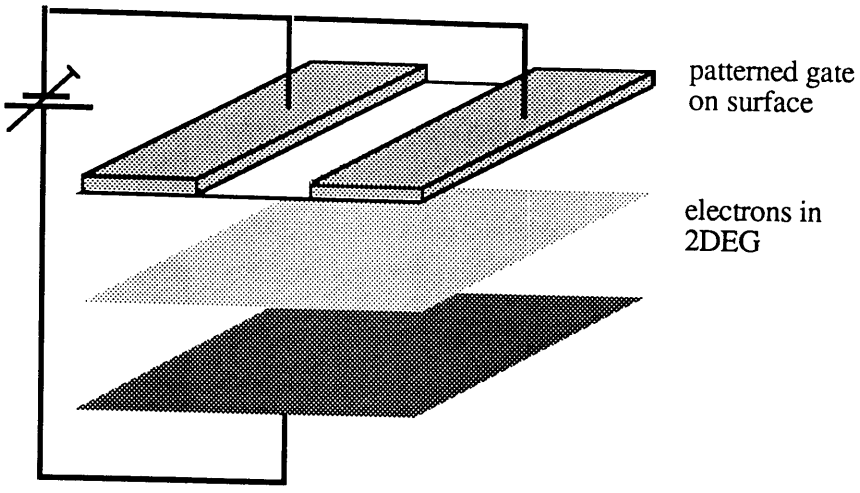

Figure 5.7 Schematic of the squeezed gate arrangement

Figure 5.8 illustrates a section of a self-consistent potential calculated by Nixon and Davies, where the tapering of the channel is clearly visible.

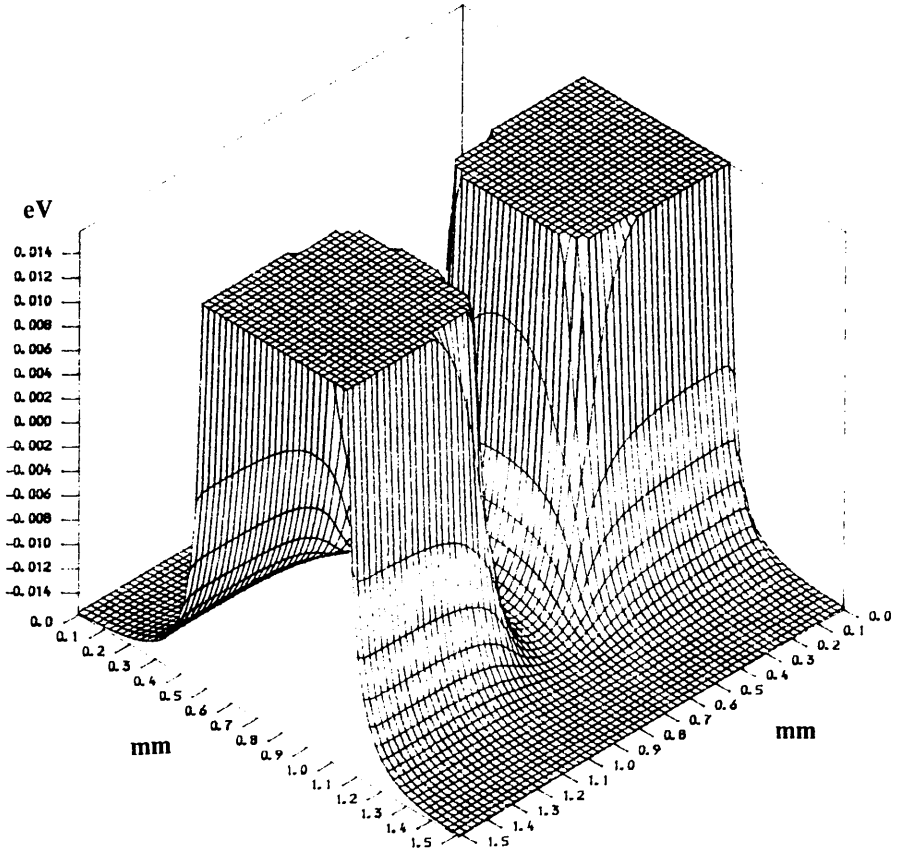

Figure 5.8 Self-consistent potential of a QPC. The vertical energy axis has been offset so that zero represents the Fermi energy.

To calculate the conductance of this non-uniform channel, the method first developed in Chapter Four was employed to determine a set of independent vectors for the channel up to, but not including, the interfaces with the 2DEG. This matrix of independent vectors effectively replaces the matrices $\mathbf{E}_{xs}$ and $\mathbf{E}_{xe}$ in Section 5.3. The independent vectors were then coupled with the contacts using Equations 5.16 and 5.17 to model the entire system. A calculation of the available modes in the channel indicated that there was a gradual increase as one moved out from the narrowest region of the constriction but, after reaching ten available modes, the channel widened very rapidly. Based on these findings, the conductance calculation assumed that, after the channel had widened to the point at which ten modes were available, the system could be approximated by a 2DEG.

Figure 5.9 shows the calculated conductance of this smooth self-consistent QPC potential. It shows that, even for this 0K calculation, the oscillatory structure in the conductance of this device is negligible, and the quantized steps are very accurate. The spacing between the potential steps has also changed from the even spacing of the parabolic potential employed in the prior section, suggesting that the self-consistent potential profile is non-parabolic.

This result provides further evidence that the conductance is very sensitive to the interface between the channel and the contacts. The loss of the resonance structure appears to result from the widening of the channel before the interface with the 2DEG contact. This can be thought of as the introduction of a small section of ideal lead described in Section 5.3.2. However, it is a little surprising to find that such a short tapering section has such an impact on the calculated profile.

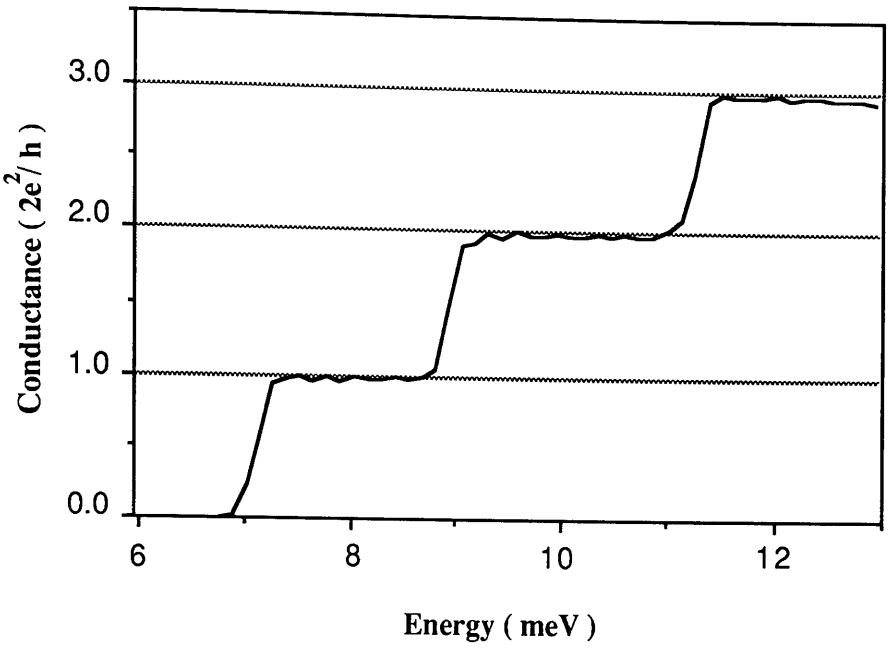

Figure 5.9 Calculated conductance of a self-consistent QPC

5.5 Comparison of Uniform and Ideal QPCs

In order to obtain a more detailed understanding of the transport of a QPC it is necessary to replace the 2DEG contacts with ideal leads connected to the sample. These leads will be discussed in more detail in Section 6.6, but at this point it is necessary to introduce the relationship between the transmission coefficient of the modes of the ideal leads and the conductance.

5.5.1 Relationship between Transmission and Conductance

In 1957 Landauer *(Landauer 1957)* introduced the first expression that related the conductance of a sample to its transmission. This was based on a one-dimensional (1D) barrier connected with ideal 1D wires to some external source which drives a current through the system. Under these circumstances Landauer determined that the conductance of the barrier is given by

$$G = \frac{e^2 T}{\pi \hbar R}. \tag{5.24}$$

where the barrier is characterized by a transmission coefficient T and a reflection coefficient $R = T - 1$.

An alternative 1D formula *(Imry 1986)* that relates the conductance to the transmission coefficient is given by

$$G = \frac{e^2 T}{\pi \hbar} \tag{5.25}$$

Over recent years there has been considerable controversy over the applicability of these two formulae *(Landauer 1989)*. When the transmission is poor, $R \approx 1$. The two formulae are then consistent with the basic understanding that the conductance is proportional to the transmission through the sample. However, when the sample has perfect transmission, Equation 5.24 gives an infinite conductance, whereas Equation 5.25 gives the finite conductance

$$G = \frac{e^2}{\pi \hbar}. \tag{5.26}$$

In order to understand this difference it is useful to show the derivation of these two conductance formulae.

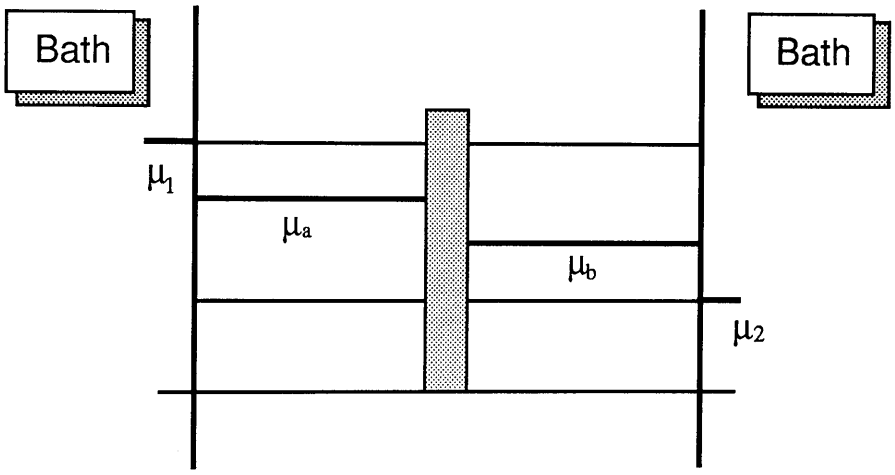

Figure 5.10 Schematic of the various chemical potentials of the system. μ_a and μ_b are the chemical potentials in the left and right ideal leads.

Following Büttiker *(Büttiker 1985)*, the sample, including the scattering centre, is connected to one-dimensional electron reservoirs by perfect one-dimensional conductors. The reservoir (bath) on the left of Fig 5.10 injects carriers into the wire up to the characteristic Fermi energy μ_1 and the reservoir to the right of the barrier injects carriers up to the Fermi energy μ_2. The electron reservoirs are random baths similar to black body radiators, and the outputs are correspondingly incoherent.

The net current flow between the two reservoirs is given by

$$I = T 2 e v \frac{\partial n}{\partial E}(\mu_1 - \mu_2) \tag{5.27}$$

where v is the Fermi velocity, $\partial n / \partial E$ is the density of states per spin with positive velocity, T is the probability of transmission across the sample and R = T – 1 is the probability of reflection. In one dimension $\partial n / \partial E = 1/\pi \hbar v$, which leads to a cancellation of the velocity term, so that

$$I = T 2 \left(\frac{e}{\pi \hbar}\right)(\mu_1 - \mu_2) \tag{5.28}$$

Inside the perfect one-dimensional wires the chemical potentials are defined such that the number of occupied states above μ_a is equal to the number of empty states below μ_a. Therefore

$$T \frac{\partial n}{\partial E}(\mu_1 - \mu_b) = (2 - T)\frac{\partial n}{\partial E}(\mu_b - \mu_2) \tag{5.29}$$

The same reasoning is applied to the chemical potential μ_b to the right of the sample to give

$$(1 + R)\frac{\partial n}{\partial E}(\mu_1 - \mu_a) = (1 - R)\frac{\partial n}{\partial E}(\mu_a - \mu_2) \tag{5.30}$$

There are now two alternative definitions of the potential difference across the system. If the potential difference is defined as that measured between the electron reservoirs then

$$eV = \mu_1 - \mu_2 \tag{5.31}$$

which, when substituted into Eqn 5.28, gives the alternate conductance formula Eqn 5.25. Alternatively, if the potential difference across the system is defined as that in the perfect leads, then

$$eV = \mu_a - \mu_b \tag{5.32}$$

Substituting this into Equations 5.29 and 5.30 gives $eV = R(\mu_a - \mu_b)$ which, when combined with Eqn 5.28, recovers the original Landauer conductance formula, Eqn 5.24.

These derivations show that the crucial difference between the two forms of the conductance formula is the position at which the potential is measured. To obtain the original formula of Landauer, the potential difference is measured in the perfect leads on either side of the scattering object. The alternative formula (Eqn 5.25) is recovered by measuring the potential difference between the electron reservoirs. These are characterized by well-defined chemical potentials, which implies a large heat and particle reservoir.

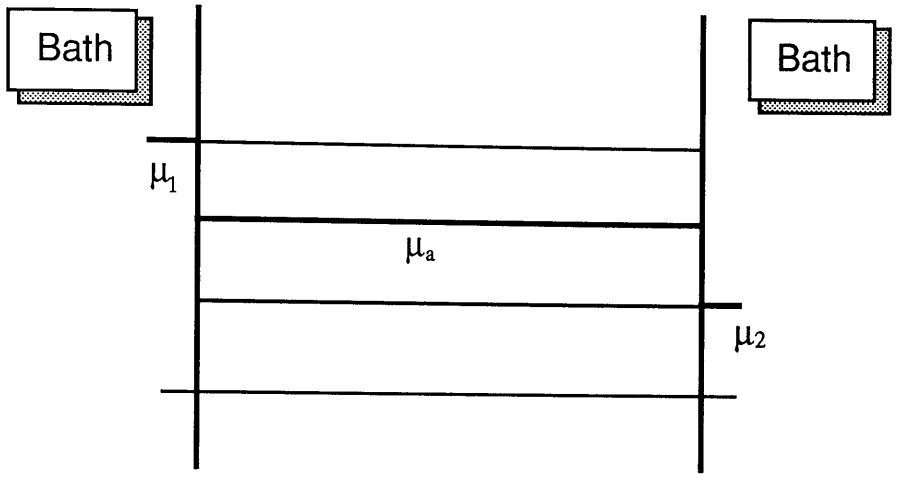

Figure 5.11 A perfect one-dimensional conductor with chemical potential μ_a

Landauer *(Landauer 1987)* has shown that electron reservoirs which randomize the phase of the incident electrons are a necessary component of a system that measures a resistance. In 1D, however, these reservoirs can appear a little abstract. For example, Figure 5.11 illustrates the situation where the transmission of the ideal lead is perfect. In this situation all of the forward and backward travelling states in the reservoirs are filled up to their respective Fermi energies and in the ideal lead there is only a net forward current. Following Equations 5.29 to 5.30 with T = 1 and $\mu_a = \mu_b$

$$\frac{1}{2}(\mu_1 - \mu_2) = \mu_1 - \mu_a \tag{5.33}$$

$$R_c = \frac{h}{4e^2} \tag{5.34}$$

This has been defined as the contact resistance *(Imry 1986)*, which appears a little unusual in a system in which all the components are one-dimensional. However, the actual systems measured experimentally have contacts which are approximated by 2D electron reservoirs. Therefore, the alternate Landauer formula (Eqn 5.25) has been used, since it more closely resembles the system in which the conductance measured experimentally.

Fisher and Lee *(Fisher 1981)* have generalized this result to N channels, obtaining the result

$$G = \frac{2e^2}{h} \mathrm{Tr}\left(t^{\dagger} t\right) \tag{5.35}$$

where t is the N × N transmission matrix connecting the incident flux in various channels on one side of the system to outgoing flux in the channels on the other side. $|t_{ij}|^2$ is the probability of flux input in the channel j emerging in channel i. This formula has had considerable success in the study of mesoscopic systems *(Stone 1988)*.

5.5.2 Numerical Results

A useful facility of the computation is the ability to use the intrinsic modal nature of the calculations to determine the individual modal contributions to the conductance of a QPC.

In the modal analysis, the wavefunction is expanded in terms of the eigenfunctions $\phi_n(x,y)$ of the local transverse potential, with energies $\varepsilon_n(x)$. The wavefunction is partially separated throughout the length of the constriction into:

$$\Psi(x,y) = \sum_n \left\{ c_n^{+}(x)\exp(i k_n x) + c_n^{-}(x)\exp(-i k_n x) \right\} \phi_n(y) \tag{5.36}$$

where $c_n^{\pm}(x)$ is the amplitude of the electrons travelling forwards (+) or backwards (–) in the n^{th} transverse mode.

The results can be expressed in terms of t and r matrices defined by

$$t_{kj} = \sqrt{\frac{k_k(x)}{k_j(x=0)}} \frac{c_k^{+}(x)}{c_j^{+}(x=0)} \tag{5.37}$$

and

$$r_{kj} = \sqrt{\frac{k_k(x)}{k_j(x=0)}} \frac{c_k^{-}(x)}{c_j^{+}(x=0)}, \tag{5.38}$$

where $x = 0$ is the left-hand edge of the system. Then $|t_{kj}(x)|^2$ is the probability that flux input in mode j is travelling forward in mode k at x, and similarly $|r_{kj}(x)|^2$ is the probability that flux input in mode j is travelling backward in mode k at x.

The dimensionless conductance (in units of $2e^2/h$) is given in terms of the overall t matrix $G = Tr(t^\dagger t)$. The t matrix reduces to the identity matrix in an adiabatic system and there is perfect quantization with $G = n_{min}$, where n_{min} is the total number of modes which continue to propagate throughout the constriction at the Fermi energy.

To study the transport, we define

$$a_k^+(x) = \sum_j \left|t_{kj}(x)\right|^2, \quad a_k^-(x) = \sum_j \left|r_{kj}(x)\right|^2. \tag{5.39}$$

Then $a_k^\pm(x)$ is the probability of occupancy of the forward (+) or backward (–) mode k at x along the constriction, irrespective of the mode in which the electron entered the system.

Figure 5.12a shows the net conductance of a uniform QPC, while Figures 5.12b and 5.12c respectively show the forward and backward contributions to this net conductance as the Fermi energy of the electrons in the 2DEG is varied. Since this is a uniform QPC, the modal contributions remain constant along the length of the QPC channel.

From Figure 5.12b it can be seen that, as the QPC passes through resonance, the forward modal contribution exceeds $n2e^2/h$. This results in a build-up of flux in the cavity of the QPC by repeated scattering between the two 2DEG interfaces. Despite the excessive conductance contribution of some forward modes, each net modal current never exceeds $2e^2/h$, as required by unitarity.

At other energies the conductance, and hence the modal occupancy, is less than unity. The coupling of the channel to the 2DEG is poor and very different from the perfect coupling of ideal leads. It is only when the Fermi energy is well above the minimum propagation energy that the coupling efficiency is consistently good.

In contrast, Figure 5.13 shows the conductance calculation of the self-consistent QPC on the G = 4 plateau and the modal contribution to the conductance throughout the length of the channel. It shows that the four modes which propagate throughout the structure are efficiently coupled to the contact, but the other modes that are available only at the edges of the system are poorly coupled.

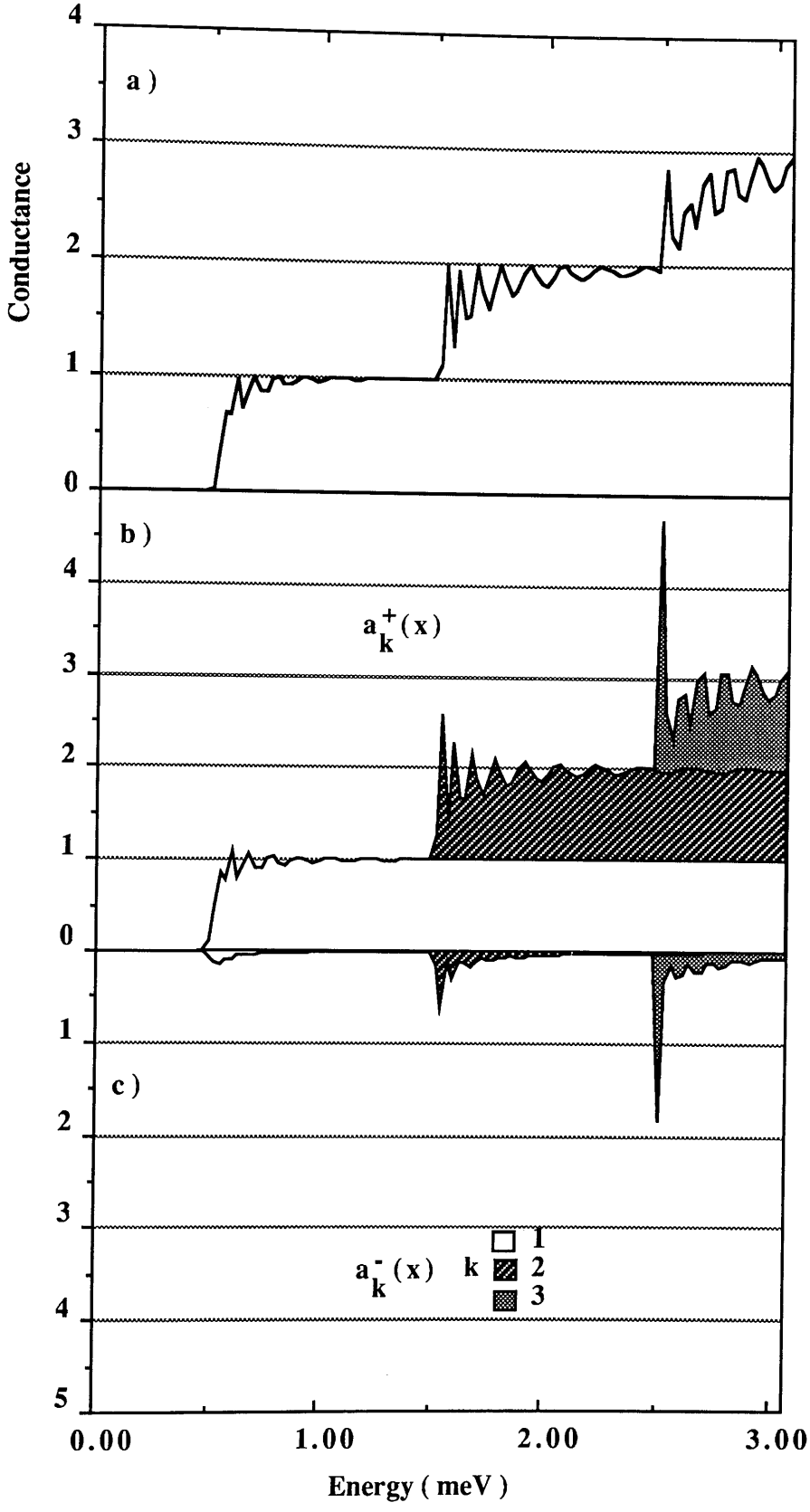

Figure 5.12 Modal analysis of a uniform QPC contacted to a 2DEG

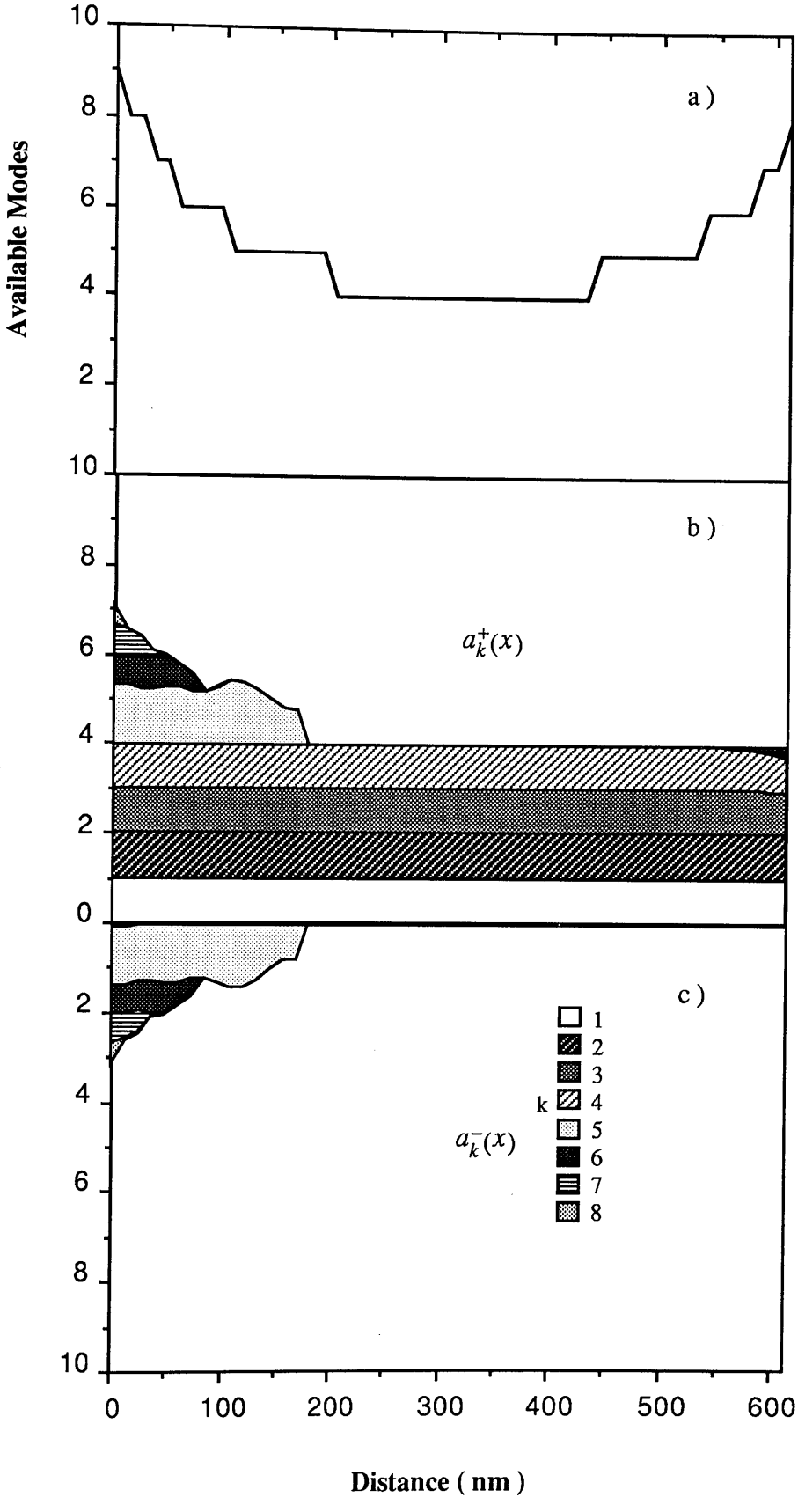

Figure 5.13 Self-consistent QPC connected to 2DEG contacts

Szafer and Stone *(Szafer 1989)* have developed an analytical approximation for the transmission coefficient of a mode passing from a narrow channel into a wider contact region. Known as the *Mean Field Approximation*, this compares well with their exact numerical calculation. It assumes that electrons in a mode in the narrow channel couple evenly to a range of modes in the wider section. This range is bounded by the transverse energies of the modes immediately above and below the one under consideration in the narrow region. Yacoby *et al (Yacoby 1990)* has shown that the interface transmission coefficient for electrons in the s^{th} mode, t_s, can be approximated by

$$t_s = 1 - \frac{1}{64}\left[\frac{n_a}{n_a^2 - s^2}\right]^4 \tag{5.40}$$

This is valid for $n_a \geq n_{max} + 1$, where n_a is the total number of available modes at the interface and n_{max} is the number of modes occupied by electrons. This shows that, at the interface, the electrons occupying modes well below the maximum available mode will be only weakly scattered. An ideal scenario for transmission would therefore have only the lowest of many available modes occupied at the interface. This could be obtained by widening the channel at a sufficiently slow rate that the electrons propagate adiabatically and do not scatter into the higher modes as they become available.

Although this approximation applies to a single interface, its attributes do carry over qualitatively into the QPC system. This can be seen in the abrupt QPC, Figure 5.12, where the improved coupling of the lower modes is witnessed by the reduction in the reflected flux as the higher modes become available. In the self-consistent QPC, Figure 5.13, the non-unitary occupancy of modes that are cut off as the channel narrows indicates that the interfaces are not transparent. The fifth forward mode exceeds unity as a result of repeated scattering between the interface to the left and the point at which the mode is cut off in the channel. However, the net modal contribution is zero, as is the net conductance of all higher modes cut-off to the left of the narrowest section of the channel. All conducting modes are efficiently coupled to the 2DEG contacts, and each provides an integer contribution to the normalized conductance at the entry to the left of the channel. After passing through the narrowest region of the channel, there is a small amount of forward scattering out of the fourth mode into the sixth. At the exit, with $n_a = 9$ and $n_{max} = 6$, t_s is of the order of one for all the occupied modes. This is consistent with the conductance calculation, which shows most of the flux passing out into the 2DEG with only a tiny amount of backscattering. Overall, the smooth QPC appears adiabatic up to the narrowest section of the channel, with each of the four conducting modes providing a unit contribution to the conductance and with no intermode scattering.

The nature of the conductance calculation of a channel connected to a 2DEG contact means that it is only possible to obtain the overall occupancy of each mode in the system. However, if the channel were to be connected to ideal leads, it would then become possible to analyse the scattering further in terms of the mode in which the electrons entered the sample. Define

$$b_j^+(x) = \sum_k |t_{kj}(x)|^2, \quad b_j^-(x) = \sum_k |r_{kj}(x)|^2, \tag{5.41}$$

so that $b_j^{\pm}(x)$ is the probability that flux input in mode j is travelling forward (+) or backward (–) at x, irrespective of which mode it is in at x. Thus $b_n^{\pm}(x)$ resolves the flux into contributions from the *input* modes, whereas $a_n^{\pm}(x)$ (Equation 5.39) resolves the flux into contributions from the *local* modes at x. This provides information as to the origins of the flux in each mode throughout the structure, with the overall conductance obtained by summing up the contributions of each fully occupied mode in the ideal lead at the entrance to the device.

In Figure 5.14 the conductance of the self-consistent QPC has been calculated using ideal leads. It is seen that the overall conductance of G = 4 is identical to the structure connected to 2DEG contacts, but the use of ideal leads has enabled the flux to be identified by the mode in which the flux *entered* the structure. The nature of the ideal leads can be seen at the entrance to the device, where all available modes are fully occupied. At the end of the device the ideal leads would have eliminated any interface scattering present when connected to the 2DEG contacts.

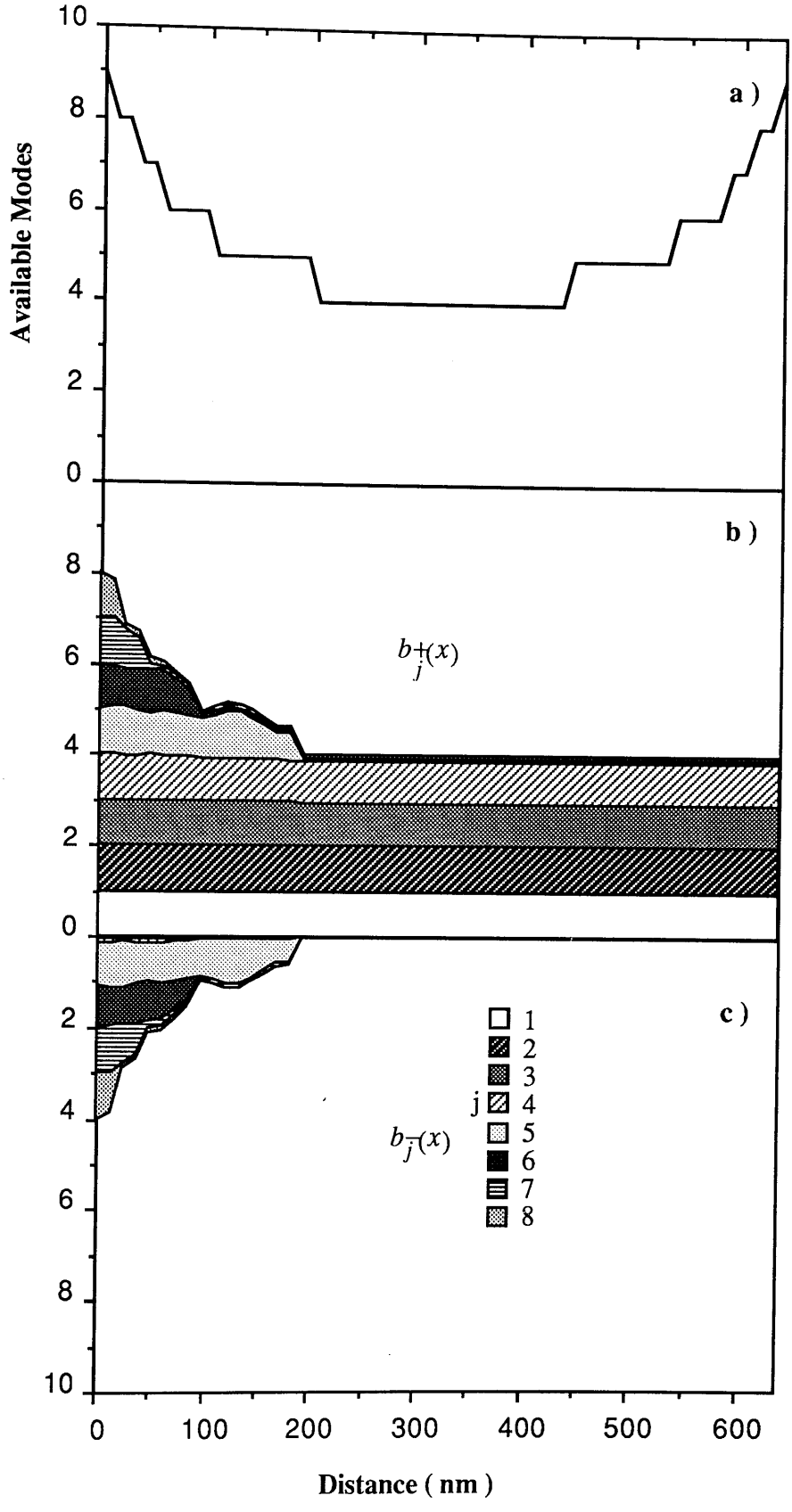

Figure 5.14 Self-consistent QPC connected to ideal leads

The central region of Figure 5.14b is expanded in Figure 5.15. It can be seen that in the narrowest region of the the device, where there are only four conducting modes, there is a small contribution to the flux from electrons that entered the structure in modes five and six. This indicates that, even in ideal structures that produce good quantized conductance characteristics, the transport is not totally adiabatic.

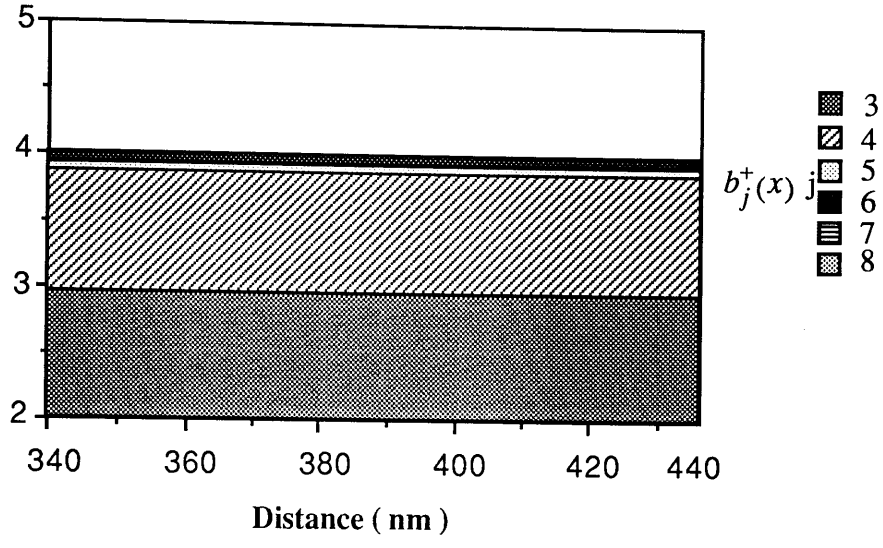

Figure 5.15 Detail of central region of Figure 5.14

The validity of the use of different boundary conditions and the subsequent comparison of the results is discussed in more detail in Chapter Six. At this point, the observation is made that in the current structure the change in boundary conditions will have a negligible impact on the conductance. This is because all of the conducting modes are well coupled to the contact and there is very little reflection from the conducting modes at the right-hand interface with the 2DEG.

5.6 Summary

This chapter began with an analytical approximation of the quantized conductance. When this was compared with a numerical calculation of the conductance of a uniform QPC, the latter was found to have a significant oscillatory structure. This was not predicted by the original analytical calculation, which had implicitly assumed that the QPC was connected by ideal leads. A correction for non-zero temperature was applied to the oscillatory conductance, but this was found to be insufficient to fully explain the lack of any resonance structure observed experimentally. A detailed calculation of the modal contributions to the conductance in the uniform QPC revealed an energy dependence in the coupling efficiency to the available modes inside the constriction.

A more realistic self-consistent model of the gate potential was found to possess a tapered region connecting the narrowest section of the channel to the 2DEG contacts. The conductance of this potential structure was calculated by combining the general formalism of the independent vector propagation of Chapter Four with the 2DEG interface matching of this chapter. The conductance calculations revealed that the tapers vastly improved the coupling efficiency to the 2DEG contacts over a continuous energy range and led to the virtual elimination of oscillations, even at 0 K. However, an investigation of the modal origins of the flux in the central region of the device indicated that transport was not totally adiabatic.

This chapter has shown how sensitive the conductance profile of a QPC is to the shape of the confining potential. As the model of the QPC potential has become more realistic, so has the profile of the calculated conductance. In Chapter Six the model of the QPC is extended to include the potential contribution of the ionized donor atoms above the plane of the 2DEG.

Chapter Six
The Realistic Quantum Point Contact

6.1 Introduction

In Chapter Five, the characteristics of the conductance of a QPC were found to be very sensitive to the potential profile of the channel. As a first stage towards modelling a realistic QPC, a self-consistent potential which did not consider the ionized donor layer was studied. The characteristic feature of this potential was the tapered section connecting the narrowest region of the channel to the 2DEG contact. This curved interface was found to have a significant influence on the conductance and led to the elimination of the resonance structure observed in the abrupt QPC model.

In this chapter, the transport through realistic potential profiles is modelled. These realistic self-consistent potentials include the non-self-averaged ionized donor atoms as well as the 2DEG *(Nixon 1988)*. The conductance of these structures is calculated for both 2DEG contacts and ideal leads. By attaching ideal leads, the transport is studied in terms of the modal origins of the flux. This enables a detailed analysis of electron transport in realistic potentials to be carried out. Further insight into the transport is provided by an analytical calculation of the scattering rates based on the Born Approximation.

6.2 The Realistic Potential

The realistic QPC potentials studied in this chapter were calculated by Nixon and Davies *(Nixon 1990)*. The calculated potentials include the contributions from ionized donors, the potential of the gate and also the self-consistent screening from the electrons in the 2DEG. The donors are assumed to be randomly distributed, fully ionized and both the donors and free electrons are assumed to occupy strictly two-dimensional planes.

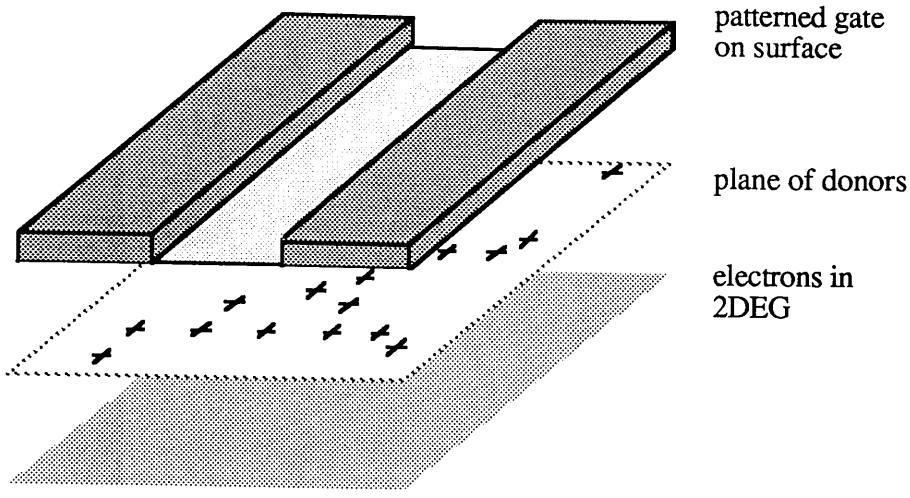

Figure 6.1 Components of realistic potential calculation

Figure 6.2 illustrates a typical gate potential from this calculation. In Figure 6.2a the vertical energy scale has been offset, so that zero represents the Fermi energy.

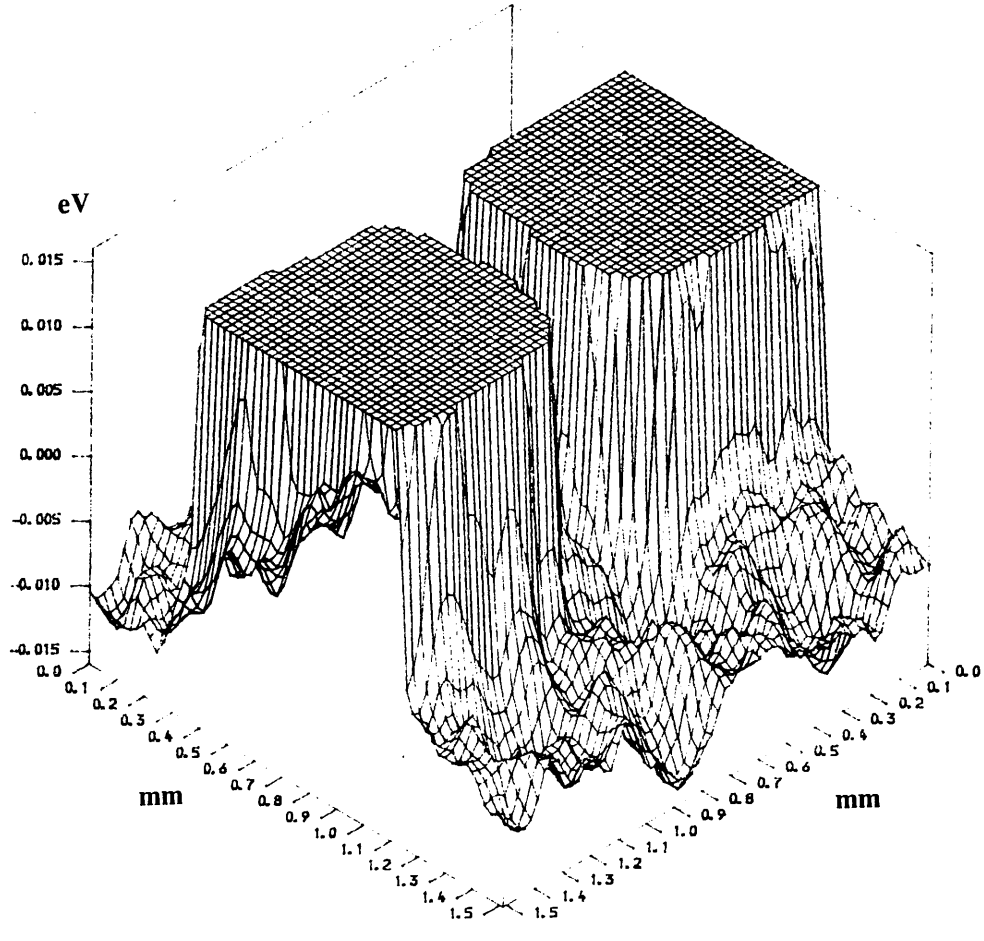

Figure 6.2a Example of a potential profile of a QPC that includes the potential of the ionized impurities

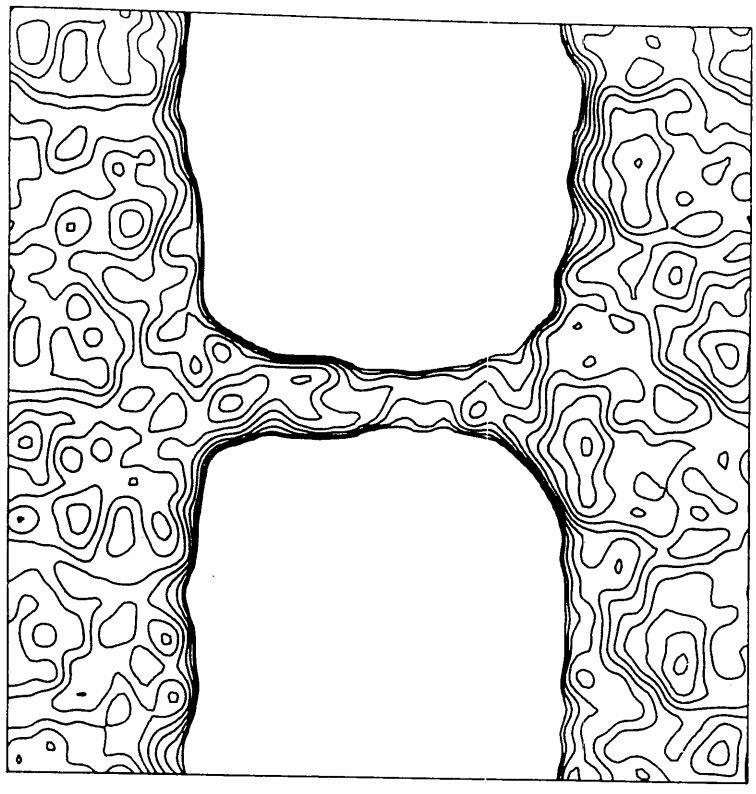

Figure 6.2b Example of a contour plot of a 0.6 μm QPC that includes the potential of the ionized impurities *(Nixon 1991)*. Contours start at zero and are 4.2×10^{14} m^{-2} apart, corresponding to an energy spacing of 1.5 meV.

This model probably represents a worst case scenario. Efros *et al (Efros 1990)* have suggested that there is correlation in the position of donors, and this would reduce the random nature of the potential. The electron screening was also assumed to be purely semiclassical. However, the calculated conductance of this structure, illustrated in Figure 6.3 for various distributions of donors, is seen to be in qualitative agreement with the experimental results of Figures 1.2 and 1.3. These results were calculated assuming that ideal leads were attached to the QPC, and using the recursive Green's function technique. The parameters of the structure were taken from Timp *et al (Timp 1989)* and a schematic of the device structure is shown in Figure 2.6. The gates were 600 nm long with a 300 nm gap between them. Although the doping density of the actual device was 4.0×10^{16} m^{-2}, a fully ionized 2.5×10^{16} m^{-2} donors were incorporated into the model. This reduction was necessary to take into account the fraction of unionized donors in the real system (*Nixon 1991*). Despite showing qualitative agreement with the experimental results, these calculations do not provide an insight into the nature of the transport in the channel.

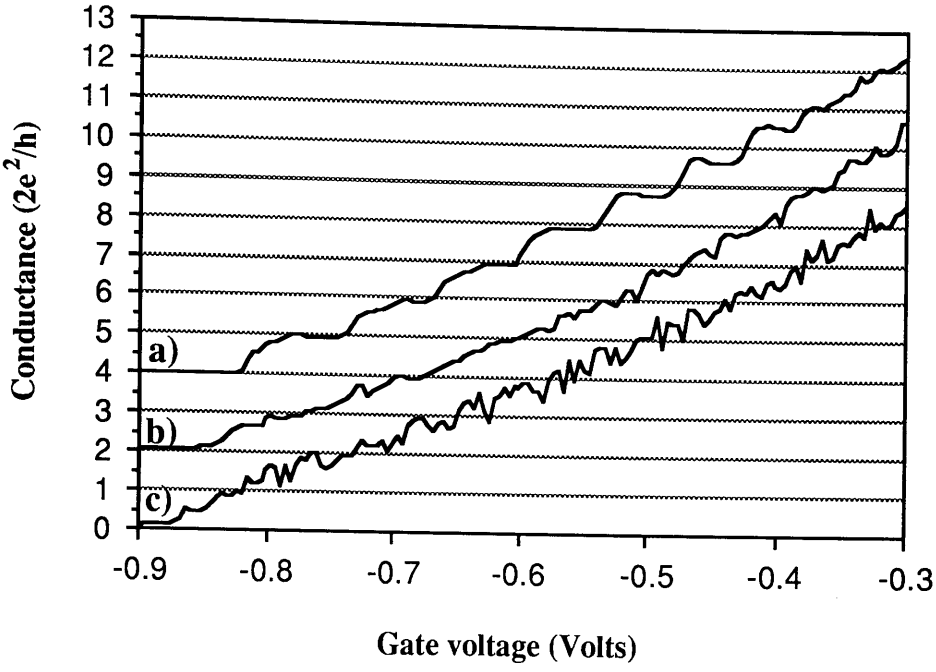

Figure 6.3 Conductance as a function of gate voltage for a variety of randon donor distributions in a 0.6μm QPC The plots have been vertically offset for clarity after Nixon *et al (Nixon 1991).*

In Figure 6.4, the ten lowest eigenvalues of the transverse modes $\varepsilon_n(x)$ are plotted throughout the length of a realistic channel. This represents a departure from the ideal QPCs modelled in Chapter Five, where a smooth variation of the number and energies of modes was expected throughout the structure. With the exception of an energy offset below the lowest eigenvalue, the lower transverse eigenstates' separation remains reasonably constant throughout the structure. This suggests that the potential profile resembles the parabolic profile used in the ideal QPC. However, there is some increase in the energy spacing of the higher modes, which suggests that the potential profile does begin to rise more steeply than the parabola at high energies. Because the lowest eigenvalue is the only mode to remain below the Fermi energy throughout the entire length of the constriction, $n_{min} = 1$, and one would then expect a normalised conductance of G = 1. This is shown to be the case in Section 6.3, where the full modal analysis of this potential is shown as a well-quantized QPC on the G = 1 plateau.

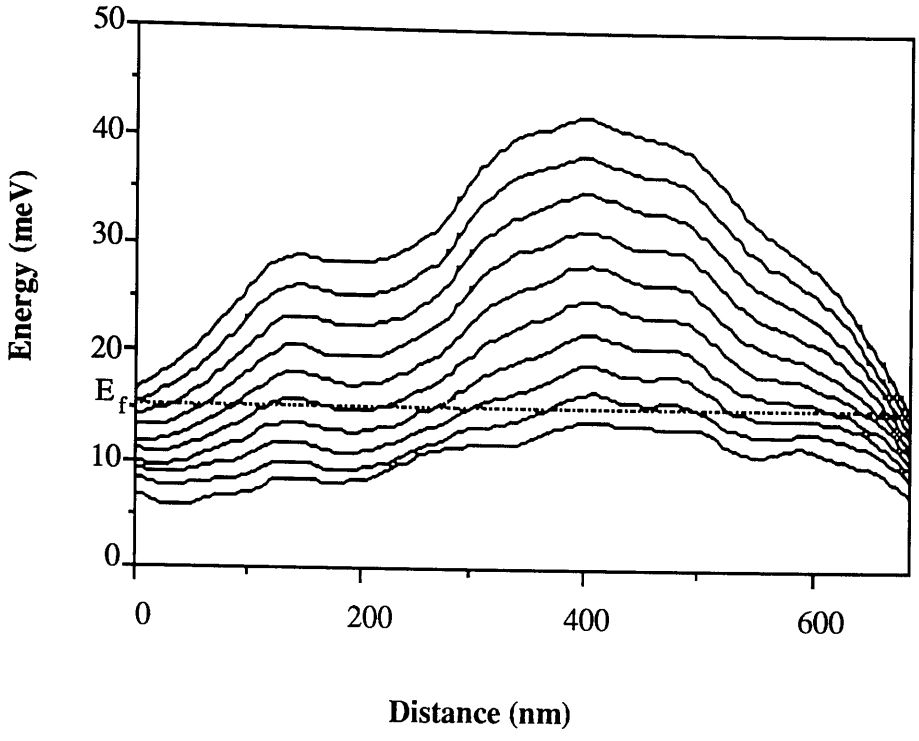

Figure 6.4 Lowest ten transverse eigenvalues of a realistic QPC

6.3 The Conductance of a Well-Quantized QPC

In Figure 6.5 the calculated conductance, assuming 2DEG contacts, of a QPC in a realistic potential is plotted. The realistic potential model employed identical parameters to those used in the previous section. However, the conductance was calculated with 2DEG contacts instead of ideal leads. The calculated conductance shown in Figure 6.5 is in very good agreement with that of Figure 6.3a. This had been determined using the recursive Green's function technique over a potential that included a large but finite contact region.

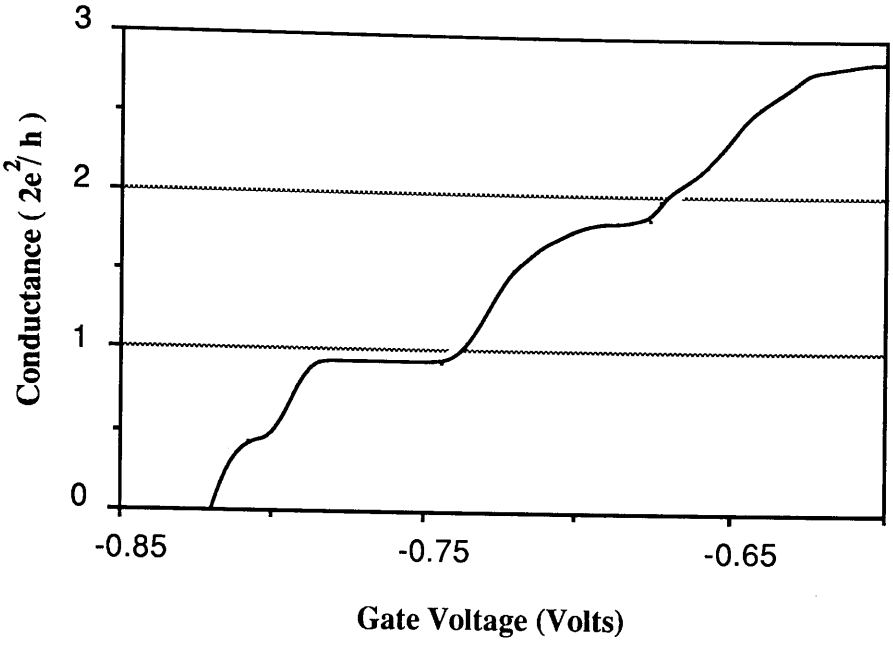

Figure 6.5 Calculated conductance of a 600 nm long realistic QPC attached to 2DEG contacts.

As the conductance increases, the quantized nature of the conductance is seen to deteriorate (Figure 6.5). The lowest plateau is the most accurate, with a 5% error. With the exception of a gate voltage offset, this conductance calculation has very similar characteristics to the experimental results of the 0.6 μm QPC measured by Timp *et al (Timp 1989)* (Figure 1.3). Unfortunately, this must be considered merely fortuitous, since theoretical work by Nixon *et al* (*Nixon 1991* and Figure 6.3), experimental results of Timp *et al* (Figure 1.2) and the current study show that a change in the random distribution of the potential can radically alter the conductance characteristics.

Modal transport through the central region of this QPC is illustrated in Figure 6.6 for the QPC connected to ideal leads. As in Section 5.5, it is necessary to use ideal leads as contacts in order to perform a detailed modal analysis of the transport. The conductance of this device at this bias is well quantized on the first plateau, G = 1. This is a slight increase on the conductance calculated when the QPC is connected to 2DEG contacts (Figure 6.5), and this will be discussed in more detail in Section 6.5. The electron density in Figure 6.6a shows fluctuations caused by the random potential. The number of propagating modes, n_m, at each point along the length of the channel is superimposed on the modal contributions of Figure 6.6b. The minimum, $n_{min} = 1$, is the number of conducting modes throughout the constriction, and this is consistent with both the findings of Section 6.2 (Figure 6.4) and also the conductance.

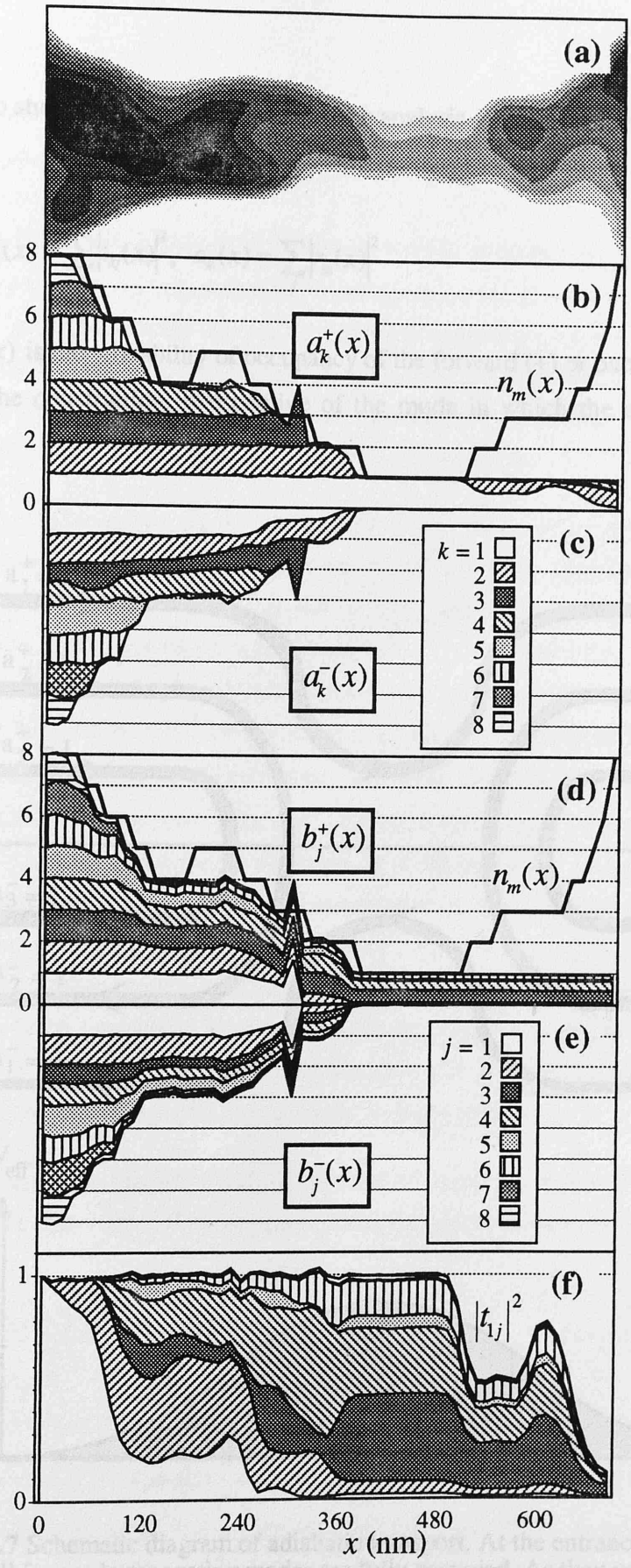

Figure 6.6 Modal analysis of a well quantized QPC.

To study the transport, we follow the analysis of Chapter Five, repeated here, and define

$$a_k^+(x) = \sum_j |t_{kj}(x)|^2, \quad a_k^-(x) = \sum_j |r_{kj}(x)|^2 \qquad (6.1,\ 6.2)$$

Then $a_k^{\pm}(x)$ is the probability of occupancy of the forward (+) or backward (–) mode k at x along the constriction, irrespective of the mode in which the electron entered the system.

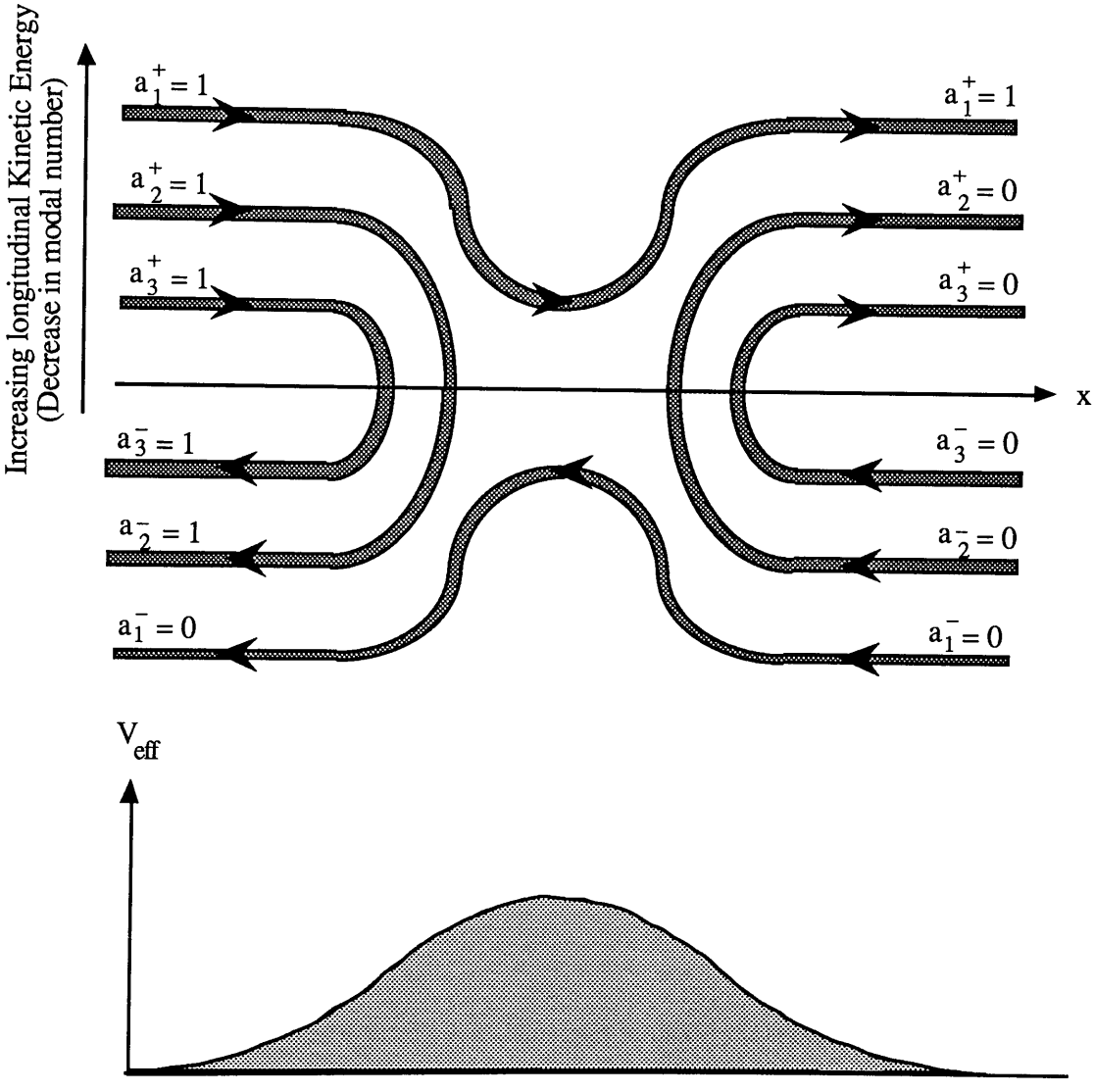

Figure 6.7 Schematic diagram of adiabatic transport. At the entrance to the structure (left) all forward propagating modes are fully occupied. As they pass through the constriction, some modes pass through cut-off and are completely reflected. Those modes that do not pass through cut-off remain fully occupied throughout the entire channel length of the channel and do not scatter into any other modes.

If transport were adiabatic, each $a_k^+(x)$ would remain unity until cut-off, at which point it would be entirely reflected into $a_k^-(x)$, as shown in Figure 6.7.

At first sight, Figure 6.6b for the forward occupancy $a_k^+(x)$ appears to support this, with each mode remaining approximately full until it is cut off. However, there is resonance in the third mode at cut-off and there is scattering after the narrowest part of the constriction as soon as higher modes become available. The absence of any flux on the right-hand side of Figure 6.6c for backward occupancy indicates that this scattering to the right of the narrowest region is purely forward in nature.

No conclusion can be drawn on scattering at the interface of the channel and the leads, since interface transparency is a property of ideal leads. Any backward scattering to the right of the *narrowest* region would have severely deteriorated the quantized conductance. This is because it would have reduced the forward flux which, by this point in the constriction, already represents a measurement of the minimum number of available modes. In addition to the forward scattering, the occupancies of the backward-going modes $a_k^-(x)$, shown in Figure 6.6c, are also inconsistent with the adiabatic approximation. In particular there is a substantial occupation of the lowest mode. This backward travelling mode should be empty, because the lowest forward mode propagates throughout the structure. The forward mode remains fully occupied until it has passed through the narrowest region of the channel, after which some of the electrons are scattered into other modes. This scattering out of the lowest mode to the right of the narrowest region has already been shown to be forward in nature, and therefore cannot be the source of the flux in the lowest backward travelling mode. The actual source of this backward travelling flux in the lowest mode is analysed below.

To study the scattering further, we have analysed the flux in terms of the modes in which the electrons *entered* the sample. Again, following Chapter Five, we define

$$b_j^+(x) = \sum_k \left|t_{kj}(x)\right|^2, \quad b_j^-(x) = \sum_k \left|r_{kj}(x)\right|^2. \qquad (6.3,\ 6.4)$$

Then $b_j^\pm(x)$ is the probability that flux input in mode j is travelling forward (+) or backward (–) at x, irrespective of which mode it is in at x. Thus $b_n^\pm(x)$ resolves the flux into contributions from the *input* modes, whereas $a_n^\pm(x)$ resolves the flux into contributions from the *local* modes at x. There is no scattering in the adiabatic limit, which implies that $b_n^\pm(x) = a_n^\pm(x)$. This is clearly not the case, as shown by Figure 6.6d.

In particular, the lowest mode b_1^+ makes a tiny ($\approx$2%) contribution to the conductance. The origins of the flux in this mode, the only conducting mode in this system, are shown in Figure 6.6f, where $|t_{1j}|^2$ is plotted. Most electrons that enter the sample in this mode are rapidly scattered out, but they are replaced by electrons that entered in higher modes, so that the total flux remains close to unity. In this process of reciprocity, the flux scattering out of the lowest mode is balanced by flux scattering into the same mode. This can only maintain the full occupancy of the lowest mode for as long as the associated scattering modes remain fully occupied, thus maintaining the equilibrium. At the beginning of the constriction, the electrons scattering out of the lowest mode are replaced with electrons that were originally in the second mode. It is unlikely that there would have been substantial scattering of electrons out of the second mode in such a short distance. It is therefore reasonable to suggest, as shown by Figure 6.6f, that the principal scattering process of electrons originally in the lowest mode at the beginning of the constriction is forward scattering into the second mode.

The fractions contributed by the different incident modes remain constant only in the narrowest region of the constriction, where $n_m = n_{min}$. This is the sole region where transport can be said to be adiabatic. Even this is not true in a wider constriction with $n_{min} > 1$, where we have found scattering between the conducting modes in other well-quantized samples.

The results in Figure 6.6 demonstrate that it is possible to have well quantized conductance even when scattering is strong and the adiabatic approximation fails. Two conditions must be met for quantization: the transmitted modes must be fully occupied when they reach the narrowest part of the constriction, and they must not be back-scattered after this point. These conditions are fulfilled in our system because forward scattering is dominant. This in turn follows from the slowly-varying nature of the random potential in space. Forward scattering allows a 'compensating' process to occur to the left of the constriction. Figure 6.6b shows that all the forward-going modes are fully occupied until they reach cut-off. Electrons that scatter out of one of the transmitted modes into a higher mode can therefore be exactly balanced by electrons scattering via the inverse process. This would not be true if back-scattering were important, because the backward-going modes are not fully occupied and the two rates would not balance. This process of compensation was suggested by Payne *(Payne 1989)*, who studied a channel whose width increased with time. Pure forward scattering is also analogous to a unitary change in the basis, under which $Tr(t^\dagger t)$ remains unchanged *(Büttiker 1990)*. It will be demonstrated in Section 6.5 that, as a direct consequence of disorder in the system, it is not always a precondition of quantized resistance to have all modes fully occupied at the start of the constriction. The freeing of this constraint allows for the possibility of the

observation of quantized resistance when there is poor interface coupling between the channel and the contacts.

Figure 6.8 illustrates the scattering processes taking place in this well-quantized QPC.

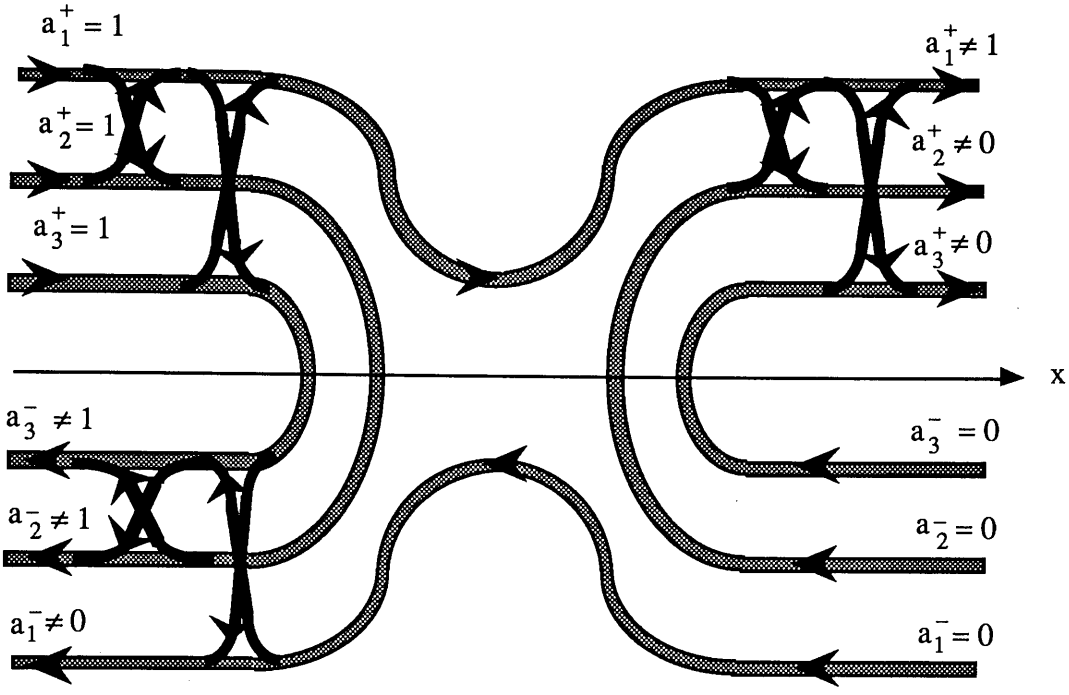

Figure 6.8 Schematic of the transport in a realistic structure showing a selection of the scattering process of the electrons as they pass though the QPC

6.4 The Conductance of a Poorly Quantized QPC

A study of transport in devices whose conductance is poorly quantized has also been made. The full conductance characteristic is shown in Figure 6.3b Figure 6.9 shows the modal analysis of the transport through this QPC, which has identical device parameters to that of Figure 6.6, except for a different random distribution of ionized impurities.

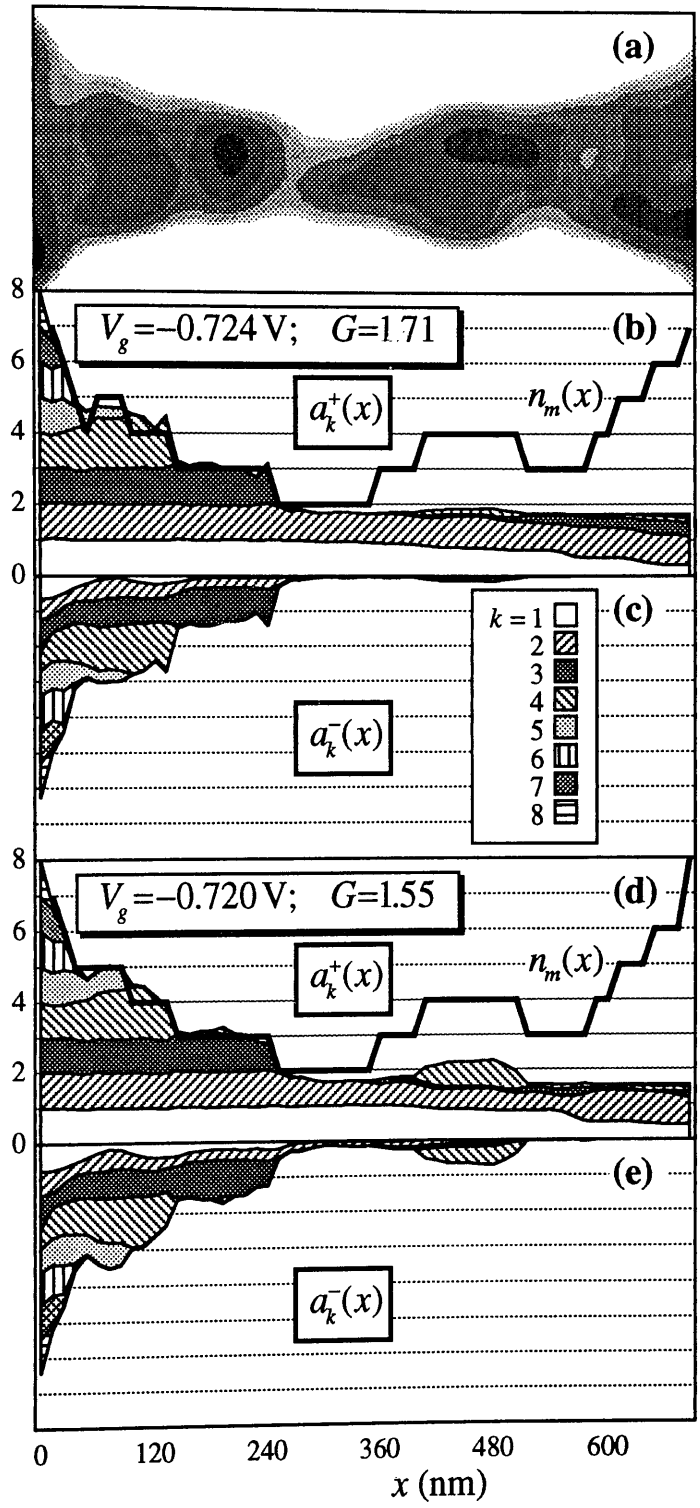

Figure 6.9 Modal analysis of a poorly quantized QPC

A change in gate voltage from $V_g = -0.724$ V to -0.720 V leads to a *decrease* in conductance from $G = 1.71$ to $G = 1.55$, whereas an *increase* would have been expected as the channel becomes wider and deeper. The electron density and available modes $n_m(x)$ in this QPC (Figures 6.9b and 6.9d) suggest that there is a resonant state in a 'bulge' for 400 nm <x < 500 nm, to the right of the narrowest region of the device. Only a very small fraction of flux passing through the constriction enters this resonance when $V_g = -0.724$ V. Here, the term *enters* means that electrons scatter into the modes that are only available as a result of the local widening of the channel. At the slightly shifted gate voltage of -0.720 V, a large flux appears in the bulge. Electrons are forward scattered from one of the conducting modes into the extra mode that propagates only within the bulge. They are reflected when this extra mode cuts off at the end of the bulge, and some are 'forward' scattered into the backward-going conducting modes (Figure 6.10). Flux that is not 'forward' scattered into the backward travelling conducting mode is then reflected when the mode cuts off. This reflected flux may then forward scatter to the forward travelling conducting mode or begin another circuit of the local extra mode. The net result is a three-step indirect back-scattering process which lowers the conductance.

The usual formula for mobility, based on the Born Approximation, gives very high values for electrons in narrow wires *(Sakaki 1980)*. This is because the slowly-varying nature of the random potential means that the matrix element for direct back-scattering is tiny. An important approximation in this formula is that successive scattering events are assumed to be independent, with no interference between them. This means that it cannot describe the three-step back-scattering process discussed above, and may seriously over-estimate the mobility. It is known from field theory *(Abrikosov 1976)* that the assumption of independent scattering events fails in one dimension, and we believe that the indirect back-scattering process provides a clear physical demonstration of this.

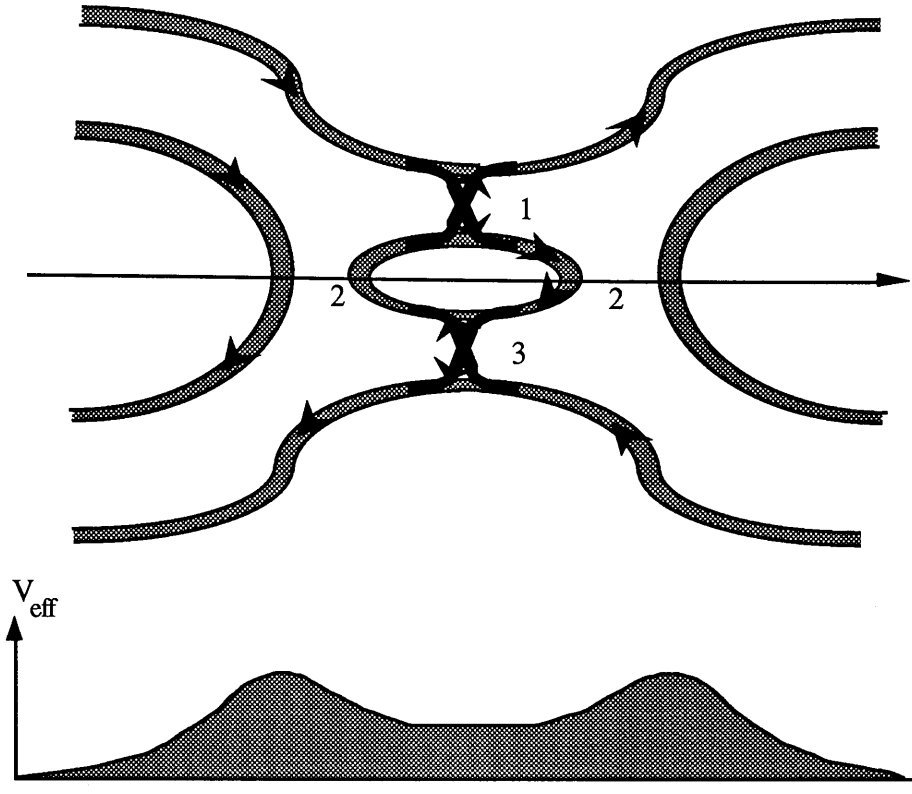

Figure 6.10 Schematic of three stage in-direct scattering process. 1) Electrons are forward scattered into (out of) the localized state. 2) Electrons in the localized state pass through cut-off and are reflected. 3) Electrons *forward* scatter out of the localized state into the backward travelling extended state.

Such resonances may explain the similar reduction in conductance observed in some experiments *(Timp 1989)* as the channel widens. It is important to distinguish this type of in-channel resonance from the flux build-up seen in mode three of Figure 6.6, which occurs when the mode is reflected at cut-off and is reminiscent of an Airy function solution to a turning point problem. This does not affect the conducting states, since this only represents a mode passing through cut-off and being reflected.

6.5 Analytical Scattering

Sakaki *(Sakaki 1980)* demonstrated that the scattering length of an electron travelling along a one-dimensional electron waveguide was enhanced over the scattering lengths in two- or three-dimensional systems, subject to the same scattering mechanisms. In the numerical calculations Sakaki used a single ionized impurity and determined the scattering rates from the Born Approximation. However, the basis of this enhancement can be intuitively understood with reference to Figure 6.11.

Figure 6.11a is a k-space representation of a purely one-dimensional electron waveguide. The only available scattering mechanism available to the electrons travelling forward, represented by vector $\mathbf{k}_{f1}$, is to undergo total reflection to state $\mathbf{k}_{r1}$. This reflection process requires a large change in momentum, Δk, which will not be allowed when the scattering potential is slowly varying. Figure 6.11b shows a system where the electron's energy has freed it from the confines of a purely one-dimensional system. Instead, the electron is in a quasi-one-dimensional system where it can scatter into other modes rather than undergo complete reflection in the same mode. Of the additional scattering mechanisms that are available to the electrons in this quasi-one-dimensional space, scattering into $\mathbf{k}_{f2}$ would be favoured due to the small change in momentum, Δk. However, the freedom of this forward, low angle, scattering is considerably restricted from that of a purely two-dimensional system, where there would be no quantization of allowed scattering angle. Therefore, one can expect that the scattering length in a quasi-one-dimensional system is enhanced over that of a truly two-dimensional system. Unfortunately, this picture is inconsistent with the results illustrated in Figure 6.9, where there is a considerable amount of backscattering in a channel of length 0.6 μm, which is less than the transport length of a 2DEG.

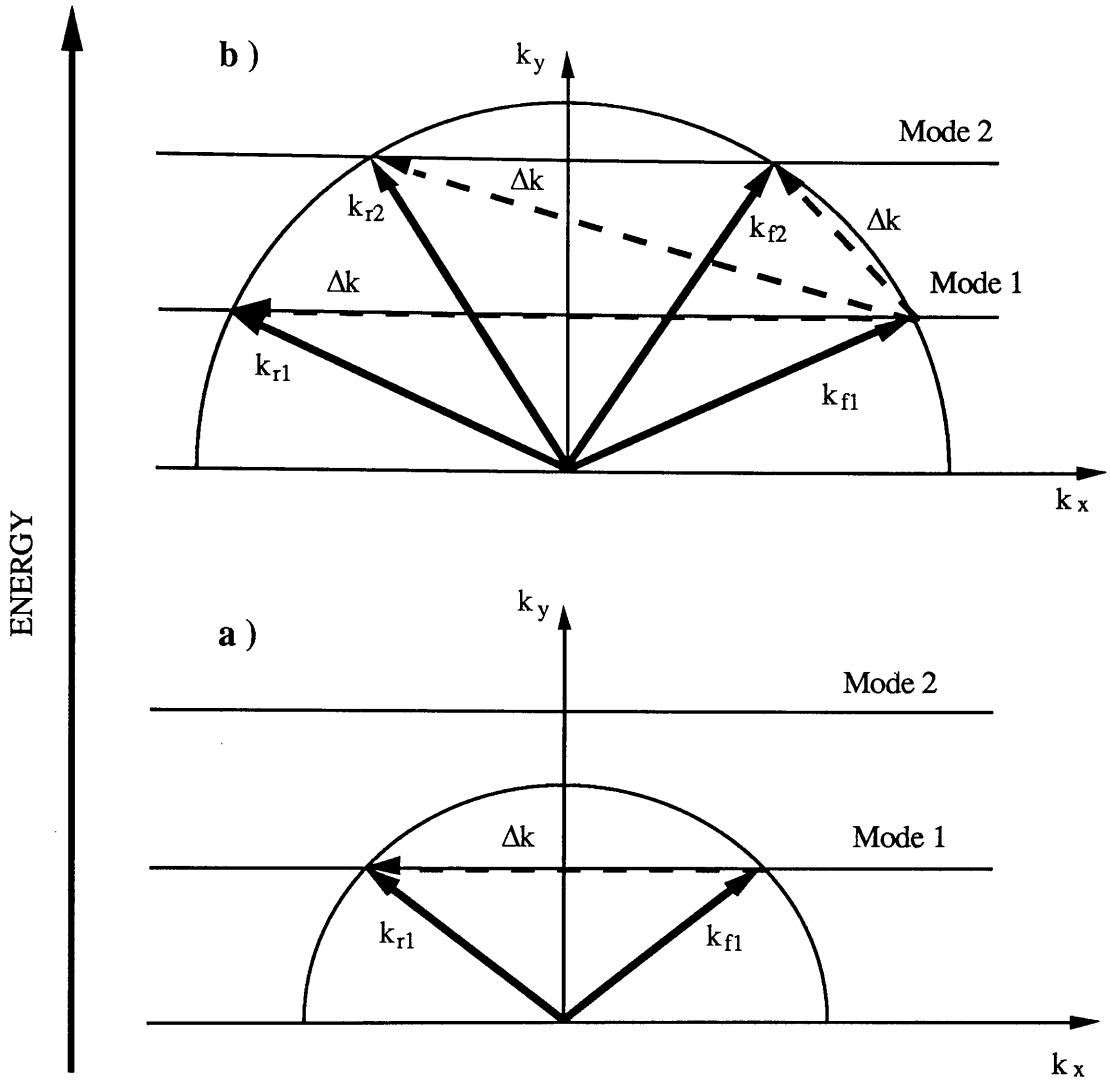

Figure 6.11 Schematic of scattering processes available to electrons travelling in the lowest forward mode as the Fermi energy is increased. a) The lowest mode is the only propagating mode available and therefore direct backscattering is the only possible scattering process. b) The increased Fermi energy has made the second mode available, thus increasing the scattering processes.

To investigate further we consider a long uniform electron waveguide and calculate the scattering caused by a weak random potential using perturbation theory. This is the routine method used to calculate two- and three- dimensional mobilities and has been more recently used by Glazman and Jonson *(Glazman 1991)*, also in the context of the electron waveguide. The modes of the system are defined by $\phi_n(y)\exp(\pm i\, k_n x)$ where $\phi_n(y)$ represents the various transverse modes which can be travelling forward, $\exp(+i\, k_n x)$, or backward, $\exp(-i\, k_n x)$ along the waveguide.

The propagation constant, k_n, is then defined as

$$k_n = \sqrt{\frac{2m}{\hbar^2}(E_{tot} - \varepsilon_n)} \tag{6.5}$$

and ε_n is the transverse energy of the mode. The scattering rate of each of the various scattering processes was determined using Fermi's Golden Rule

$$\frac{1}{\tau_{fi}} = \frac{2\pi}{\hbar} N(E_f)|V_{fi}|^2 \tag{6.6}$$

where $1/\tau_{fi}$ is the scattering rate for the transition from state *i* to state *f*. The scattering process is considered to be elastic, so that the energy of the initial state i equals that of the final state f, $E_f = E_i$, and V_{fi} is the matrix element given by

$$V_{fi} = \left(\frac{1}{L_x}\right)\iint dx\,dy\left[\phi_f^*(y)\exp(-i\,k_f x)\right]V(x,y)\left[\phi_i(y)\exp(i\,k_i x)\right] \tag{6.7}$$

$N(E_f)$ is the density of final states, which in this case is equal to one quarter of the usual one-dimensional density of states. This is because spin is preserved, and each scattering process considers only those electrons travelling in a single direction in the final state.

To produce an estimate of the screened potential seen by the electrons in the constriction, it was necessary to average over the out-of-plane ionized donors. After averaging over the ionized donors, the matrix element becomes *(Davies 1991)*

$$N_{imp}\int_{-\infty}^{\infty}\frac{dq}{2\pi}|\overline{V}(k_f - k_i, q)|^2\left|\int_{-\infty}^{\infty}dy\exp(iqy)\phi_f^*(y)\phi_i(y)\right|^2 \tag{6.8}$$

where N_{imp} is the areal density of impurities (m^{-2}).

The Thomas-Fermi approximation produces screening of an out-of-plane ionized donor by a 2DEG of

$$\overline{V}(q) = \left(\frac{e^2}{4\pi\varepsilon\varepsilon_0}\right)\frac{2\pi}{|q|+q_{TF}}\exp(-|z_0\,q|) \tag{6.9}$$

where z_0 is the distance from the ionized donors to the plane of the electrons and q_{TF} is the Thomas-Fermi wavevector.

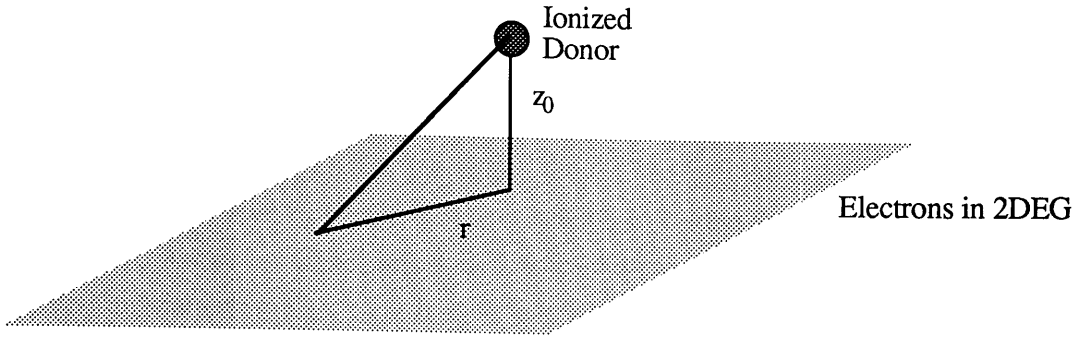

Figure 6.12 Distances in screening calculation

It was shown in Section 6.3 that, apart for an energy offset, a parabola is a good analytical approximation to the transverse potential in the electron waveguide. The Hermite eigenfunctions have therefore been used in this analytical calculation. The energy offset discussed in Section 6.3 will not have an impact, because all scattering processes are dependent upon the current mode of occupancy and the relative energies of all other modes.

Having determined the rates of all possible scattering processes using Equation 6.6, the total scattering rate was determined using Matthiessen's Rule, that is

$$\frac{1}{\tau_1} = \frac{1}{\tau_{11}} + \frac{1}{\tau_{21}} + \frac{1}{\tau_{31}} + \ldots \tag{6.8}$$

where $\frac{1}{\tau_1}$ is the overall scattering rate out of forward travelling mode 1, having taken into account all the scattering processes. This includes both back-scattering in the same mode, and also forward- and back-scattering in all other modes that are available in terms of energy. The inverse of this total scattering rate was then multiplied by the electron velocity to give an estimate of the scattering length.

Figure 6.13 shows the analytical results of the scattering rates and associated scattering lengths for an impurity density of 2.5×10^{16} m^{-2} and a parabolic mode spacing of 1 meV. This impurity density is consistent with that used to determine the realistic potential studied in Section 6.4. The energy spacing is also a reasonable approximation for the first 100 nm of this well-quantized device, but is seen from Figure 6.4 to increase to approximately 2 meV as the channel narrows. In calculating the scattering length, the usual factor of $(1-\cos\theta)$, where θ is measured relative to the forward direction and is used to weight the effect of the scattering on the mobility, was not used.

The discontinuities in Figure 6.13 correspond to the singularities in the density of states as each mode becomes available. With the electrons originating in the lowest, only conducting, mode, the scattering length is seen to increase from a low energy value of $\approx$10 μm as the electron energy increases. This is because the only available scattering process, as illustrated in Figure 6.11a, is reflection. As the Fermi energy increases, the necessary change in wavevector increases, with a corresponding reduction in the reflection scattering rate, S_{r1}. Just before the second mode becomes available, the scattering length is 100 μm. With the increase of the Fermi energy, the second mode becomes available and the scattering length falls drastically. This fall in scattering length results from an increase in the number and efficiency of the scattering processes. Of these scattering mechanisms, the forward scattering into mode two, S_{f2} of Figure 6.13b, dominates as a result of the reduced change in wavevector. The back-scattering rate into mode 2, S_{r2}, is seen to be of much the same efficiency as that of mode 1, and both of these back-scattering rates are several orders of magnitude down on the principal forward scattering rate. However, it must be noted that it is not purely the change in wavevector that determines the scattering rate. The backward scattering rate into mode two, S_{r2}, is lower than that of mode one, S_{r1}, despite the fact that the scattering process into mode two has a smaller wavevector change than that associated with mode one. This is because the transverse component of the overlap matrix must also be included in the calculation of the scattering rates. The predominance of forward scattering in this structure can be gauged from a comparison of the scattering lengths. The scattering length associated with all forward and backward scattering processes available is about 100 nm, whereas that purely based on back-scattering rates reached 100 μm by the time the first forward scattering process became available. Following the continual fall of the backward scattering rates in Figure 6.13c, this length of 100 μm would increase significantly as the energy was increased. This highlights the predominantly forward nature of the scattering in a QPC. Roughly there are two distinguishable rates: *(i)* a lifetime rate which determines the length of time spent in the original mode. This is dependent on all scattering processes, but dominated by forward scattering and *(ii)* a rate analogous to the transport rate, which is dependent on the back-scattering processes and strongly affects the conductance.

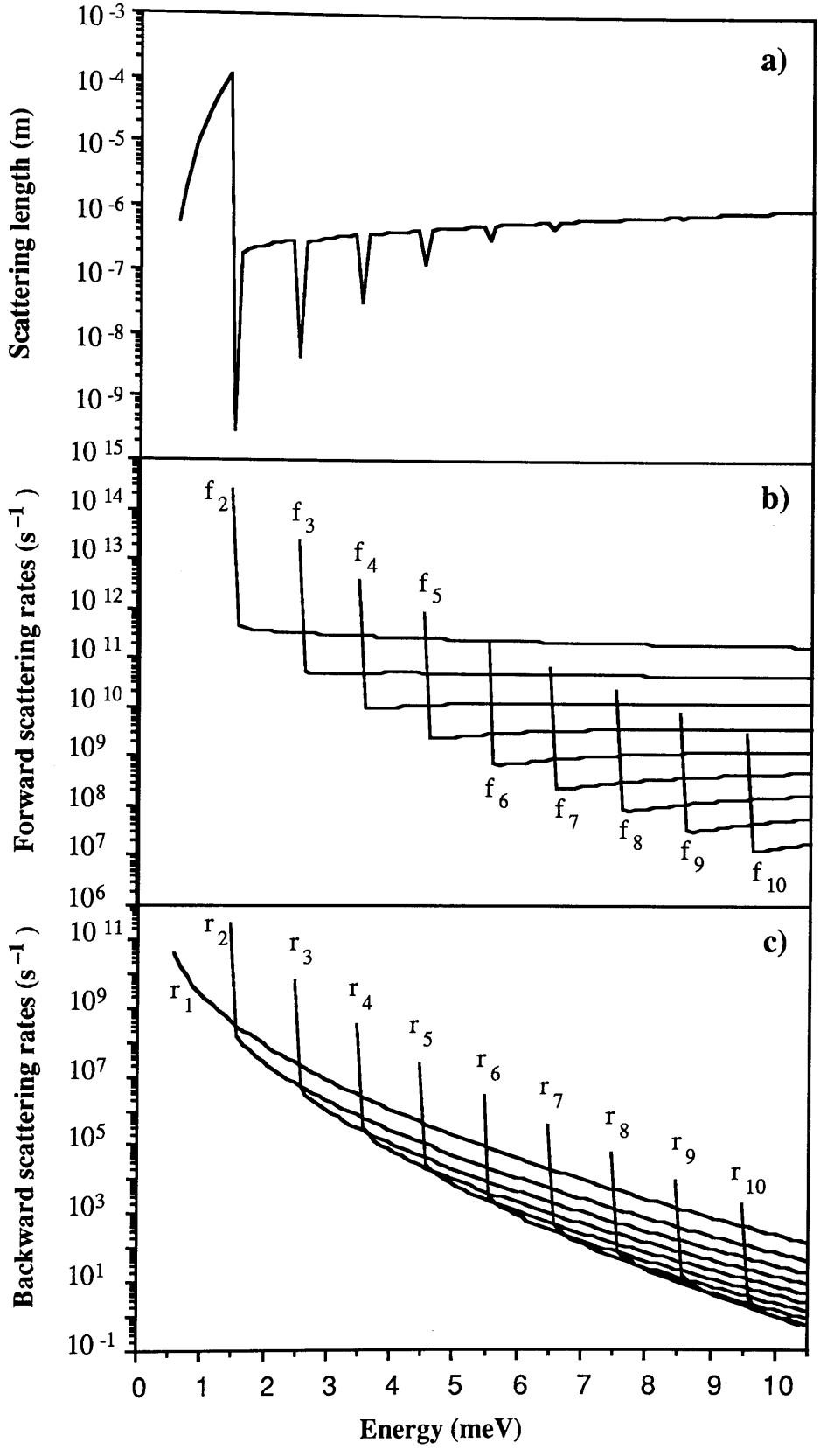

Figure 6.13 Analytical scattering rates with the input flux in mode one ($N=2.5\times10^{16}$ m^{-2}, $\Delta E=1$ meV)

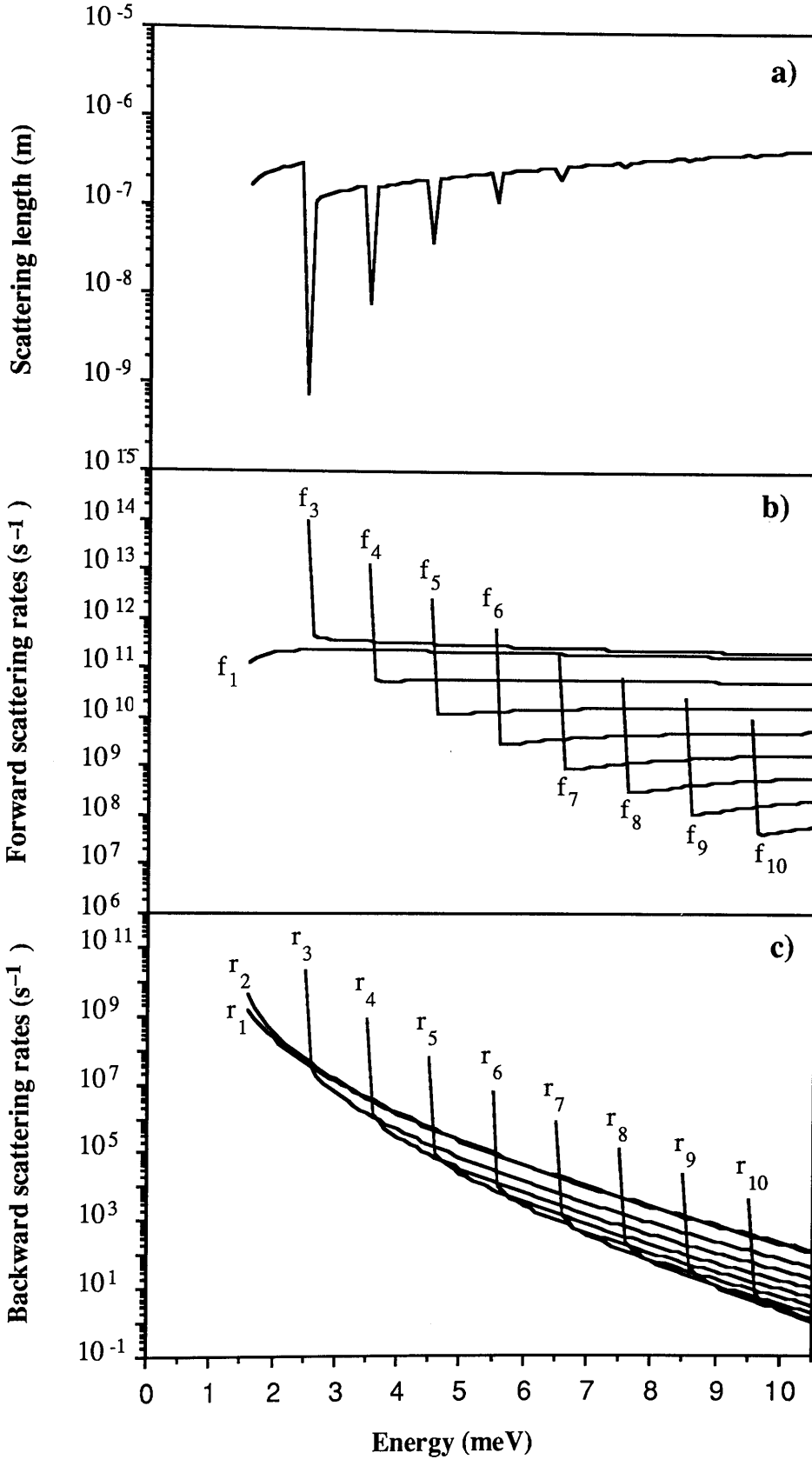

Figure 6.14 Analytical scattering rates with the input flux in mode two ($N=2.5\times10^{16}$ m^{-2}, $\Delta E=1$ meV)

As the Fermi energy increases further, more propagating modes become available but, with the exception of the singularity when the mode first becomes available, they have little impact on the overall scattering length, which is dominated by the forward scattering mechanism 1→2.

Overall, the scattering length for electrons incident in the lowest mode in this calculation is of the order of 100 nm. This is broadly in line with the electron scattering in the modal analysis of the realistic potential in Figure 6.6f, where it is seen that most of the electrons originating in the lowest mode have been scattered out within 120 nm. Furthermore, Figure 6.6f also shows that the initial and principal scattering process in the modal calculation is forward scattering into the second mode. This is also in agreement with the findings of this calculation.

In Figure 6.14, the results of the analytical calculation are shown for electrons input in the second mode, all other parameters remaining constant. These results are similar to those for electrons that enter in the first mode. The principal difference is that for electrons input in the second mode, both modes one and three act in the same way as mode two did for electrons input in the lowest mode. The scattering rates for electrons to forward-scatter from mode two to modes one and three are therefore comparable to each other. In both Figures 6.13 and 6.14 it is seen that the principal scattering mechanisms are with modes which would be expected to be excluded on the grounds of parity. However, Equation 6.8 shows that this problem with parity is accounted for by the Fourier transform.

6.6 Contacts

In this and the previous chapters, the transport in a QPC has been studied using both ideal leads and 2DEG contact regions. It has been left to this section to provide a justification for the earlier claims that a change in the contacts does not significantly alter the system under investigation.

6.6.1 'Ideal' Lead Contacts

Ideal leads have become a useful mathematical tool in the study of mesoscopic systems for several reasons. In this study they have allowed the identification of the incoming flux and the subsequent detailed investigation of the transport that this information enables. In other studies, the mathematical methods employed have necessitated the use of ideal leads as approximations to 2DEG contacts.

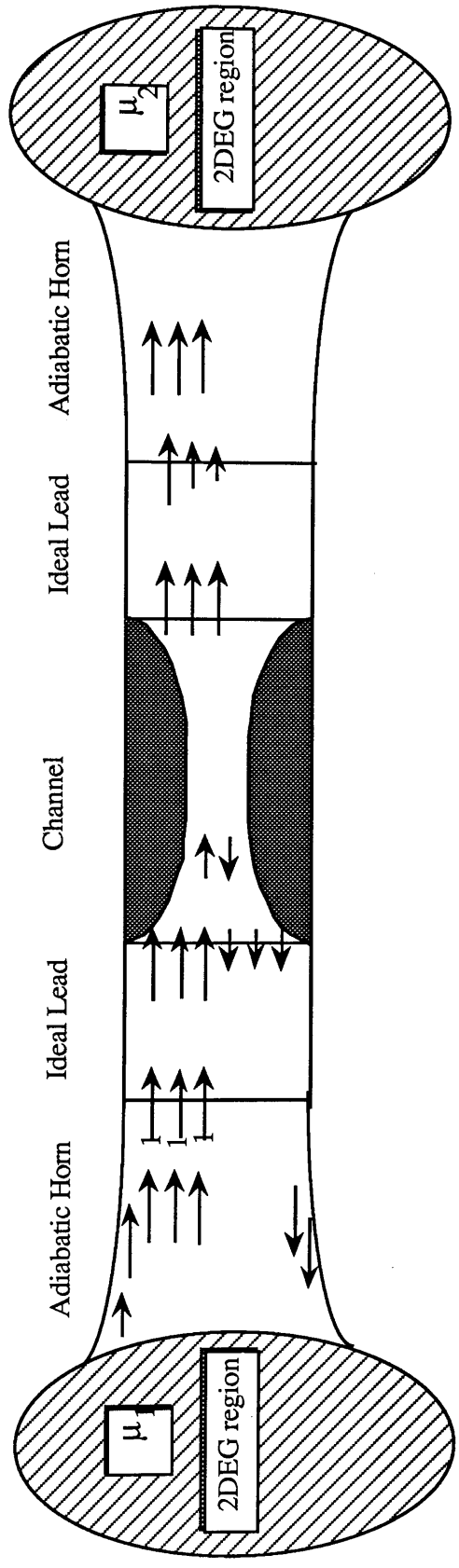

Figure 6.15 Schematic of a QPC connected to ideal leads

Figure 6.15 illustrates the local scattering processes of the net flux through the system. As described in Section 5.3.2, the ideal lead represents the final region of an adiabatic horn attached to the 2DEG. As the infinite number of one-dimensional channels travel down the adiabatic horn from the 2DEG, modes pass through cut-off and are reflected. Eventually only a finite number of these forward travelling fully occupied modes pass into the ideal lead. In applying ideal leads to a QPC system, the interface with the 2DEG has therefore not been ignored. Instead the scattering has been assumed to take place in a controlled manner that leaves all available modes fully occupied and each backward travelling state matched to those in the channel.

6.5.2 2DEG Contacts

The 2DEG contact system is simpler than that of ideal leads. In the 2DEG system, the full occupancy of each available mode at the start of the constriction is not guaranteed. Instead, the occupancy of each mode for the entire system is found by globally matching the 2DEG contacts to the QPC. This can produce poor matching and consequent low occupancy of some of the available modes.

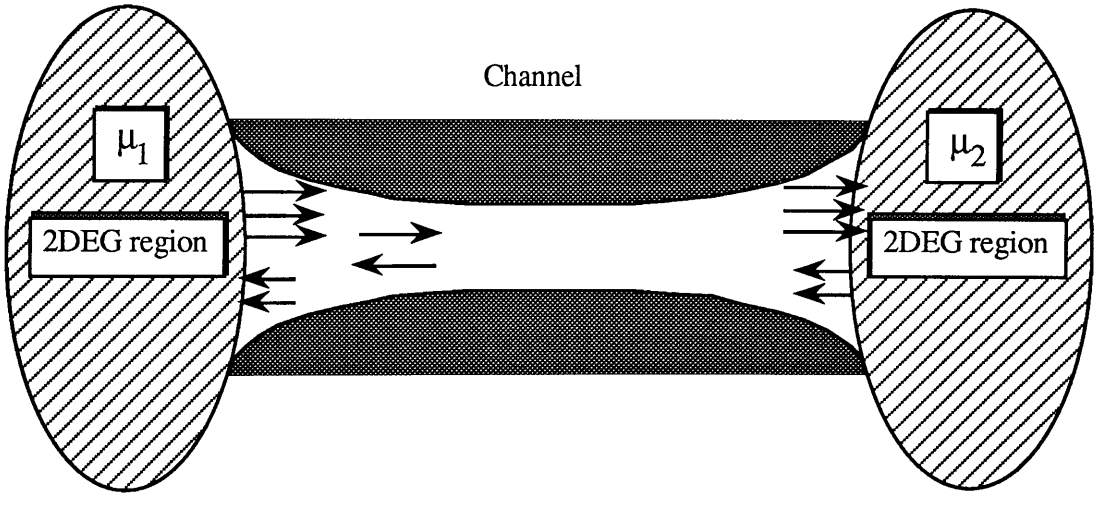

Figure 6.16 Schematic of a QPC connected to 2DEG contacts

In Chapter Five the additional scattering introduced by 2DEG contacts attached to the end of the channel was studied. Provided that the channel had widened sufficiently from its narrowest section, additional interface scattering was found to be negligible.

A more significant difference between ideal leads and 2DEG contacts is the initial coupling of the flux into the constriction. Figure 6.17 shows the 2DEG contact modal occupancy of the realistic QPC on the G = 1 plateau, as in Section 6.3. The occupancies represent the total modal occupancies, irrespective of the origin of the flux.

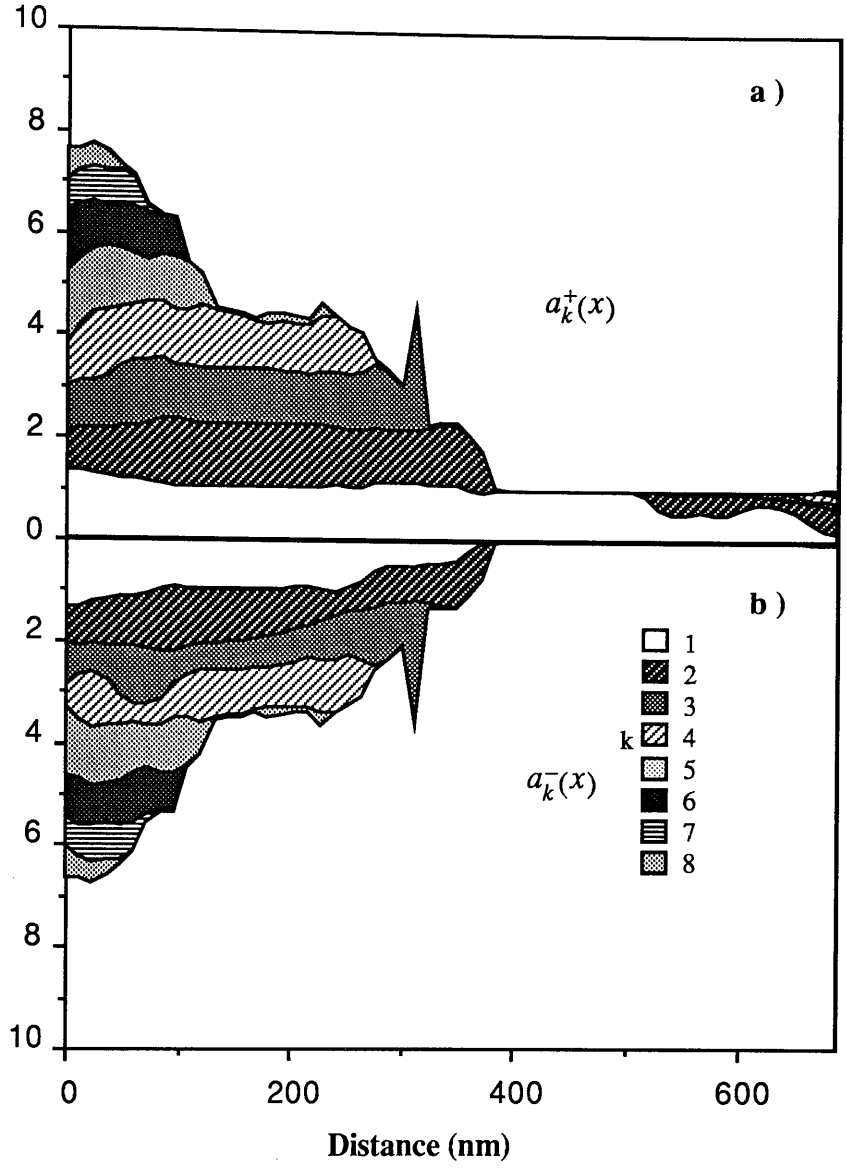

Figure 6.17 Transport through a realistic potential connected to 2DEG contacts

Where the occupancy of a mode at the start of a constriction is greater than unity, it is not possible to obtain a measure of the coupling efficiency. This is because the coupling has been obscured by resonances, as described in Section 5.5. However, poor coupling is evident where the occupancy at the entrance to the constriction is less than unity. This is the case for modes two to four in Figure 6.17. If transport were adiabatic in this system, this poor coupling would not have an effect on the G=1 plateau. However it has been shown in Section 6.3 that transport is far from adiabatic. In Figure 6.6f it can be seen that the majority of the flux present in the lowest mode, as it passes through the critical narrowest region of the channel, originated from modes three and four at the start of the constriction. With these modes being less than perfectly coupled when 2DEG

contacts are used, the calculated conductance is below that determined when ideal leads are used. This small difference in the results of the two systems can be seen by comparing the G=1 plateau in Figure 6.5 with the overall conductance in Figure 6.6.

The absence of adiabatic transport in the channel eliminates the requirement that good quantization be dependent on the coupling of a specific mode. Instead intermode scattering introduces a more general requirement of good overall mode coupling. Perfect quantization may not result from this requirement. However, a dependence on overall coupling rather than specific mode coupling introduces another element of robustness into the processes that allows an experimental observation of quantized conductance.

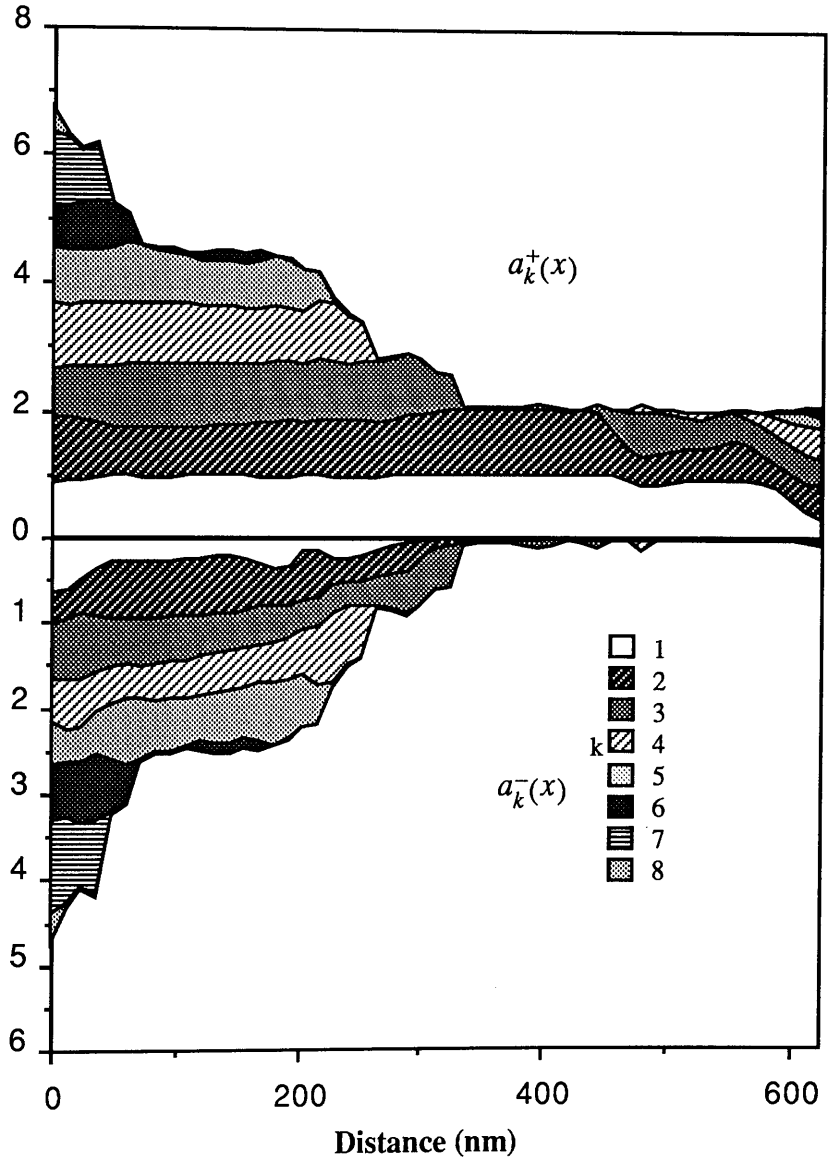

Figure 6.18 Modal analysis of a G=2 QPC connected to 2DEG contacts

This robustness of quantized conductance to poor mode coupling is more clearly illustrated in Figure 6.18, which shows the calculated conductance for another realistic potential on the G=2 plateau. Despite less than perfect coupling of all incident modes, the overall quantization is maintained.

In Figure 6.19 the lowest conducting mode of the QPC shown in Figure 6.18 is analysed in more detail. Figure 6.19a shows the origins of the flux in this lowest mode throughout the structure. The perfect coupling of this lowest mode to the contact at the start of the constriction is a consequence of having to use ideal leads in this particular calculation (Section 6.3). This ideal coupling is a considerable improvement over the coupling of the lowest mode when connected to 2DEG contacts, shown in Figure 6.19c. However, despite this poor coupling of the lowest mode at the start of the channel, at the middle of the channel its occupancy has almost reached unity. In Figure 6.19b the normally perfect coupling factors of the ideal contacts have been adjusted to the magnitudes of the modal occupancies of the QPC connected to the 2DEG contacts at the start of the constriction (Figure 6.18). Despite the crudeness of this approximation to the coupling factors, the resulting analysis, shown in Figure 6.19b, closely resembles the actual 2DEG contact calculation shown in Figure 6.19c. As a result of intermode scattering, by the middle of the channel the occupancy of this lowest mode is made up of varying amounts of flux from many channels. Therefore, the occupancy of the lowest conducting modes is not simply dependent on the coupling of these modes to the contacts. Instead, these occupancies are the result of both the coupling of all modes to the 2DEG contacts and also complex intermode scattering processes which will ordinarily not be in equilibrium. However, forward scattering will in general be favoured, which will tend to fill up the lower conducting modes, regardless of their initial occupancies.

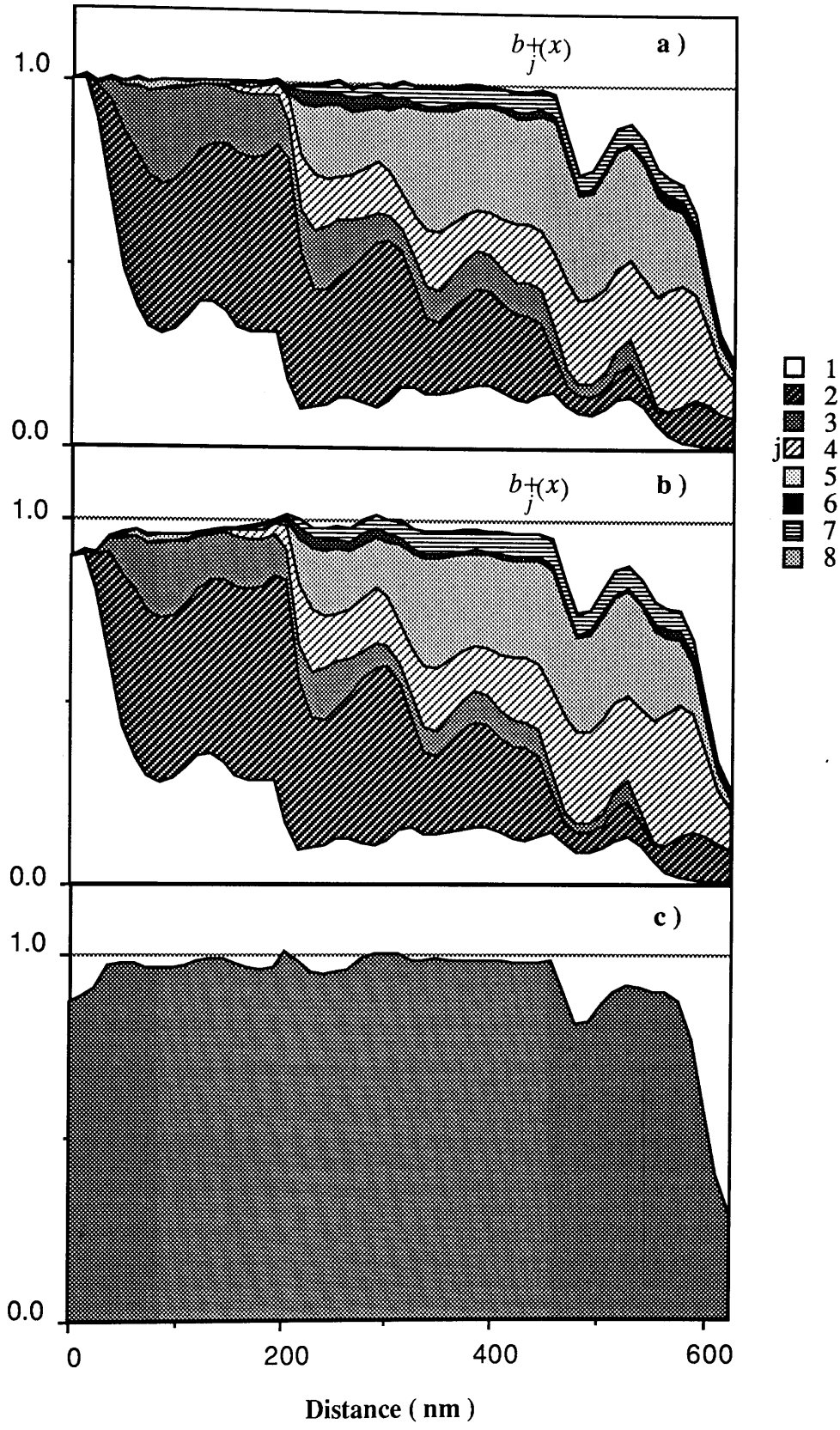

Figure 6.19 Lowest mode of a G=2 realistic QPC. a) shows the origins of the flux in the lowest mode connected to ideal leads. b) is similar to a), but with the modal coupling altered, in line with the coupling in Figure 6.18. c) shows the actual occupancy of the lowest mode of the same channel with 2DEG contacts

6.6 Summary

The chapter began with the introduction of the realistic potential model of Nixon *et al (Nixon 1991)*. In this model the influence of the ionized donors was not approximated by the usual average potential, but instead they were treated as individual potential sites. This treatment was found to have a significant influence on the self-consistent potential seen by the electrons in a 0.6 μm constriction. However, despite the random contribution of the ionized donors to the gate potential, the calculated conductance of a 0.6 μm QPC connected to 2DEG contacts was still found to contain plateaux, although these were seen to deteriorate as the conductance increased.

Next, the modal calculation developed in Chapter Four was used to analyse the transport on the G = 1 conductance plateau of the 0.6 μm realistic potential QPC. It showed that the adiabatic approximation fails badly, as the majority of electrons originally in the lowest mode had been scattered out within 100 nm. However, it was still possible to have well quantized conductance, subject to the less stringent condition of 'compensated' scattering.

In the modal analysis of a poorly quantized QPC, the primary cause of back-scattering which led to the degradation of the quantization was found to stem from a three-stage resonance scattering process. This mechanism provided, via a combination of forward scattering and cut-off, an efficient back-scattering process in an environment that strongly favoured forward scattering.

An analytical calculation, using the Born Approximation, was performed to provide further analysis of transport in realistic potentials. This calculation produced an unweighted scattering length of ≈ 100nm, which was comparable with the 'lifetime' of the electron flux originally in the lowest mode. This 'lifetime' was dominated by forward scattering processes, whose scattering rates were several orders of magnitude greater than those of the direct back-scattering processes. However, when back-scattering was examined in isolation, it was seen that at low energies the scattering length was of the order of 10 μm and would increase for higher Fermi energies. Unfortunately, this contradicts the physical observation and numerical investigation described in Section 6.4, where poor quantization was observed in a 0.6 μm QPC. This is at least an order of magnitude smaller than the *direct* back-scattering length determined by the Born Approximation. In the poorly quantized structure studied in Section 6.4, the quantization was degraded by a three-stage indirect back-scattering process. This cannot be accurately described by the Born Approximation, which assumes that successive scattering events are independent.

Therefore, if resonances are the dominant mechanism for backscattering, the use of the standard Born Approximation could severely overestimate the scattering length of an electron waveguide. In principle, the potential caused by a complex of remote ionized impurities in various configurations could be used in the Born Approximation to include the effect of multiple scattering at short length scales *(Baranger 1990)*.

Finally, a study was made of the influence of employing both ideal leads and 2DEG contacts in the conductance calculation. In the structures used for the comparison, small differences were observed in the calculated conductance. However, the principal finding was the tolerance to poor mode coupling brought about by the non-adiabatic nature of the transport in the QPC. Therefore, even in quite poorly coupled channels, a step structure may be observable in the conductance, although its accuracy may be poor.

Chapter Seven
Current and Future Work

7.1 Introduction

Up to this point, this thesis has described the techniques employed and the results obtained in the study of electron transport in QPC devices, and stands as a self-contained piece of work.

In this chapter, areas that represent a natural progression of the underlying methods used in this work are detailed, and their application to the study of electron transport in mesoscopic structures discussed along with preliminary findings.

7.2 Conformal Mapping

Drawing again an analogy with electromagnetic radiation, the technique of conformal mapping can be carried over into the electron waveguide regime *(Heiblum 1975)*. In the first instance, the Schrödinger Equation is written in the form of a standard scalar wave equation,

$$\sum_n \left[\left(\frac{\partial^2}{\partial x^2} + \frac{\partial^2}{\partial y^2} \right) + k^2(x,y) \right] A_n \psi_n(x) \phi_n(y) = 0 \qquad (7.1)$$

where $k^2(x,y) = \frac{2m}{\hbar^2}(E_{TOT} - V(x,y))$ and the wavefunction has been expanded in terms of the local normal transverse eigenstates $\psi_n(x)$ of the electron channel.

The basis of conformal transformations is to map a problem from one space, Z, onto another space, W, in which the problem is more easily solved. Solutions obtained in the co-ordinate system u,v of W space are related to those in x,y of Z space through the relationship,

$$W = u + iv = f(Z) = f(x + iy), \qquad (7.2)$$

where f is an analytical function. Following Heiblum, we transform Equation 7.1 from Z to W space with the aid of the Cauchy-Riemann relations, $\frac{\partial u}{\partial x} = \frac{\partial v}{\partial y}$, $\frac{\partial u}{\partial y} = -\frac{\partial v}{\partial x}$.

Then

$$\sum_n \left[\left(\frac{\partial^2}{\partial u^2} + \frac{\partial^2}{\partial v^2} \right) + \left(\frac{\partial Z}{\partial W} \right)^2 k^2(u,v) \right] A_n \psi_n(u) \phi_n(v) = 0 \tag{7.3}$$

where $\left(\frac{\partial Z}{\partial W} \right)^2 = \left(\frac{\partial u}{\partial x} \right)^2 + \left(\frac{\partial v}{\partial x} \right)^2$.

To illustrate this approach, we consider a curved section of waveguide in real, Z space. By applying the conformal transformation $W = R_c \ln\left(\frac{Z}{R_c}\right)$, the curved boundaries of the waveguide in Z space are transformed to straight ones in W space (refer to Figure 7.1).

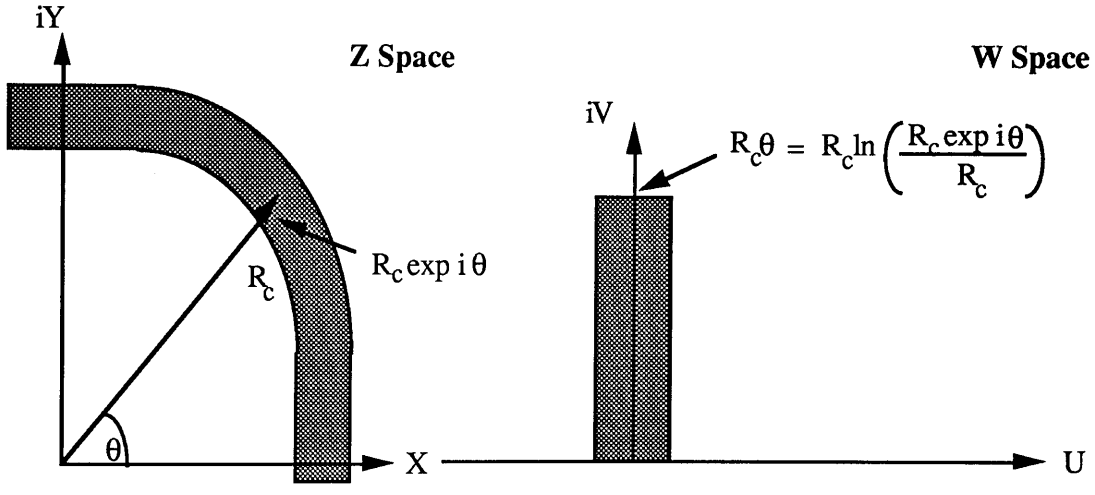

Figure 7.1 Conformal transformation of curved surface in Z space.

At the interface between a straight and curved section of guide in Z space, it is necessary to transform the curved section to W space and then match the wavefunction and its first derivative across the interface. Care must be taken in this matching process, since one must match the Z space eigenstates transformed to W space with the W space eigenstates of the transformed section of waveguide.

Preliminary results support those obtained by Sols *(Sols 1990)*, who found that the total transmission around a curved waveguide is practically unity, except very close to threshold. To obtain their results, Sols *et al* had used polar coordinates to allow separation of the variables for propagation around the curved section of the waveguide.

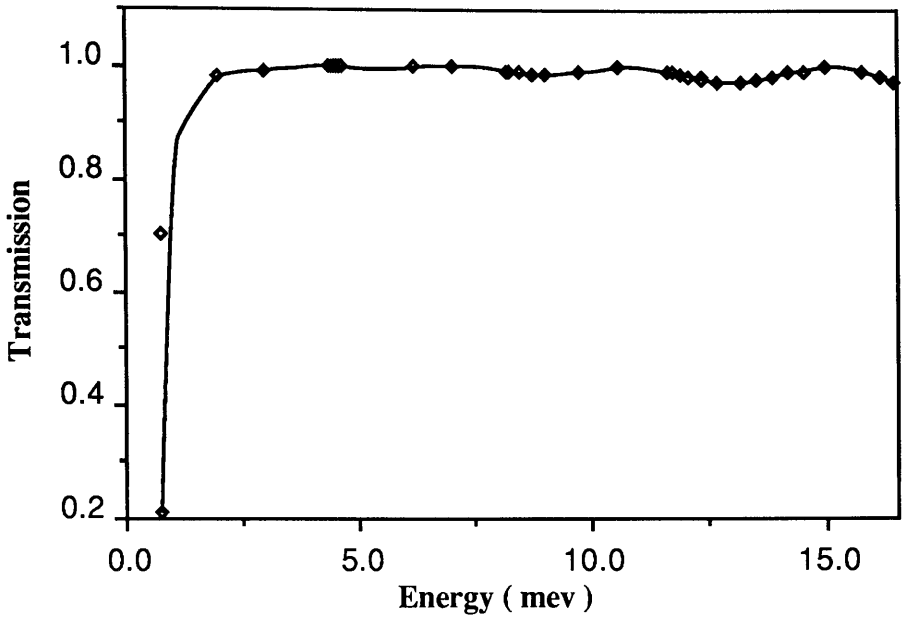

Figure 7.2 Transmission coefficient of an electron wave travelling around a 45° bend

The use of conformal mapping in other areas for many years has resulted in a wide range of transformations that may have potential for the electron waveguide environment, and it is surprising that to date no published work in this field has made mention of this type of approach.

7.3 Magnetic Fields

The use of magnetic fields in mesoscopic systems introduces many interesting concepts and effects. In this section a magnetic field is incorporated into an otherwise homogeneous waveguide to illustrate the application of magnetic fields into the coupled mode model.

With the addition of a magnetic field the Hamiltonian becomes

$$\mathbf{H} = \frac{1}{2m}(\mathbf{p} - e\mathbf{A})^2 + V(x,y) \qquad (7.4)$$

Generally, the magnetic field is applied perpendicularly to the plane of the electrons. If the electrons are in the x-y cartesian plane, the magnetic field will therefore be of the form $\mathbf{B} = B(0,0,1)$. There are many vector potentials, $\mathbf{A}$, that will produce this magnetic field via the relationship $\mathbf{B} = \text{curl } \mathbf{A}$. An example is $\mathbf{A} = B(0,x,0)$, which is known as the Landau gauge.

Using this form of the vector potential, the Hamiltonian becomes

$$\frac{-\hbar^2}{2m}\frac{\partial^2}{\partial x^2}-\frac{\hbar^2}{2m}\frac{\partial^2}{\partial y^2}+\frac{i\hbar}{m}Bex\frac{\partial}{\partial y}+\frac{(Bex)^2}{2m}+V(x,y) \tag{7.5}$$

In this instance we shall consider the effects of the magnetic field on a uniform section of electron waveguide. Furthermore, to demonstrate analytically the action of the magnetic field on the local normal modes of the guide, we shall assume that the guide can be approximated by a parabolic potential, as used in Chapter Four.

Following Chapter Four, the local transverse eigenstates of the parabolic potential are the Hermite polynomials

$$\phi_n(y) = 2^{-n/2}(n!)^{-1/2}\left(\frac{m\omega}{\hbar\pi}\right)^{1/4}\exp\left(\frac{-m\omega}{2h}y^2\right)H_n\left(\sqrt{\frac{m\omega}{\hbar}}y\right)$$

which satisfy the equation

$$\left(\frac{-\hbar^2}{2m}\frac{\partial^2}{\partial y^2}+V(y)\right)\phi_n(y)=\varepsilon_n\phi_n(y) \tag{7.6}$$

Applying the Hamiltonian to the general wavefunction $\sum_n \psi_n(x)\phi_n(y)$ and substituting Equation 7.6 produces

$$\sum_n \frac{-\hbar^2}{2m}\frac{\partial^2\psi_n}{\partial x^2}\phi_n(y)+\frac{i\hbar}{m}Bex\,\psi_n(x)\frac{\partial\phi_n(y)}{\partial y}+\frac{(Bex)^2}{2m}\psi_n(x)\phi_n(y)-(\varepsilon_{TOT}-\varepsilon_n)\psi_n(x)\phi_n(y)=0 \tag{7.7}$$

The next stage is to remove the summation and obtain the characteristic equation of each of the local modes $\psi_n(x)$. This is done by exploiting the orthogonality of each of the transverse eigenstate of the system by integrating Equation 7.7 by

$$\int_{-\infty}^{+\infty}\phi_\beta(y)dy$$

To perform this integration it is necessary to use some of the results obtained in Chapter Four. Equation 7.8 is the result of this integration, and illustrates the intermode coupling introduced by the magnetic field in an otherwise homogeneous system.

However, this scattering only couples with the modes immediately above, $\beta+1$, and below, $\beta-1$, the flux mode.

$$\frac{\partial^2\psi_\beta(x)}{\partial x^2} + i\frac{2m}{\hbar^2}Bex\omega\left[\left(\frac{\hbar\beta}{2m\omega}\right)^{1/2}\psi_{\beta-1}+\left(\frac{\hbar(\beta+1)}{2m\omega}\right)^{1/2}\psi_{\beta+1}\right]$$

$$- 2i\frac{Bex}{\hbar}\left(\frac{m\omega}{\hbar}\right)^{1/2}\left(2(\beta+1)\right)^{-1/2}\psi_{\beta+1}+\frac{2m}{\hbar^2}(\varepsilon_{TOT}-\varepsilon_n)\psi_\beta = 0 \qquad (7.8)$$

Equation 7.8 can be solved in an identical manner to that developed in Chapter Four. Figure 7.3 shows the results of this calculation for a 2 meV wavefunction travelling in a parabolic potential waveguide of length 500 nm characterized by $\hbar\omega = 3$ meV. The magnetic field of 0.6 T is present only over the central region of the system. The net flux at each point across the waveguide has been plotted at several points along its length. At each cross-section the total net flux was found to be the same, but there are clear differences in the spatial distribution of the flux throughout the waveguide. At the beginning and end there is no magnetic field present, and hence the forward and backward components of the flux are both evenly distributed about the centre of the guide. The resulting net flux plotted is therefore also symmetric about the centre of the waveguide. However, in the central regions in the presence of the magnetic field, there is a spatial separation between flux travelling forwards and backwards. This is broadly in line with general expectations of electron transport in magnetic fields, with electrons scattering along the boundaries of the waveguide in the presence of the perturbative magnetic field. If the electrons had been launched into an edge state of a wire under a continuous magnetic field, then back-scattering would not have been expected. Instead, the flux would have passed along one side of the waveguide and could have only back-scattered if there were sufficient perturbation to couple it to the back-scattering state that travels along the opposite side of the channel.

The application of magnetic fields is a rich area for future research. We have briefly touched on edge state transport, but there are other areas, including the Quantum Hall Effect in the weak coupled limit, in which the techniques developed here could be employed.

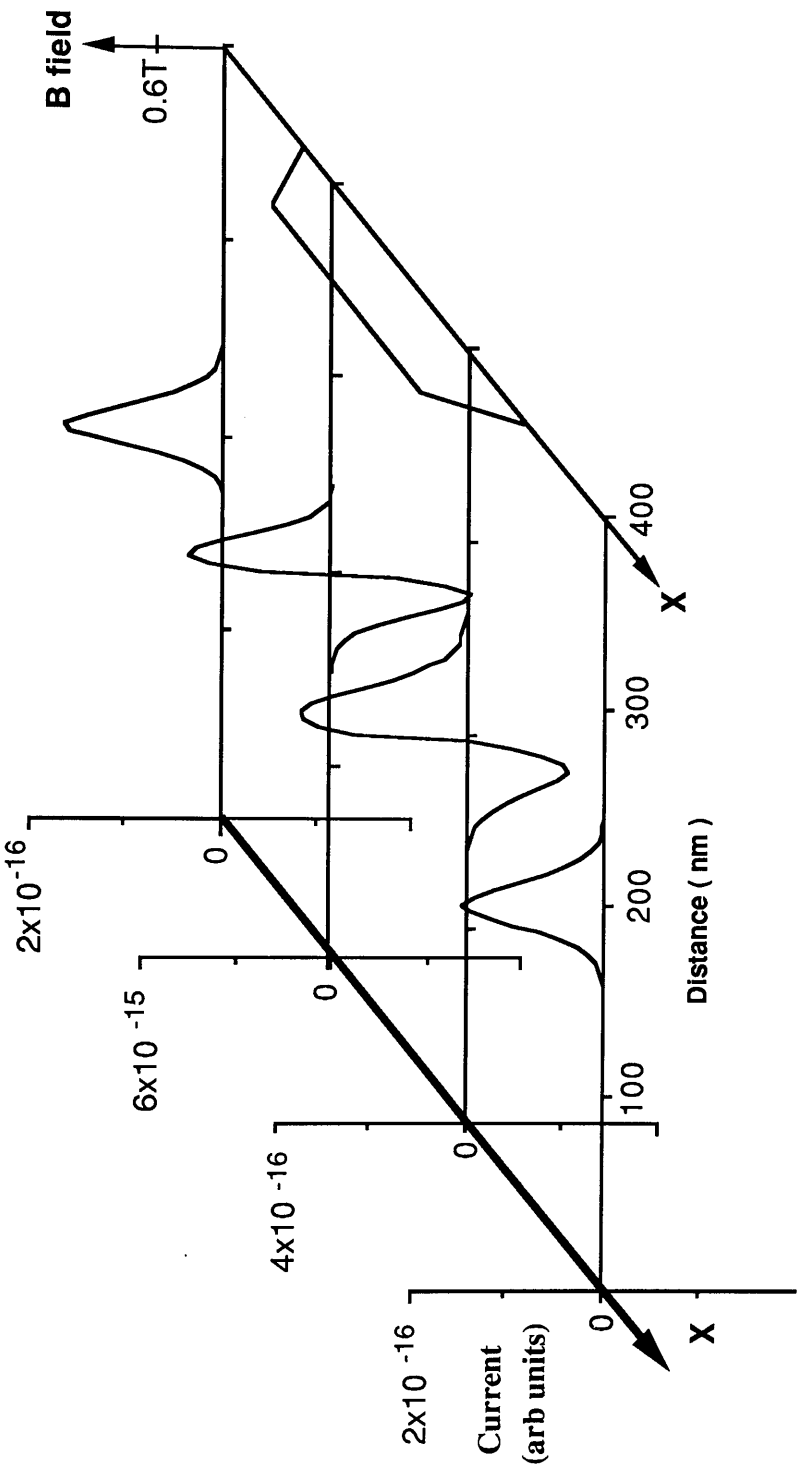

Figure 7.3 Net flux of an electron wavefunction confined in a parabolic waveguide section passing through a magnetic field. (Note that the flux axes are not drawn to scale).

7.4 Self-Consistent Potentials

Throughout this work no attempt has been made to include the effective potential of the electrons travelling through the device, since this is not of particular importance in the regimes of operation addressed in this work. However, in the limit where the realistic QPC is virtually cut-off and consists of a few weakly coupled 'puddles' of electrons, the self-consistent potential may prove significant. In this regime, the QPC is similar to a coulomb blockade device, in which the capacitance of each electron puddle is so small that a single electron can have a significant influence.

In standard one-dimensional calculations, the self-consistent potential is difficult to determine, because it is not possible to normalise the wave function. However, within the coupled mode approximation, it is possible to attach the QPC to 2DEG contacts. Using these 2DEG contacts it is possible to normalise the wave functions.

The electron density is given by

$$n_{2D} = 2\int_{-\infty}^{\infty}\frac{dk_y}{2\pi}\int_{-\infty}^{\infty}\frac{dk_x}{2\pi}f(k_x,k_y)|\psi(x,y)|^2 \qquad (7.9)$$

In the 2DEG, $\psi = 1 \times \exp(ik.r)$, so that $|\psi|^2 = 1$ and

$$n_{2D} = 2\int_{-\infty}^{\infty}\frac{dk_y}{2\pi}\int_{-\infty}^{\infty}\frac{dk_x}{2\pi}f(k_x,k_y) \qquad (7.10)$$

Approximating the Fermi function with the step function $f(k_x,k_y) = \theta\left(k_f - \left(k_x^2 + k_y^2\right)^{0.5}\right)$ gives

$$n_{2D} = 2\int_0^{k_f}\frac{2\pi k\,dk}{4\pi^2} = \frac{k_f^2}{2\pi} \qquad (7.11)$$

The Fermi wavevector is related to the energy via $E = \frac{\hbar^2 k_f^2}{2m}$.

This gives

$$n = \frac{mE}{\pi\hbar^2} \text{ and } \frac{dn}{dE} = \frac{m}{\pi\hbar^2}$$

which are consistent with the two-dimensional density of states.

7.5 Electron Collimation

In December 1987, Roukes *et al* *(Roukes 1987)* reported the first observation of the quenching of the low field Hall Effect in quasi-one-dimensional wires. Electron collimation is one of several theories put forward to explain this quenching of the low field Hall effect *(Roukes 1989)*. This theory was originally proposed by Beenakker *(Beenakker 1989)* and has also been successfully applied to the conductance of two QPCs in series *(van Houten 1990)*. However, the theory of collimation put forward by van Houten is based on a semi-classical adiabatic analysis, and it is unclear how such a picture can be reconciled to non-adiabatic electron transport in a QPC.

In this semi-classical analysis of electron collimation, the constriction channels the momentum of the electrons into the axial direction. It achieves this by a reduction in the transverse momentum and a corresponding increase in forward momentum as the constriction widens, with the electron remaining in the same mode. This leads to a collimation of the output beam, as θ gets smaller, assuming no diffraction effects at the interface with the 2DEG.

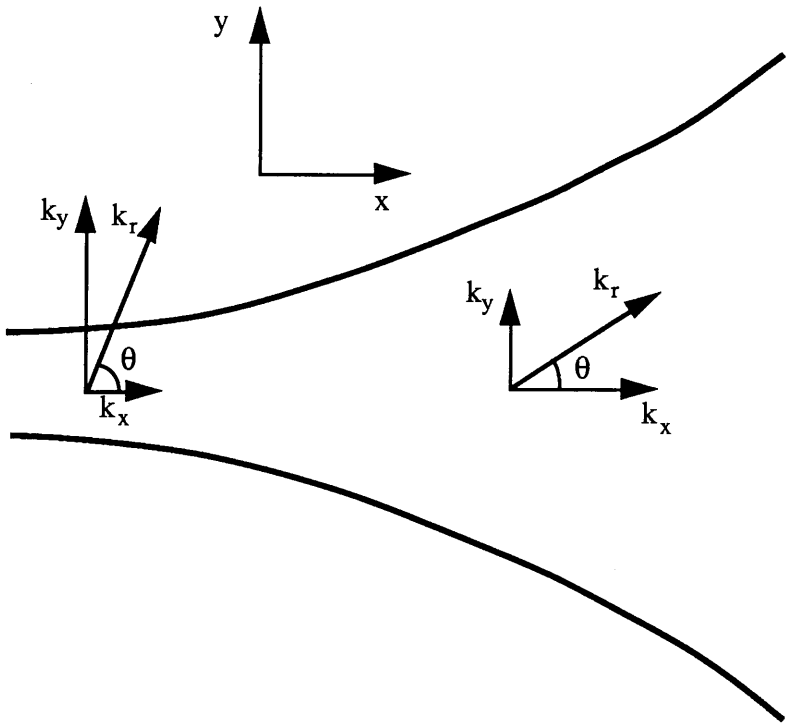

Figure 7.4 Schematic of adiabatic collimation of electrons emitted from a QPC.

As a first stage in obtaining a measure of the collimation, if any, from a non-adiabatic QPC we consider the channel on the G=1 plateau studied in Section 6.3.

The dependence of the conductance on the input angle can be obtained by substituting Equation 5.20 into Equation 5.22 to give

$$G = \frac{2m}{h^2} \int_{-\frac{\pi}{2}}^{\frac{\pi}{2}} d\theta \, k_f \langle \psi_\theta | J_x | \psi_\theta \rangle \tag{7.12}$$

where all terms are defined in Section 5.3.1.

The 2DEG contacts are identical and symmetric, with the exception of the potential difference. Therefore, by invoking reciprocity *(Schiff 1968)*, it can be seen that the dependence of the conductance on the input angle can also represent, with the potential difference reversed, the angular distribution of electrons leaving the QPC.

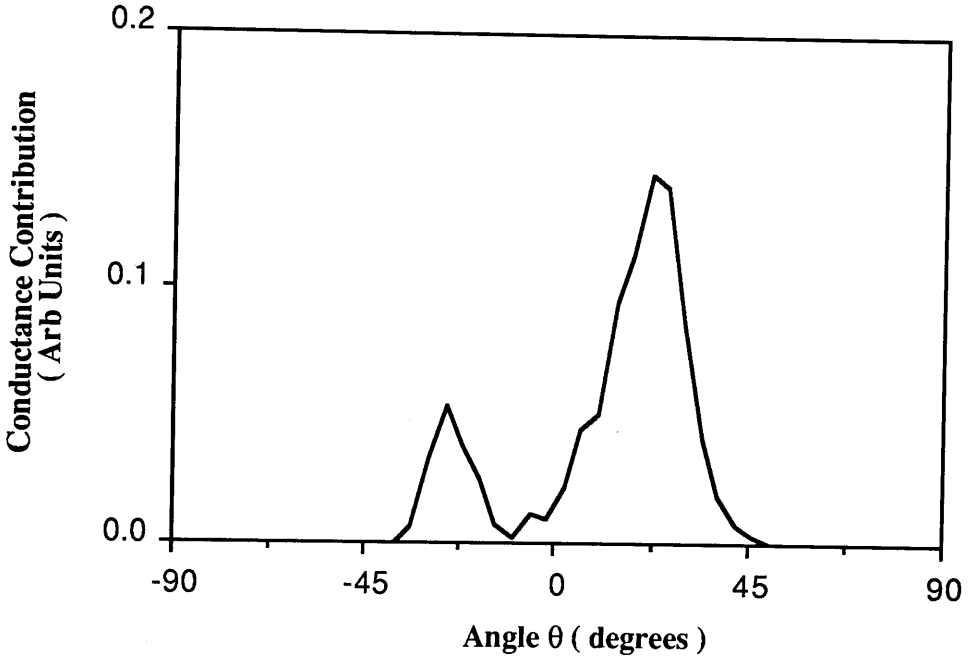

Figure 7.5 Angular contributions to the conductance in a non-adiabatic QPC on the G=1 plateau

The calculated angular contribution to the conductance of a realistic QPC on the G=1 plateau is plotted in Figure 7.5. Clearly some element of the random nature of the potential has been carried over into the asymmetry of the conductance as a function of incident angle. If this is viewed as an output beam, then electron collimation may be inferred, but this is not necessarily in the axial direction. However more work is required to provide a fuller picture of electron collimation in the non-adiabatic limit.

7.6 Summary

In this brief chapter, the basic method of modal analysis developed in the thesis has been shown to form the basis of a study in areas related to the basic transport through a QPC. The preliminary results obtained are encouraging and suggest that this could prove a fruitful area of future research.

Chapter Eight
Summary and Conclusions

In the first part of this thesis, the basic AlGaAs-GaAs heterostructure used to create the 2DEG system was introduced. It was seen that this area of semiconductor LDS has been dependent on recent developments in the areas of epitaxial growth and patterning techniques. Not only have advances in technology led to advances in conventional semiconductor devices but they have also made conceivable the possibility of new devices based on fundamental quantum phenomena. If continued improvements in conventional devices follow current trends, then we can expect to observe quantum effects as a secondary influence on the operation of conventional device structures. Therefore, a study of semiconductor LDS forms an integral part of the development of both conventional devices and a potential new class of quantum devices, as well as providing a test bed for semiconductor physics research.

The basic building block of any device is a section of connecting lead. When, in 1988, a short (0.2 μm) section of a 2DEG was confined to form a wire whose width was comparable with the Fermi wavelength, its conductance was found to be quantized. The system comprising the narrow channel and connecting contacts was termed a Quantum Point Contact (QPC). This conductance quantization had not been predicted, which is surprising when one considers the elegant simplicity of the processes responsible. Although conjecture, we would like to propose the following reasons for not predicting the quantization. It was not thought possible that :

i) the available modes in the channel would be exactly filled by electrons from the contact.

ii) a channel could be fabricated which was sufficiently smooth, on an electron wavelength scale, to allow adiabatic transport.

The original experimental observation and analysis appeared to support these assumptions. However, these findings were inconsistent with those of both early numerical models, which predicted that the quantization should have a resonant structure, and also experimental measurements of longer, 0.6 μm, channels, where quantization was found to be poor.

In Chapter Three, an initial time-dependent study of transport through a QPC was carried out, based on a Alternating Direction Implicit (ADI) expansion of the 2D Schrödinger Equation. This approach was not found to be suitable for a detailed study,

but provided a qualitative appreciation of the transport. In particular, it highlighted the complex nature of the scattering at the contact-channel interface and the modal nature of the transport in the channel.

A time-independent approach more suitable to a detailed study of the electron transport was developed in Chapter Four. Where the channel could be fully described analytically, it was possible to develop a Coupled Mode description of the transport inside the channel. It was necessary to solve this system of equations numerically. However, it proved very difficult to develop a integration procedure that could integrate stably through mode cut-off and carry evanescent modes in the calculation. After considerable effort, a stable approach was found, which was then developed for systems which could not be described analytically.

In Chapter Five, this Coupled Mode method was first applied to the uniform QPC connected to 2DEG contacts. The calculated conductance was found to have a significant oscillatory structure. These oscillations, first modelled by Kirczenow, were neither predicted by the original analytical analysis nor observed experimentally. A correction for non-zero temperature was applied to this oscillatory conductance, but this was found to be insufficient to explain the lack of any resonant structure observed experimentally. A modal analysis of this oscillatory conductance revealed an energy dependence in the coupling efficiency to the available modes inside the channel.

A more realistic self-consistent model of the gate potential was found to possess a tapered region connecting the narrowest section of the channel to the 2DEG contacts. The conductance of this potential structure was calculated by combining the general formalism of the independent vector propagation of Chapter Four with the 2DEG interface matching of Chapter Five. The conductance calculations revealed that the tapers vastly improved the coupling efficiency to the 2DEG contacts over a continuous energy range and led to the virtual elimination of oscillations even at 0 K. This provided clear evidence for the important role of the shape of the interface between the channel and the 2DEG contacts in the observation of quantized conductance. However, an analysis of the origins of the flux in the narrowest section of this well quantized QPC indicated that the transport was not totally adiabatic.

Chapter Six began with the introduction of the realistic potential model of Nixon *et al (Nixon 1991)*. In this model the influence of the ionized donors was not approximated by the usual average potential, but instead they were treated as individual, randomly distributed potential sites. This treatment was found to have a significant influence on the self-consistent potential seen by the electrons in a 0.6 μm constriction. However, despite the random contribution of the ionized donors to the gate potential, the

calculated conductance of a 0.6 μm QPC connected to 2DEG contacts was still found to contain plateaux, although these were seen to deteriorate as the conductance increased.

A detailed modal study of the transport on the G = 1 (in units of $2e^2/h$) conductance plateau of the 0.6 μm realistic potential QPC was made. It showed that the adiabatic approximation fails badly, as the majority of electrons originally in the lowest mode had been scattered out within 100 nm. However, it was still possible to have well quantized conductance, subject to the less stringent constraint of 'compensated' scattering in which the flux that foward scatters out of a mode is exactly balanced by flux that forward scatters into the same mode.

In the modal analysis of a poorly quantized QPC, the primary cause of back-scattering which led to the degradation of the quantization was found to stem from a three-stage indirect resonance scattering process. This mechanism provided, via a combination of forward scattering and cut-off, an efficient back-scattering process in an environment that strongly favoured forward scattering.

An analytical calculation, using the Born Approximation, was performed to provide further analysis of transport in realistic potentials. This calculation produced an unweighted scattering length of approximately 100 nm, which was comparable with the 'lifetime' of the electron flux originally in the lowest mode of the coupled mode calculation. The Born Approximation scattering length was dominated by forward scattering processes whose rates were several orders of magnitude greater than those of the direct back-scattering processes. Therefore, when back-scattering was examined in isolation, it was seen that at low energies the scattering length was of the order of 10 μm, and would increase further for higher Fermi energies. Unfortunately, this contradicts the physical observation and coupled mode calculation of a realistic potential, where poor quantization was observed in a 0.6 μm QPC. This is at least an order of magnitude smaller than the *direct* back-scattering length determined by the Born Approximation.

In the poorly quantized structure studied, the quantization was degraded by a three-stage indirect back-scattering process. This cannot be accurately described by the Born Approximation, which assumes that successive scattering events are independent. Therefore, if resonances are the dominant mechanism for back-scattering, the use of the standard Born Approximation could severely overestimate the scattering length of an electron waveguide. In principle, the potential caused by a complex of remote ionized impurities in various configurations could be used in the Born Approximation to include the effect of multiple scattering at short length scales *(Baranger 1990)*.

A study was made of the influence of employing both ideal leads and 2DEG contacts in the conductance calculation. In the structures used for the comparison, small differences were observed in the calculated conductance. However, the principal finding was the tolerance to poor mode coupling brought about by the non-adiabatic nature of the transport in the QPC. Therefore, even in quite poorly coupled channels, a step structure may be observable in the conductance, although its accuracy may be poor.

Finally, Chapter Seven gave a brief introduction to other areas of LDS in which the Coupled Mode model developed in this thesis could be applied. Preliminary findings indicate that this could prove a fruitful area of future research.

The principal findings of this thesis can therefore be summarized as:

i) The random potential in a QPC leads to rapid intermode scattering. The adiabatic approximation fails badly, but conductance can still be quantized through the less stringent conditions of 'compensated' scattering.

ii) The lack of adiabaticity in the transport can compensate for poor coupling of the channel modes to the contact regions. Through a process of forward intermode scattering, this non-adiabatic process can lead to the full occupancy of the lower conducting modes. This makes the conductance profile of the QPC less sensitive to the exact nature of the channel / interface geometry.

iii) An efficient resonant back-scattering process has been identified which cannot be described within the usual Born Approximation. If this represents the dominant back-scattering process in quasi-one-dimensional systems, then the mobilities calculated using the Born Approximation will be overstated.

Interestingly, these findings show that the assumptions originally applied to explain the observation of conductance are not required to obtain conductance quantization.

These findings imply that, in currently available LDS, the only means to obtain adiabatic transport is to have just one conducting mode available to the electrons throughout the length of the channel. However, it will still be necessary to have a tapered horn section to match the channel to the 2DEG contacts, in an effort to ensure the full occupancy of the single conducting mode.

Unfortunately, the fabrication of a monomode system will be frustrated by the potential of the ionized donor layer, which could either cut off the channel completely or else provide small sections in which more than one mode is available. In both instances

this could lead to back-scattering, which would degrade the transport and provide a different 'fingerprint' to each device. Such unique device characteristics would make the integration of several devices very difficult. Current research is in progress to attempt to reduce this problem through delta doping.

Further restrictions are placed on the fabrication of the channel when the operating temperature is considered. Current thinking suggests that it may be practical to operate semiconductor equipment at liquid nitrogen temperatures (77K). At this temperature $kT \approx 7$ meV. In order that the system remain monomode, the channel energy spacing must be several times this energy. Applying the 'particle in a box' approximation suggests that the channel width must be less than 50 nm.

In conclusion, there are significant engineering challenges to be overcome before quantum device structures can become a reality. In the meantime, however, these structures provide a fascinating basis for the study of semiconductor physics.

Appendix 1

This appendix details the modal coupling parameters of an parabolic electron waveguide described by an analytical function in $\psi^+ \psi^-$ space (refer to Equation 4.20).

$$M_{\beta\,\beta}^{\pm\pm} = \mp\frac{1}{2k_\beta}\frac{\partial k_\beta}{\partial x} \pm \frac{1}{2ik_\beta}\left(\frac{\partial\omega}{\partial x}\right)^2 \frac{\left(\beta^2+\beta+1\right)}{8\omega^2}$$

$$M_{\beta\,\beta}^{\pm\mp} = \pm\frac{1}{2k_\beta}\frac{\partial k_\beta}{\partial x} \mp \frac{1}{2ik_\beta}\left(\frac{\partial\omega}{\partial x}\right)^2 \frac{\left(\beta^2+\beta+1\right)}{8\omega^2}$$

$$M_{\beta\,\beta-2}^{+\pm} = \frac{\partial^2\omega}{\partial x^2}\frac{\left[\beta(\beta-1)\right]^{1/2}}{ik_\beta\ 8\omega} - \left(\frac{\partial\omega}{\partial x}\right)^2 \frac{\left[\beta(\beta-1)\right]^{1/2}}{8\omega^2\ ik_\beta} \pm \frac{k_{\beta-2}}{k_\beta}\frac{\left[\beta(\beta-1)\right]^{1/2}}{4\omega}\left(\frac{\partial\omega}{\partial x}\right)$$

$$M_{\beta\,\beta+2}^{+\pm} = -\frac{\partial^2\omega}{\partial x^2}\frac{\left[(\beta+1)(\beta+2)\right]^{1/2}}{ik_\beta\ 8\omega} + \left(\frac{\partial\omega}{\partial x}\right)^2 \frac{\left[(\beta+1)(\beta+2)\right]^{1/2}}{8\omega^2\ ik_\beta} \mp \frac{k_{\beta+2}}{k_\beta}\frac{\left[(\beta+1)(\beta+2)\right]^{1/2}}{4\omega}\left(\frac{\partial\omega}{\partial x}\right)$$

$$M_{\beta\,\beta-4}^{+\pm} = -\left(\frac{\partial\omega}{\partial x}\right)^2 \frac{\left[\beta(\beta-1)(\beta-2)(\beta-3)\right]^{1/2}}{32\omega^2\ ik_\beta}$$

$$M_{\beta\,\beta+4}^{+\pm} = -\left(\frac{\partial\omega}{\partial x}\right)^2 \frac{\left[(\beta+1)(\beta+2)(\beta+3)(\beta+4)\right]^{1/2}}{32\omega^2\ ik_\beta}$$

$$M_{j\,k}^{-\pm} = -M_{j\,k}^{+\pm}$$

Appendix 2

This appendix details the modal coupling parameters of an parabolic electron waveguide described by an analytical function in $\psi\Omega$ space (refer to Equation 4.26).

$$T_{\beta\,\beta}^{\Omega\,\psi} = -k_\beta{}^2 + \left(\frac{\partial\omega}{\partial x}\right)^2 \frac{\left(\beta^2+\beta+1\right)}{8\omega^2}$$

$$T_{\beta\,\beta-2}^{\Omega\,\psi} = \frac{\partial^2\omega}{\partial x^2}\frac{\left[\beta(\beta-1)\right]^{1/2}}{4\omega} - \left(\frac{\partial\omega}{\partial x}\right)^2 \frac{\left[\beta(\beta-1)\right]^{1/2}}{4\omega^2}$$

$$T_{\beta\,\beta+2}^{\Omega\,\psi} = -\frac{\partial^2\omega}{\partial x^2}\frac{\left[(\beta+1)(\beta+2)\right]^{1/2}}{4\omega} + \left(\frac{\partial\omega}{\partial x}\right)^2 \frac{\left[(\beta+1)(\beta+2)\right]^{1/2}}{4\omega^2}$$

$$T_{\beta\,\beta-4}^{\Omega\,\psi} = -\left(\frac{\partial\omega}{\partial x}\right)^2 \frac{\left[\beta(\beta-1)(\beta-2)(\beta-3)\right]^{1/2}}{16\omega^2}$$

$$T_{\beta\,\beta+4}^{\Omega\,\psi} = -\left(\frac{\partial\omega}{\partial x}\right)^2 \frac{\left[(\beta+1)(\beta+2)(\beta+3)(\beta+4)\right]^{1/2}}{16\omega^2}$$

$$T_{\beta\,\beta+2}^{\Omega\,\Omega} = -\frac{\partial\omega}{\partial x}\frac{\left[(\beta+1)(\beta+2)\right]^{1/2}}{2\omega}$$

$$T_{\beta\,\beta-2}^{\Omega\,\Omega} = \frac{\partial\omega}{\partial x}\frac{\left[\beta(\beta-1)\right]^{1/2}}{2\omega}$$

References

Abrikosov A.A., Ryzhkin I.A., *JETP* **44** (1976) 630

Ansboro A.P. Ph.D Thesis University of Glasgow 1989

Arfken G. *Mathematical Methods for Physicists* (Academic Press 1970)

Bagwell P.F., Orlando T.P. *Phys. Rev.* **B40** (1989) 1456

Baranger H. U. Private communication (1990)

Barker J.R., Pepin J., Finch M., Laughton M.J. *Solid State Electronics* **32** (1989) 1155

Beenakker C.W.J., van Houten H., *Phys Rev* **B39** (1989) 10445

Büttiker M. *Phys Rev* **B41** (1990) 7906

Büttiker M., Imry Y., Landauer R., Pinhas S. *Phys. Rev.* **B31** (1985) 6207

Collins S. Ph.D Thesis University of Warwick 1986

Datta S. *Superlattices and Microstructures* **6** (1989) 83

Davies J.H. *Postgraduate Lecture Series* (University of Glasgow, 1987, unpublished)

Davies J.H., Timp G. *preprint* (1991)

Efros A.L., Pikus F.G., Saamsonide G.G. *Phys Rev* **B41** (1990) 8295

Eisberg R.M. *Fundamentals of Modern Physics* (John Wiley & Sons, New York, 1961)

Evans R.B. *Wave Motion* **8** (1986) 321

Fesbach H., Villars F. *Rev Mod Phys* **30** (1958) 24

Finch M. Ph.D. Thesis, University of Glasgow 1989

Fisher D.S., Lee P.A. *Phys Rev* **B23** (1981) 6851

Foxon C.T., Harris J.J., Hilton D., Hewitt J., Roberts C. *Semicond. Sci. Technol* **4** (1989) 582.

Glazman L.I., Jonson M. *Phys Rev* **B44** (1991) 3810

Glazman L.I., Lesovik D.E., Khmel'nitskii D.E., Shekhter R.I. *JETP Lett* **48** (1988) 238

Goldberg A., Schey H.M., Schwartz J.L., *Am J Phys* **35** (1967) 177

Hartstein A. in *Physics and Fabrication of Microstructures and Microdevices,* edited by Kelly M.J., Weisbuch (Springer, Berlin 1986)

Heiblum M., Harris J.H. *IEEE J. Quantum Electron.* **QE11** (1975) 75

van Houten H., Beenakker C.W.J., van Wees B.J., in *Semiconductors and Semimetals,* edited by M.A. Reed (Academic Press, New York, 1990)

Imry Y. in *Directions in Condensed Matter Physics,* edited by Grinstein G., Mazenko G. (Singapore, World Scientific)

Jaros M. *Physics and Applications of Semiconductor Microstructures* (Clarendon Press, Oxford, 1989)

Keyes R.W. *IBM J. Res. Develop.* **32** (1988) 24

Kirceznov G. *J. Phys. Condens. Matter* **1** (1989) 305

Kumar A., Laux S.E., Stern F. *Appl Phys Lett* **54** (1989) 1270

Landauer R. *IBM. J. Res. Dev.* **1** (1957) 223

Landauer R. *Z. Phys. Condensed Matter* **B68** (1987) 217

Landauer R. in *Proceedings of the International Symposium on Nanostructure Physics and Fabrication,* edited by Reed M.A., Kirk W.P. (Academic Press, New York 1989)

Landauer R. *J. Phys.: Condens. Matter* **1** (1989b) 8099

Laughton M.J., Barker J.R., Nixon J.A., Davies J.H. *Phys Rev* **B44** (1991) 1150

Lee P.A., Fisher D.S. *Phys Rev Lett 47* (1981) 882

Mattheij R.M.M. *SIAM Review* **27** (1985) 1

Moshinsky M. *Am J Phys* **44** (1976) 1037

Nixon J.A., Davies J.H., Barker J.R. in *Proceedings of the International Symposium on Nanostructure Physics and Fabrication,* edited by Reed M.A., Kirk W.P. (Academic Press, New York 1989)

Nixon J.A., Davies J.H. *Phys Rev* **B41** (1990) 7929

Nixon J.A., Davies J.H. *Phys Rev* **B43** (1991) 12638

Nixon J.A., Davies J.H., Baranger H.U. *Phys Rev* **B43** (1991) 12638

Payne M.L. *J. Phys. Condens. Matter* **1** (1989) 4939

Potter D. *Computational Physics* (John Wiley & Sons, New York, 1973)

Press W.H., Flannery B.P., Teukolsky S.A., Vetterling W.T. *Numerical Recipes* (Cambridge University Press, Cambridge, 1987)

Roberts S.M., Shipman J.S. *Two Point Boundary Value Problems* (Elsevier, 1972)

Roukes M.L., Scherer A., Allen S.J., Craighead H.G., Ruthen R.M., Beebe E.D., Harbison J.P. *Phys Rev Lett.***59** (1987) 3011

Roukes M.L., Thornton T.J., Scherer A., Simmons J.A., Van der Gaag B.P., Beebe E.D., in *Science and Engineering of 1- and 0- Dimensional Semiconductors,* edited by Beaumont S.P., Sotomayor-Torres C.M. (Plenum 1989)

Sakaki H. *Jpn J. Appl. Phys.***19** (1980) L735

Schiff L.I. *Quantum Mechanics* (McGraw-Hill, 1968)

Sols F., Macucci M. *Phys Rev* **B41** (1990) 11887

Stone A.D., Szafer A. *IBM J. Res. Develop.* **32** (1988) 384

Szafer A., Stone A.D. *Phys Rev Lett* **62** (1989) 300

Thornton T.J., Roukes M.L., van der Gaag B.P. *16th International Conference on GaAs and Related Compounds, Sept 1989, Karuizawa, Japan.*

Thouless D.J. *Phys Rep* **13** (1974) 93

Timp G., Behringer R., Sampere S., Cunningham J.E., Howard R.E. in *Proceedings of the International Symposium on Nanostructure Physics and Fabrication,* edited by Reed M.A., Kirk W.P. (Academic Press, New York 1989)

Wharam D.A., Thornton T.J., Newbury R., Pepper M., Ahmed H., Frost J.E.F., Hasko D.G., Peacock D.C., Ritchie D.A., Jones G.A.C. *J. Phys. C* **21** (1988) L209

Williamson J.G. Private Communication (1990)

Wilson E.B., Decuis J.C., Cross P.C. *Molecular Vibrations* (Clarendon 1955)

van Wees B.J., van Houten H., Beenakker C.W.J., Williamson J.G., Kouwenhoven L.P., van der Marel D., Foxon C.T. *Phys Rev Lett* **60** (1988) 848

Yacoby A., Imry Y. *Phys Rev* **B41** (1990) 5341

Yosefin M., Kaveh M. *Phys Rev Lett* **64** (1990) 2819

GLASGOW
UNIVERSITY
LIBRARY